The Dissertation Committee for Sean Michael Wood certifies that this is the approved version of the following dissertation:

Studies of Potential Anode Materials for Lithium-Ion Batteries

Committee:

Charles Buddie Mullins, Supervisor

Adam Heller, Co-Supervisor

Arumugam Manthiram

Gyeong S. Hwang

Guihua Yu

Studies of Potential Anode Materials for Lithium-Ion Batteries

by

Sean Michael Wood, B.S. CHEM. & BIO. E., M.S.E.

Dissertation

Presented to the Faculty of the Graduate School of

The University of Texas at Austin

in Partial Fulfillment

of the Requirements

for the Degree of

Doctor of Philosophy

The University of Texas at Austin

August 2016

Dedication

To my family and friends for their never-ending support and encouragement,

To my all of my labmates for their advice and wisdom,

And to my dog, Elektra, for her constant comfort and companionship over the years.

Acknowledgements

I want to acknowledge and thank the many people who have helped and guided me throughout my long and arduous journey in graduate school. Primarily I would like to thank my family and friends for their unwavering support, especially my mother Sharon, my sister Shannon, my aunt Robin, and my stepfather David for encouraging me to keep going when times were rough. Even though I am halfway across the country, without them I would not have made it this far. Also, I would like to thank my stepmother Silke and my father Stuart halfway across the world for the comedic encouragement of their "Drei Jahres Plan".

I would also like to express my sincerest gratitude to my supervisor, Professor Buddie Mullins, and my co-supervisor, Professor Adam Heller. Dr. Mullins has taught me many of the soft skills necessary to succeed and thrive outside of the lab, and I value the many one-on-one discussions I have had with him over the years, where I was able to learn many important lessons from his storytelling. Dr. Heller has tried to impart his vast wisdom on me and finally helped me to understand the fundamental difference between science and engineering. He also genuinely cared about my success and wanted for me to do with my life whatever makes me happiest, whether that was in academia or elsewhere. For that, I am eternally grateful.

I would also like to express my appreciation to Dr. Arumugam Manthiram, Dr. Gyeong Hwang, and Dr. Guihua Yu for their valuable input and time commitment in serving on my dissertation committee. Two other professors have also helped me to grow outside of the Chemical Engineering field. I appreciate Dr. Varun Rai's invitations to present my work to my peers and a wider audience through the UT Energy Symposium.

And I valued greatly my time working with Dr. Tom Edgar in the IGERT program and the unique experiences that provided, including the chance to study abroad in Munich, Germany.

My friends outside of the lab have been one of my greatest sources of joy during my time here in Austin, and I am forever grateful for them. The ridiculous antics of Adrien Guillaussier and Kevin Vasquez always brought a smile to my face. Discussions about politics and pop culture with Stephen Hoang served as a needed escape from the world of engineering. Venting my frustrations with Matt Walters, who went through the trials and tribulations of graduate school with me, helped keep me level headed and focused towards the light at the end of the tunnel.

I would also like to thank the friends in my lab who have provided me endless sources of fascinating discussion and comedic relief, helping to keep me sane: Emily Powell, Edward Evans, Melissa Meyerson, Bryan Wygant, Adrian Brush, and Rodrigo Rodriguez. They have all been truly wonderful people to work with.

I would like to thank my undergraduate assistant, Codey Pham, who helped me complete so many of the experiments that led to this dissertation. I would also like to thank the other collaborators who assisted in my various published works: Dr. Kyle Klavetter, Dr. Andrei Dolocan, Dr. Hugo Celio, Sindhu Nathan, and Pedro de Souza. I would also like to acknowledge Solvay Fluor for their donation of fluoroethylene carbonate and Celgard for their donation of separator membranes to our laboratory.

Finally, I would like to acknowledge the financial support of the Welch Foundation, the National Science Foundation's Integrative Graduate Education Research Traineeship program, and the Department of Defense's National Defense Science and Engineering Graduate Fellowship program.

Studies of Potential Anode Materials for Lithium-Ion Batteries

Sean Michael Wood, Ph.D.

The University of Texas at Austin, 2016

Supervisor: Charles Buddie Mullins

Co-Supervisor: Adam Heller

Lithium-ion batteries (LIBs) are currently used in nearly all consumer electronics, including cellular phones, laptop computers, and wearable devices such as smart watches. In the future, these batteries will also be used in electric vehicles and to store excess energy on a grid scale from intermittent sources such as wind and solar. On the anode side of LIBs, graphite has been the state-of-the-art material for the last 25 years and is reaching its technological limits, so research into new anode materials is needed in order to meet the increasing consumer demands for smaller, longer lasting batteries.

The use of lead would be an incremental improvement over graphite since it has a higher capacity and is also cheap and abundant. A series of lead chalcogenides (PbO, PbS, PbSe, and PbTe) was synthesized, and their electrochemical properties were tested to determine their usefulness as potential LIB anode materials. PbO and PbS were found to perform poorly. PbSe performed better, although exhibited side reactions that rendered it unusable in actual LIBs. PbTe performed extremely well over the given testing window, able to be charged and discharged in only 30 minutes without suffering capacity fade. However, this material would be too expensive to use on a large scale due to tellurium's rarity. Additionally, the 30 year old lithium-lead reaction mechanism in the literature was updated using a series of *ex situ* X-ray diffraction experiments.

A step change improvement over graphite could come from using lithium metal, which would increase the anode capacity by a factor of 10. However, lithium metal suffers from uncontrollable dendritic growths which pose extreme safety hazards. An electrolyte additive was developed using potassium ions to overcome this dendrite issue. Dendritic growth was completely halted when this additive was used, and the cells cycled stably over the entire 18 day test period. The corrosion layer that forms on the surface of the lithium metal was characterized (via electrochemical impedance spectroscopy, X-ray photoelectron spectroscopy, and time of flight – secondary ion mass spectrometry) and found to be altered by the presence of potassium, leading to the improved performance.

Table of Contents

List of Tables

List of Figures

SECTION 1:
INTRODUCTION TO LITHIUM-ION BATTERIES

Chapter 1:
Components of a Lithium-ion Battery

Energy storage is a critical component of many of the technologies that exist today, from portable consumer electronics to power tools, implantable medical devices to electric vehicles.[1,2] There are a number of different options for energy storage including batteries, fuel cells, capacitors and supercapacitors, compressed air, flywheels, and pumped hydro, each with power and energy densities (shown in the Ragone plot of Figure 1.1, which was recreated with data from the IEC[3]) suited for different applications. Of the different types of energy storage, electrochemical energy storage technologies are most well-suited for portable applications.

Batteries are by far the most popular and common of these technologies, existing in both non-rechargeable (primary) and rechargeable (secondary) forms.[4] Examples of primary batteries include disposable alkaline batteries (commonly seen in AA or AAA format), lithium batteries, and silver oxide and zinc air batteries (both of which are used in smaller applications such as watches and hearing aids). Secondary batteries gain more attention due to their reusability and include chemistries such as lead-acid, nickel cadmium, nickel metal hydride, and lithium-ion batteries. Lithium-ion batteries in particular have become the most prominent of these technologies in the 25 years since Sony first commercialized them in part due to their high energy density (due to its most negative electrochemical redox potential of -3.04 V vs. the standard hydrogen electrode) and low weight (with a density of only 0.53 g cm^{-3}).[4,5]

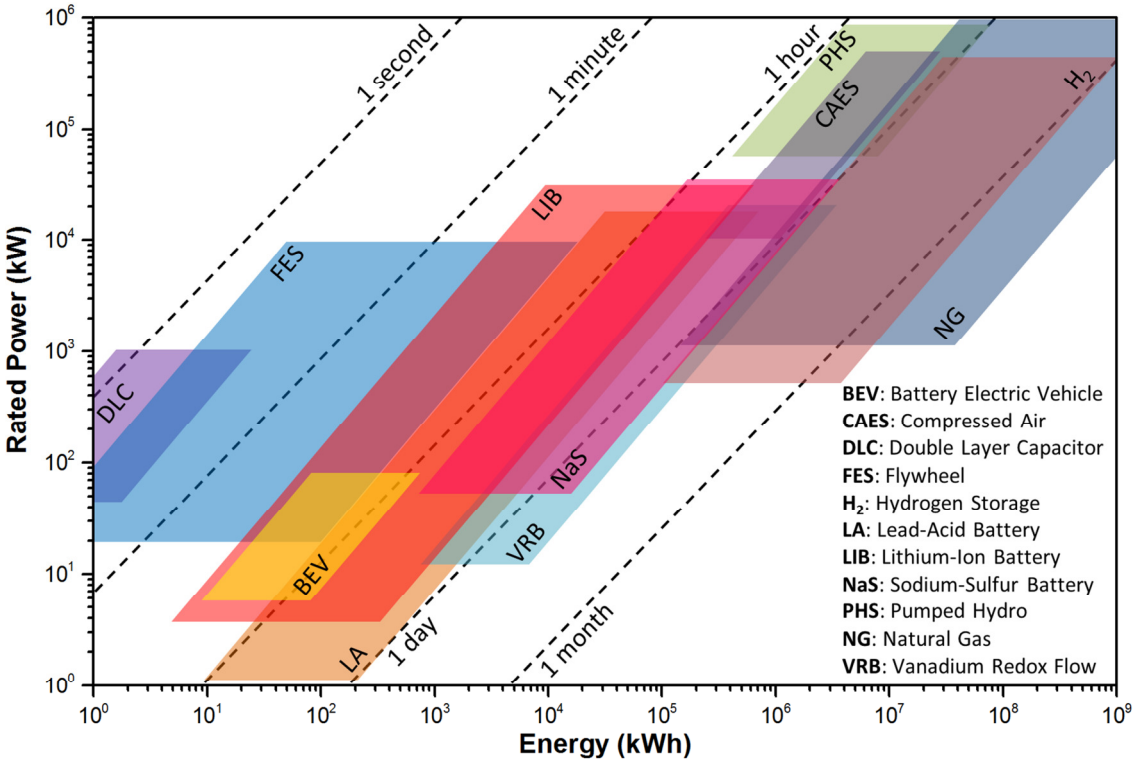

Figure 1.1. Ragone plot comparing the energy and rated power of various energy storage technologies.

Over the past two and a half decades, lithium-ion batteries have been used in everything from laptops and cellphones to portable music players and wearable electronics, demanding ever decreasing size and increased energy density. In the future, lithium-ion battery growth will continue at an exponential rate as they are more widely used in things like electric vehicles and at the grid scale to store excess energy from intermittent power sources such as wind and solar.[2,6,7] Figure 1.2 shows past trends in worldwide lithium usage as well as projected future usage, showing that use of these batteries is expected to continue growing exponentially.[8]

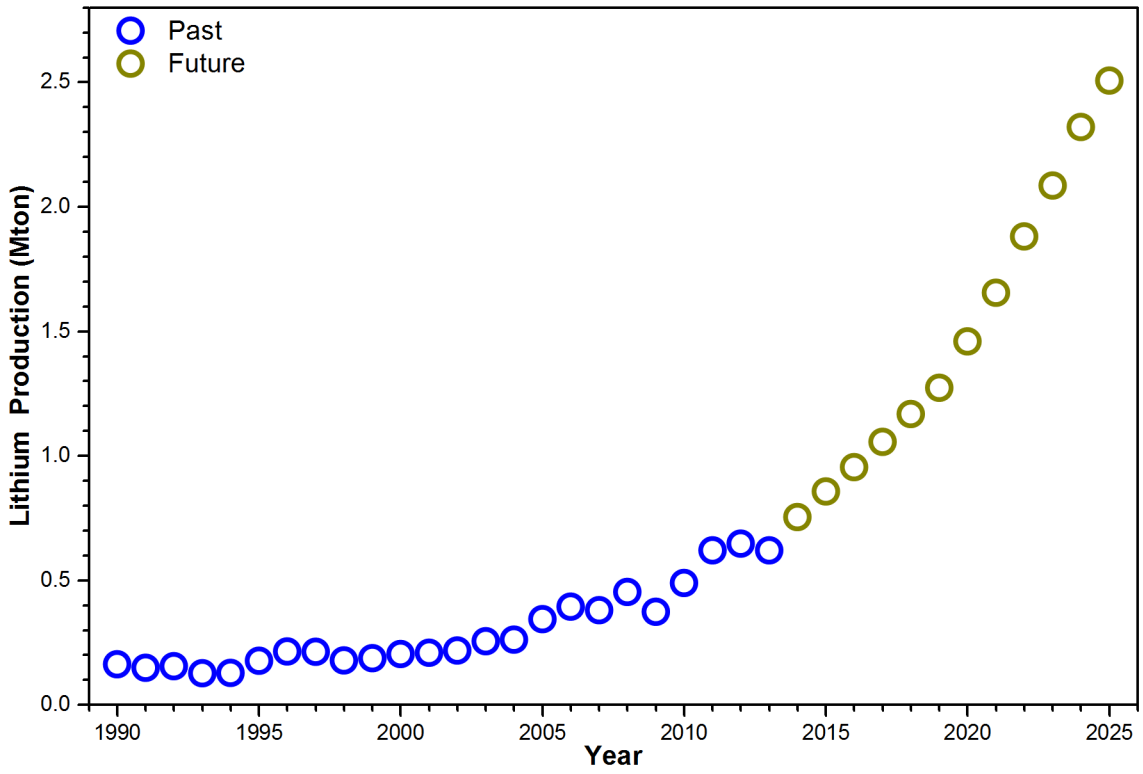

Figure 1.2. Worldwide lithium production since 1990 and expected growth in lithium production until 2025.

A schematic of a typical lithium-ion battery is shown in Figure 1.3. It is comprised of an anode, a cathode, a separator, and an electrolyte, each of which will be further discussed in the following sections.

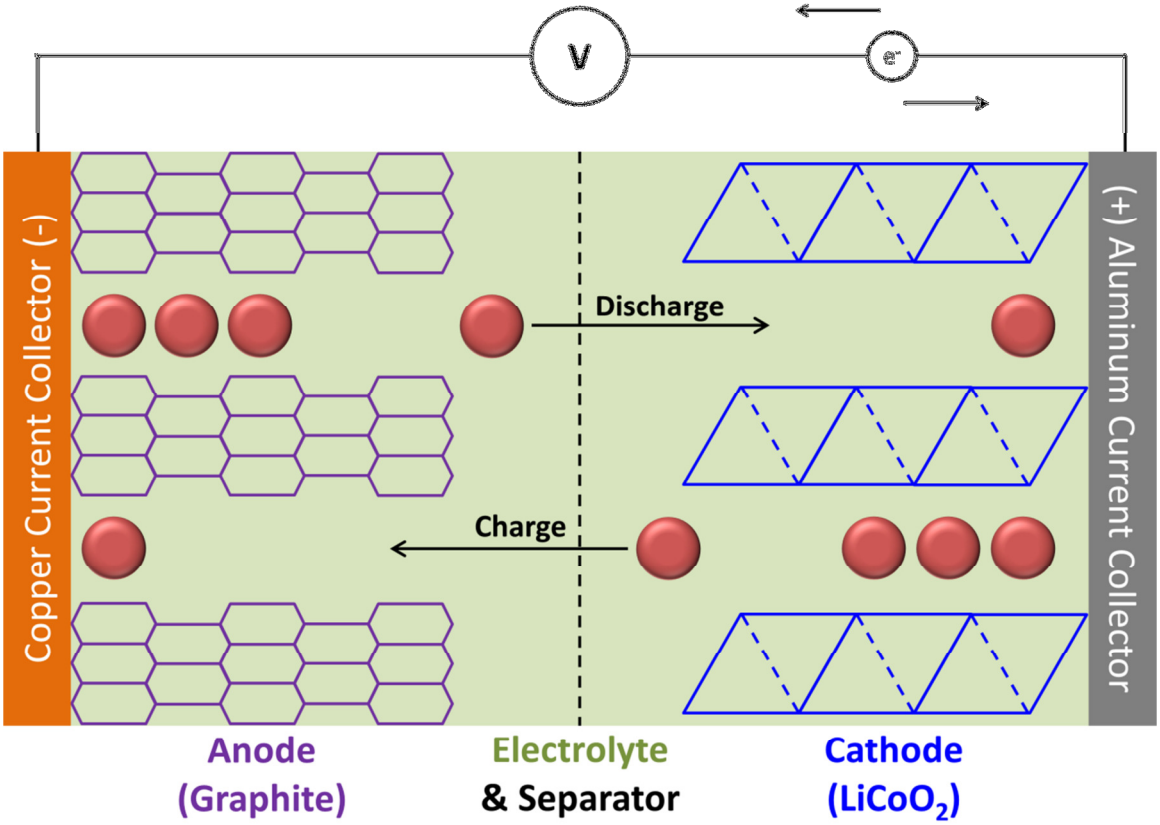

Figure 1.3. Schematic of a lithium-ion battery. Lithium ions are represented as red spheres.

ANODE & CATHODE

The anode and the cathode are the two electrochemically active components of a lithium-ion battery and are the two materials that store all of the charge.[6,7,9] When a battery is fully discharged, all of the lithium is stored in the cathode, which is typically a metal oxide such as $LiCoO_2$ or $LiFePO_4$. To charge the battery, an external voltage is applied to force the lithium ions to shuttle from the cathode to the anode, where graphite is the most commonly used material. The lithium ions are stored between the graphene layers of the graphite when the battery is fully charged. To discharge the battery, electrons are allowed to flow through an external circuit to power a device, and the

lithium ions shuttle from the anode back to the cathode.[2] An example of the reaction that occurs during charging and discharging on the cathode side is shown in Equation 1.1. An example of the reaction that occurs during charging and discharging of the anode is shown in Equation 1.2. The overall cell reaction is shown in Equation 1.3.[10]

Equation 1.1: Cathode: $LiCoO_2 \rightleftharpoons Li_{1-x}CoO_2 + x\ Li^+ + x\ e^-$

Equation 1.2: Anode: $C + x\ Li^+ + x\ e^- \rightleftharpoons Li_xC$

Equation 1.3: Overall: $LiCoO_2 + C \rightleftharpoons Li_{1-x}CoO_2 + Li_xC$

Commonly-used anode and cathode materials as well as next-generation materials are shown in Figure 1.4. In this plot, the cathode materials (purple) are at higher potentials and anode materials (green) are at lower potentials.[4] The overall battery voltage is calculated by subtracting the anode potential from the cathode potential: $V_{battery} = V_{cathode} - V_{anode}$.

For example, the most common battery in use today ($LiCoO_2$ | Graphite) has a potential of 3.9 V vs. Li/Li^+ – 0.2 V vs Li/Li^+ = 3.7 V. Although next generation cathode materials such as sulfur and air have a lower potential, their overall energy density would still be much higher due to their greatly increased capacity versus the transition metal oxides since the overall energy density of a battery is the product of the capacity and voltage.

Graphite has begun to reach its technical limits in terms of capacity, so the Group IVA elements (Si, Ge, Sn, and Pb) have been widely studied as next generation anode materials due to their ability to store high numbers of lithium ions per atom.[1,2] Additionally, graphite suffers from safety issues at higher charge rates (greater than 1C, where nC corresponds to a charging time of 1/n hours) due to the formation of lithium dendrites, which pose a shorting (and thus fire/explosion) hazard.[7] The Group IVA elements benefit from improved safety in this respect; their lithiation potentials are higher

than that of graphite and so the risk of dendrite formation is mitigated. Lithium metal is the ultimate chemistry for lithium-ion secondary batteries because of its highest capacity and lowest electrochemical potential (which translates to highest overall battery voltage) of any material. However, lithium metal is plagued by the same dendritic growth issue, which has precluded its safe use for at least 40 years.[11–13]

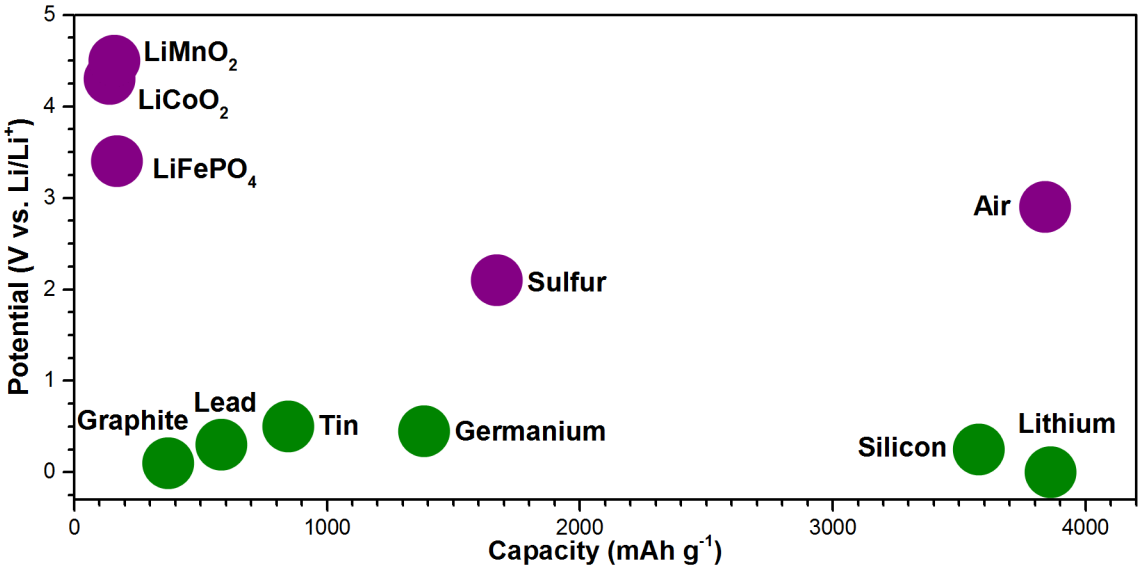

Figure 1.4. Capacity and voltage comparisons of various cathode and anode materials.

In the most commonly used particle-based electrodes, the active electrode materials are first mixed with a conductive carbon (to ensure that the particles maintain an electrically conductivity network), a polymer binder (which acts as the glue to hold everything together), and a solvent (to dissolve the binder) to form a slurry which is then coated onto the current collector foil. Aluminum foil is the preferred material for current collectors since it is both inexpensive and lightweight, and it is currently used on the cathode side. However, lithium alloys with aluminum at the lower potentials (below 1.0

V vs. Li/Li^+) where most anodes function. As such, the use of heavier, more expensive copper foil is necessitated for the current collector on the anode side.[9]

ELECTROLYTE

The electrolyte in the battery acts as the medium by which charge is transferred, allowing ions to pass back and forth between the anode and cathode while preventing electrons from doing the same. The electronically insulating nature of the electrolyte forces the charge to pass through an external circuit, providing the mechanism for charging and discharging the battery.[14,15]

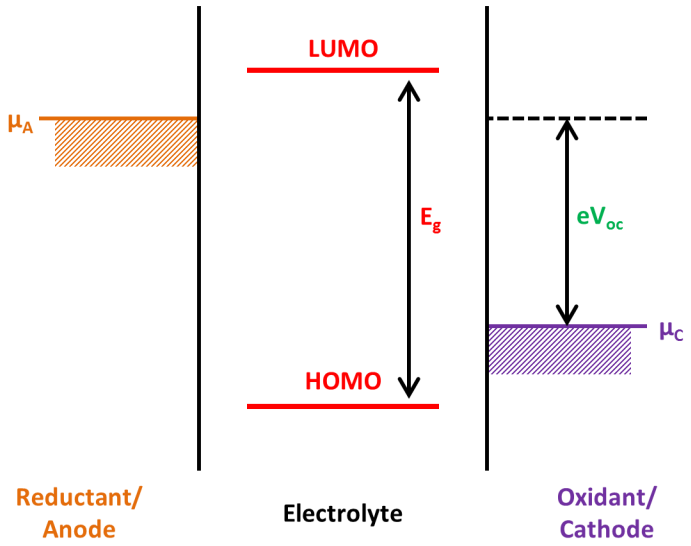

Figure 1.5. Schematic diagram of the relative energies of the electrodes and electrolyte at open circuit potential.

The relative energies and chemical potentials of the electrodes and electrolyte are shown schematically in Figure 1.5.[6,16] μ_A and μ_C represent the chemical potentials of the anode and cathode, respectively, and their difference represents the open circuit potential of the battery, given by $V_{oc} = (\mu_A - \mu_C)/e$. LUMO is the lowest unoccupied molecular

orbital of the electrolyte, whereas HOMO is the highest occupied molecular orbit; their difference, E_g, represents the energy gap between them which is the electrolyte's stability window. If μ_A is higher than the LUMO, electrons will transfer from the anode to the electrolyte, reducing the electrolyte. On the other hand, if the μ_C is lower than the HOMO, electrons will transfer from the electrolyte to the cathode, oxidizing the electrolyte. The electrolyte will only be stable and unreacted if the eV_{oc} lies entirely within the electrolyte stability window E_g.

In most commercial lithium-ion batteries, which use an electrolyte comprised of 1 M of $LiPF_6$ salt dissolved in a 1:1 (v/v) mixture of ethylene carbonate (EC) and dimethyl carbonate (DMC), the open circuit potential does not lie nicely within the electrolyte stability window. While the potential of the typical cathodes (3.2 – 4.2 V vs. Li/Li^+) lies below the upper stability limit of the electrolyte (~4.5 V vs. Li/Li^+ for EC/DMC) and prevents electrolyte oxidation, the anodes typically operate at much lower potentials (0.0 – 0.5 V vs. Li/Li^+) than the lower stability limit of the electrolyte (~0.8 V vs. Li/Li^+ for EC/DMC).[15] Thus, the electrolyte is typically reduced on the surface of the anode during charging, forming a film of reaction products referred to as the "solid electrolyte interphase" or SEI.[14–17] At some point, this layer becomes thick enough that electrons can no longer tunnel through it in order to further react, and the reaction terminates, behavior which is referred to as "self-passivation". This layer plays a number of important roles in the stable cycling of lithium-ion batteries, including the prevention of solvent co-intercalation into graphite and the prevention of dendrites on lithium metal, and its importance cannot be understated.

SEPARATOR

The separator serves the vitally important function of keeping the two electrodes within a battery electrically disconnected from each other. In the event that an electrical connection is made, a short circuit occurs, neutralizing the two sides and preventing the battery from storing any charge. Additionally, the rapid, unimpeded flow of electrons that travels across a short circuit can cause a thermal runaway within the battery. In a battery with a flammable electrolyte such as lithium-ion batteries, this rapid heating can lead to fires or explosions, making the separators an important failsafe and safety consideration.[18]

The most common separators are porous polypropylene or polyethylene membranes. They are made as thin as possible to allow for maximum utilization of the battery's limited volume and are typically on the order of 25 μm thick. The pores are large enough to allow facile transport of lithium ions between the two sides without allowing the two sides to potentially make electrical contact. A typical average pore diameter is in the range of 20 – 100 nm.

REFERENCES

(1) Bruce, P. G.; Scrosati, B.; Tarascon, J.-M. Nanomaterials for Rechargeable Lithium Batteries. *Angew. Chemie* **2008**, *47*, 2930–2946.

(2) Thackeray, M. M.; Wolverton, C.; Isaacs, E. D. Electrical Energy Storage for Transportation—approaching the Limits Of, and Going Beyond, Lithium-Ion Batteries. *Energy Environ. Sci.* **2012**, *5*, 7854–7863.

(3) IEC. *Electrical Energy Storage White Paper*; 2012.

(4) Tarascon, J. M.; Armand, M. Issues and Challenges Facing Rechargeable Lithium Batteries. *Nature* **2001**, *414*, 359–367.

(5) Han, J.; Huang, Y.; Goodenough, J. New Anode Framework for Rechargeable Lithium Batteries. *Chem. Mater.* **2011**, *23*, 2027–2029.

(6) Goodenough, J. B.; Park, K.-S. The Li-Ion Rechargeable Battery: A Perspective. *J. Am. Chem. Soc.* **2013**, *135* (4), 1167–1176.

(7) Wen, J.; Yu, Y.; Chen, C. A Review on Lithium-Ion Batteries Safety Issues: Existing Problems and Possible Solutions. *Mater. Express* **2012**, *2* (3), 197–212.

(8) Survey, U. S. G. *Mineral Commodity Summaries 2016: Lead*; 2016.

(9) Wakihara, M. Recent Developments in Lithium Ion Batteries. *Mater. Sci. Eng. R Reports* **2001**, *33* (4), 109–134.

(10) Etacheri, V.; Marom, R.; Elazari, R.; Salitra, G.; Aurbach, D. Challenges in the Development of Advanced Li-Ion Batteries: A Review. *Energy Environ. Sci.* **2011**, *4*, 3243–3262.

(11) Xu, W.; Wang, J.; Ding, F.; Chen, X.; Nasybulin, E.; Zhang, Y.; Zhang, J.-G. Lithium Metal Anodes for Rechargeable Batteries. *Energy Environ. Sci.* **2014**, *7*, 513.

(12) Li, Z.; Huang, J.; Yann Liaw, B.; Metzler, V.; Zhang, J. A Review of Lithium

Deposition in Lithium-Ion and Lithium Metal Secondary Batteries. *J. Power Sources* **2014**, *254*, 168–182.

(13) Kim, H.; Jeong, G.; Kim, Y.-U.; Kim, J.-H.; Park, C.-M.; Sohn, H.-J. Metallic Anodes for next Generation Secondary Batteries. *Chem. Soc. Rev.* **2013**, *42* (23), 9011–9034.

(14) Aravindan, V.; Gnanaraj, J.; Madhavi, S.; Liu, H.-K. Lithium-Ion Conducting Electrolyte Salts for Lithium Batteries. *Chem. A Eur. J.* **2011**, *17*, 14326–14346.

(15) Xu, K. Nonaqueous Liquid Electrolytes for Lithium-Based Rechargeable Batteries. *Chem. Rev.* **2004**, *104* (10), 4303–4417.

(16) Goodenough, J. B.; Kim, Y. Challenges for Rechargeable Li Batteries. *Chem. Mater.* **2010**, *22* (3), 587–603.

(17) Verma, P.; Maire, P.; Novák, P. A Review of the Features and Analyses of the Solid Electrolyte Interphase in Li-Ion Batteries. *Electrochim. Acta* **2010**, *55* (22), 6332–6341.

(18) Lee, H.; Yanilmaz, M.; Toprakci, O.; Fu, K.; Zhang, X. A Review of Recent Developments in Membrane Separators for Rechargeable Lithium-Ion Batteries. *Energy Environ. Sci.* **2014**, *7* (12), 3857–3886.

Chapter 2:
Dissertation Overview

This dissertation consists of ten chapters. The first chapter provides a general introduction to lithium-ion batteries and the components that comprise them. The current chapter provides an overview of subsequent chapters. Chapter 3 provides some background and motivation on the use of lead as a lithium-ion battery anode material, as well as a brief overview of the literature involving lead. Chapters 4 through 7 represent independent studies on lead-base anode materials for lithium-ion batteries, each of which has been published in a peer reviewed journal. Chapter 8 summarizes the works of the previous chapters on lead-based materials while also providing some concluding remarks. Chapter 9 is an independent study on the use of lithium metal as an anode in lithium-ion batteries, work which is expected to be published in a peer-reviewed journal after the publican of this dissertation. Finally, Chapter 10 offers some commentary about future directions for research. Each of the peer reviewed works is summarized below.

In Chapter 4, the intermediates and final phase in the dynamic electrochemical lithiation of lead at ambient temperature were determined by *ex situ* XRD. The phases and their corresponding potentials matched well with coulometric data. The detected phases were LiPb, Li_8Pb_3, Li_3Pb, and Li_7Pb_2.

In Chapter 5, the reversible charging of a lead chalcogenide, PbTe, was studied for use as the anode material in a Li-ion cell and compared to PbO. A similar series of Li-Pb alloys were formed but with Li_2Te present instead of Li_2O. In the presence of Li_2Te, rapid Li-Pb alloying and dealloying were observed in the potential range of 0.01 – 0.7 V. In the potential range of 0.8 – 2.5 V, Li_2Te formed and decomposed reversibly. Electrodes were cycled stably for 100 cycles at a C/5 rate in both potential domains. The electrodes were also cycled stably at rates up to 10C. The presence of Li_2Te reduced the

overpotential required at higher charge and discharge rates by acting as a superionic conductor to improve lithium ion diffusion. These results recommend this material for potential use in low-power applications such as cell phones.

In Chapter 6, the lithiation and delithiation of PbS was studied. Below 1.0 V vs. Li/Li^+, lithiation produced a series of Li-Pb alloys and Li_2S. The Li-Pb alloys were reversibly lithiated and delithiated, but at a 1 C rate their capacity faded through 100 cycles. Above 1.5 V vs. Li/Li^+, Li_2S was electrooxidized to Li^+ and soluble polysulfides, and the sulfide was irreversibly depleted.

In Chapter 7, the reversibility and rate of lithiation of PbSe was explored. As expected, PbSe was reversibly lithiated to Li_2Se and Li-Pb alloys, but the electrode was less stable and could not be cycled as rapidly as the PbTe electrode of Chapter 5. When the electrode was cycled at a slow rate, an electroactive polymer gel film (PGF) derived of the 1M $LiPF_6$ in 1:1 fluoroethylene carbonate/diethyl carbonate (w/w) electrolyte built up in the initial 25 cycles. Electroreduction and electrooxidation of this film added to the capacity by as much as 300 mAh g^{-1} above its theoretical value. Visual and electrochemical evidence of the PGF was presented.

In Chapter 9, addition of 10 mM KPF_6 to the 1 M $LiPF_6$ in ethylene carbonate/dimethyl carbonate electrolyte of symmetrical Li | Li cells was found to eliminate the growth of dendrites at 0.5 mA cm^{-2} current density and massively reduce, but not eliminate, the growth of dendrites at 2.5 mA cm^{-2}. The added KPF_6 increased the fraction of Li_2CO_3 in the solid electrolyte interface (SEI) 8.6-fold to 88%, making it thinner and more Li^+ permeable. It overcame the growth of dendrites resulting of inadequate nucleation density but not dendrite growth into the depletion layer, which scales with the layer's thickness, i.e. the current density.

SECTION 2:
LEAD-BASED LITHIUM-ION BATTERY ANODE MATERIALS

Chapter 3:
Introduction and Motivation for Using Lead-based Materials

In the United States in 2014, 90% of lead production was devoted to producing lead-acid batteries, which were primarily used for conventional automobiles and trucks.[1] As the worldwide vehicle fleet is increasingly electrified and all-electric vehicles such as the Nissan Leaf, Chevrolet Bolt, and Tesla Model S become more widely adopted,[2] demand for lead-acid batteries will decline and an excess of lead production will develop. The Pb used in conventional automobile lead-acid batteries will need to be repurposed.

Lead exhibits several improved characteristics over the current state-of-the-art material, graphite, and its use in lithium-ion batteries is predicated on previous research into Group IVA materials such as Si, Ge, and Sn. These materials alloy with lithium at potentials appreciably above that of the Li/Li^+ redox couple, which alleviates the risk of electroplating and dendrite formation that leads to shorting and fires and makes pure Li metal unsafe to use. Additionally, lead forms a series of lithium-lead alloys with an ultimate specific capacity of 452 mAh g^{-1} compared to only 360 mAh g^{-1} for graphite. As a metal, lead also has a much higher electronic conductivity than graphite.

However, because of its heavy weight, lead is only suitable for certain applications of lithium-ion batteries. For example, in large grid-scale storage of intermittent energy from sources such as wind and solar, cost is the key property. In a stationary setup, the weight of the battery does not matter. Lead-based batteries would be well-suited for this application. Additionally, the higher capacity and density of lead could be used to make batteries for consumer electronics which have a smaller volume while holding the same amount of charge. This characteristic would be a boon for cell-phone manufacturers who are constantly looking for new ways to shrink the batteries to make their phones thinner and thinner. Lead-based lithium-ion batteries would not be

suitable, however, in an application such as electric cars, where the high weight of lead would reduce the overall range of the vehicle.

Lead has been relatively understudied as a lithium-ion battery anode material compared to the other Group IVA elements such as Si, Ge, and Sn; at the time of this writing, there were fewer than 30 publications involving lead in the literature. Below is a brief summary of this literature.

PbO has been the most commonly studied of the lead compounds. Torabi et al. synthesized PbO nanoparticles which faded rapidly to 100 mAh g^{-1} over 40 cycles.[3] Martos et al. were able to attain capacities of nearly 500 mA h g^{-1} for 40 cycles with their spray-pyrolyzed PbO films.[4] A similar *in situ* spray solution technique was used by Konstantinov et al. to create nanostructured PbO which suffered rapid capacity loss and poor performance, decreasing to only 50 mAh g^{-1} after 50 cycles.[5] Ng et al. attempted another version of a spray-pyrolized PbO nanocomposite; this material also suffered rapid capacity loss to 100 mAh g^{-1} after 50 cycles.[6] Pan et al. synthesized a PbO@C core-shell nanocomposite which decreased in capacity to 200 mAh g^{-1} after 50 cycles.[7] Wang et al. synthesized another version of the PbO@C nanocomposite, achieving stable cycling at 175 mAh g^{-1} for the entire 100 cycle test.[8] Martos et al. also compared the cycling performance of different mixtures of PbO_2, Pb_3O_4, PbO, and Pb. All of their composites cycled poorly, decreasing to below 100 mAh g^{-1} after only 15 cycles.[9] Li et al. formed a composite of PbO with Cu and found stable performance, maintaining a steady capacity of over 300 mAh g^{-1} for 100 cycles.[10]

Other Pb-based chalcogenides were also studied. Sanusi et al. examined PbS and elucidated its lithiation mechanism but did not attempt to cycle it.[11] Xie et al. synthesized a PbSe/reduced-graphene oxide nanosheet composite, which maintained 300 – 400 mAh g^{-1} of capacity after 100 cycles.[12] Tu et al. were able to achieve capacities of

approximately 500 mA h g^{-1} that faded to 300 mA h g^{-1} after 100 cycles with their graphene-sandwiched PbTe nanoparticles.[13]

Lead has been used in its metallic or metal-alloy form as well. Using Pb-sandwiched nanoparticles, Chen et al. were able to achieve capacities of over 200 mA h g^{-1} for 200 cycles.[14] With a Sn–Pb composite oxide, Yuan et al. could reach capacities of 550 mA h g^{-1} for 20 cycles.[15] By lithiating a lead-aluminum-tin solder, Trifonova et al. found improved performance over pure Pb or Sn.[16] With a hydrothermally synthesized $PbGeO_3$/graphene composite, Wang et al. achieved capacities of nearly 600 mAh g^{-1} over 50 cycles.[17]

Lead has also been combined with various other anions, such as halides, nitrates, and phosphates, and tested as anode materials. The $Pb_3(PO_4)_2$ anodes of Liu et al. decayed to 200 mAh g^{-1} after only 5 cycles, representing one of the first attempts to cycle lead as an anode material.[18] Wang et al. reached a capacity of 250 mAh g^{-1} after 50 cycles with $Pb(NO_3)_2$/C.[19] A lead-tin composite fluoride was tested by Tovar et al., which was able to achieve high first-cycle capacity but faded rapidly after that.[20] Shu et al. synthesized $PbSbO_2Cl$, which faded to 300 mAh g^{-1} after only 20 cycles.[21] Their hydrothermally fabricated PbOHCl suffered similar performance.[22] Li et al. also synthesized a series of $PbSbO_2Cl$ materials, which all faded to only 300 – 400 mAh g^{-1} after 30 cycles.[23,24]

In the next chapter, the widely-cited reaction scheme available in the literature for the lithiation of lead was found to be incorrect. An *in situ* X-ray diffraction (XRD) study was performed in order to propose a new reaction scheme. In the subsequent three chapters, a systematic study of a series of lead chalcogenides was undertaken to evaluate their performance relative to each other using similar synthesis methods and testing conditions. All of the synthesis methods for the various lead chalcogenides (PbO, PbS,

PbSe, and PbTe) were chosen to maximize simplicity and minimize cost in the event that the materials performed well, allowing for relatively facile scale-up. As such, all of the synthesis methods involve heating and mixing two solutions, one of which is usually comprised of water and a lead salt, and the other of which is usually comprised of water, sodium hydroxide, and the chalcogenide itself (S, Se, or Te). The performance of these materials varied widely but typically followed a trend of improved performance with higher cost and higher weight of the chalcogenide (i.e. PbO performed worst; PbTe performed best).

REFERENCES

(1) Survey, U. S. G. *Mineral Commodity Summaries 2016: Lead*; 2016.

(2) Warner, J. *Lithium-Ion Batteries: Advances and Applications, Chapter 7. Lithium-Ion Battery Packs for EVs*; 2014; Vol. 1.

(3) Torabi, M. Electrochemical Evaluation of PbO Nanoparticles as Anode for Lithium Ion Batteries. *Int. J. Eng.* **2011**, *24* (4), 351–356.

(4) Martos, M.; Morales, J.; Sanchez, L.; Ayouchi, R. Electrochemical Properties of Lead Oxide Films Obtained by Spray Pyrolysis as Negative Electrodes for Lithium Secondary Batteries. *Electrochim. Acta* **2001**, *46*, 2939–2948.

(5) Konstantinov, K.; Ng, S. H.; Wang, J. Z.; Wang, G. X.; Wexler, D.; Liu, H. K. Nanostructured PbO Materials Obtained *in situ* by Spray Solution Technique for Li-Ion Batteries. *J. Power Sources* **2006**, *159* (1), 241–244.

(6) Ng, S. H.; Wang, J.; Konstantinov, K.; Wexler, D.; Chen, J.; Liu, H. K. Spray Pyrolyzed PbO-Carbon Nanocomposites as Anode for Lithium-Ion Batteries. *J. Electrochem. Soc.* **2006**, *153* (4), A787–A793.

(7) Pan, Q.; Wang, Z.; Liu, J.; Yin, G.; Gu, M. PbO@C Core–shell Nanocomposites as an Anode Material of Lithium-Ion Batteries. *Electrochem. commun.* **2009**, *11* (4), 917–920.

(8) Wang, H.; Yu, J.; Zhao, Y.; Guo, Q. A Facile Route for PbO@C Nanocomposites: An Electrode Candidate for Lead-Acid Batteries with Enhanced Capacitance. *J. Power Sources* **2013**, *224*, 125–131.

(9) Martos, M.; Morales, J.; Sanchez, L. Lead-Based Systems as Suitable Anode Materials for Li-Ion Batteries. *Electrochim. Acta* **2003**, *48*, 615–621.

(10) Li, C.-H.; Sengodu, P.; Wang, D.-Y.; Kuo, T.-R.; Chen, C.-C. Highly Stable Cycling of a Lead Oxide/copper Nanocomposite as an Anode Material in Lithium

Ion Batteries. *RSC Adv.* **2015**, *5* (62), 50245–50252.

(11) Sanusi, A.; Yahya, M. Z. A.; Navaratnam, S.; Basirun, W. J.; Alias, Y.; Mohamed, N. S.; Arof, A. K. Sulphide Based Anode Material for Lithium Rechargeable Battery. *Ionics (Kiel).* **2003**, *9* (3-4), 253–257.

(12) Xie, J.; Tu, F.; Su, Q.; Du, G.; Zhang, S.; Zhu, T.; Cao, G.; Zhao, X. *In situ* TEM Characterization of Single PbSe/reduced-Graphene-Oxide Nanosheet and the Correlation with Its Electrochemical Lithium Storage Performance. *Nano Energy* **2014**, *5*, 122–131.

(13) Tu, F.; Huo, Y.; Xie, J.; Cao, G.; Zhu, T.; Zhao, X.; Zhang, S. Reduced Graphene Oxide Induced Confined Growth of PbTe Crystals and Enhanced Electrochemical Li-Storage Properties. *RSC Adv.* **2013**, *3* (45), 23612–23619.

(14) Chen, Z.; Cao, Y.; Qian, J.; Ai, X.; Yang, H. Pb-Sandwiched Nanoparticles as Anode Material for Lithium-Ion Batteries. *J. Solid State Electrochem.* **2011**, *16* (1), 291–295.

(15) Yuan, Z.; Peng, Z.; Chen, Y.; Liu, H. Synthesis and Electrochemical Performance of Nanosized Tin Lead Composite Oxides as Lithium Storage Materials. *Mater. Chem. Phys.* **2010**, *120* (2-3), 331–335.

(16) Trifonova, A.; Momchilov, A. Electrochemical Lithium Intercalation in Lead–tin–aluminium Solder. *Solid State Ionics* **2001**, *143*, 319–328.

(17) Wang, J.; Feng, C.-Q.; Sun, Z.-Q.; Chou, S.-L.; Liu, H.-K.; Wang, J.-Z. In-Situ One-Step Hydrothermal Synthesis of a Lead Germanate-Graphene Composite as a Novel Anode Material for Lithium-Ion Batteries. *Sci. Rep.* **2014**, *4* (7030), 1–7.

(18) Liu, Z.; Yang, J. Electrochemical Performance of Pb3(PO4)2 Anodes in Rechargeable Lithium Batteries. *J. Power Sources* **2001**, *97-98*, 247–250.

(19) Wang, D.; Wu, K.; Shao, L.; Shui, M.; Ma, R.; Lin, X.; Long, N.; Ren, Y.; Shu, J.

Facile Fabrication of Pb(NO3)2/C as Advanced Anode Material and Its Lithium Storage Mechanism. *Electrochim. Acta* **2014**, *120* (3), 110–121.

(20) Tovar, L. G.; Connor, P. Investigation of Lead Tin Fluorides as Possible Negative Electrodes for Li-Ion Batteries. *J. Power Sources* **2001**, *98*, 473–476.

(21) Shu, J.; Ma, R.; Shao, L.; Shui, M.; Hou, L.; Wu, K.; Chen, Y.; Wang, D.; Liang, Y.; Ren, Y. Facile Preparation of Nano-Micro Structure PbSbO2Cl as a Novel Anode Material for Lithium-Ion Batteries. *RSC Adv.* **2013**, *3* (2), 372–376.

(22) Shu, J.; Ma, R.; Shao, L.; Shui, M.; Wang, D.; Wu, K.; Long, N.; Ren, Y. Hydrothermal Fabrication of Lead Hydroxide Chloride as a Novel Anode Material for Lithium-Ion Batteries. *Electrochim. Acta* **2013**, *102*, 381–387.

(23) Li, P.; Lin, X.; Shao, L.; Shui, M.; Wang, D.; Long, N.; Shu, J. PbSbO2Cl@C Nanocomposite as Lithium Storage Material for Secondary Lithium-Ion Batteries. *J. Electroanal. Chem.* **2015**, *747*, 39–44.

(24) Li, P.; Shu, J.; Shao, L.; Lin, X.; Wu, K.; Shui, M.; Wang, D.; Long, N.; Ren, Y. Comparison of Morphology and Electrochemical Behavior between PbSbO2Cl and PbCl2/Sb4O5Cl2. *J. Electroanal. Chem.* **2014**, *731* (3), 128–132.

Chapter 4:
Li-Pb Reaction Scheme*

INTRODUCTION

Wang et al. chemically synthesized a series of Li-Pb alloys and measured the equilibrium electrochemical potentials of electrodes made thereof, proposing the intermediates shown in Equation 4.1 through Equation 4.4 with a corresponding fully-lithiated phase of $Li_{4.5}Pb$.[1–4] However, Goward et al. reported that the most lithium-rich phase of lead is actually $Li_{17}Pb_4$ rather than $Li_{4.5}Pb$.[5] Additionally, X-ray diffraction (XRD) studies of the Li-Pb alloys formed from materials such as $Pb(NO_3)_2$/C,[6] $PbGeO_3$/graphene,[7] and PbSe[8] suggested different intermediate phases.

Equation 4.1: $Pb + Li \leftrightarrow LiPb$ $E_0 = 0.601$ V

Equation 4.2: $LiPb + 2\ Li \leftrightarrow Li_3Pb$ $E_0 = 0.449$ V

Equation 4.3: $Li_3Pb + 0.2\ Li \leftrightarrow Li_{3.2}Pb$ $E_0 = 0.374$ V

Equation 4.4: $Li_{3.2}Pb + 1.3\ Li \leftrightarrow Li_{4.5}Pb$ E0 = 0.292 V

In this chapter, the various Li-Pb phases were synthesized by dynamic electrochemical lithiation of pure Pb in 1M $LiPF_6$ in 1:1 fluoroethylene carbonate (FEC)/diethyl carbonate (DEC, 1:1 w/w) at room temperature. The compositions of the Li-Pb phases were determined by *ex situ* XRD measurement and compared to the coulometric data. Notably, the most lithium-rich compound of the phase diagram, $Li_{17}Pb_4$, was not reached during dynamic electrochemical lithiation. A similar discovery

* This work was previously published: Sean M. Wood, Codey H. Pham, Adam Heller, C. Buddie Mullins, "Stages in the Dynamic Electrochemical Lithiation of Lead", *J. Electrochem. Soc.*, 163 (2016) A1027 - A1029. The author of the dissertation was responsible for development of experiments, *ex situ* XRD measurements, and data analysis.

was made about the lithiation of silicon, which had historically been thought to have a final lithiation phase of $Li_{22}Si_5$ but was later found to only have an electrochemically-reachable phase of $Li_{15}Si_4$.[9]

EXPERIMENTAL INFORMATION

Lead electrodes were prepared by mixing 83% of -100 mesh Pb powder (Alfa Aesar), 7% of polyacrylonitrile (Sigma Aldrich, 150 kDa) binder, and 10% of Super P Li conductive carbon (Timcal) with enough dimethylformamide to form a viscous slurry, which was coated onto copper foil and dried in a vacuum oven at 120 °C for at least 6 h. The resulting composite film was punched into disks that formed the working electrodes of CR 2032 coin-type cells. Each electrode had an average Pb mass loading of 2.4 – 2.6 mg cm^{-2}. Prior to assembly into coin cells, each electrode was soaked in a 1 wt% aqueous solution of disodium ethylenediaminetetraacetic acid (EDTA) for approximately five minutes to remove any surface oxide. The electrodes were then rinsed with deionized water and ethanol and immediately transferred into an argon-filled glove box to prevent re-oxidation. Cells were assembled with Li foil as the counter/reference electrode and Celgard 2400 polypropylene membrane as the separator. A solution of 1M $LiPF_6$ in fluoroethylene carbonate (Solvay Fluor)/diethyl carbonate (1:1 w/w) was used as the electrolyte. Electrochemical measurements were performed on an Arbin BT 2143 multichannel battery testing system.

For the *ex situ* XRD, electrodes were discharged or charged to a particular potential vs. Li/Li^+ in a series of coin cells. Open circuit potentials were measured after allowing cells to relax for 48 h. Each coin cell was opened in the glove box, and the electrode was extracted and rinsed lightly with DEC to remove any residual $LiPF_6$ salt. The electrode was taped to a glass slide using air- and humidity-impermeable Kapton

tape, and its XRD spectrum was measured using a Rigaku MiniFlex 600 diffractometer with a Cu Kα radiation source at 40 kV and 15 mA. To correct for height errors introduced by securing the electrode to the glass slide, all XRD spectra were shifted using the Cu (1 1 1) peak as an internal reference, aligning it to a 2θ value of 43.342° (JCPDS Card #01-070-3039).[10]

RESULTS & DISCUSSION

Lead electrodes were lithiated and delithiated at a rate of 30 mA g^{-1} (~C/15) to generate the voltage profiles seen in Figure 4.1. During lithiation, two flat voltage plateaus were seen at 0.55 V and 0.40 V vs Li/Li^+, indicative of two-phase transitions. Below 0.30 V, a sloping voltage profile was seen. During delithiation, two sloping voltage plateaus were seen between 0.30 V and 0.45 V, and two flat voltage plateaus were seen at 0.47 V and 0.62 V.

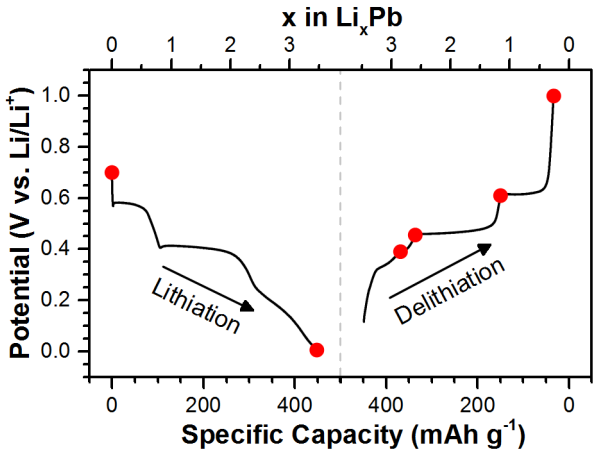

Figure 4.1. Lithiation/delithiation potential profiles for a lead electrode cycled at a specific current of 30 mA g^{-1} (~C/15). The red dots indicate the points of extraction of electrodes from the cells for *ex situ* XRD measurements.

The XRD spectra of the electrodes extracted at each of the red points in Figure 4.1 are shown in Figure 4.2. The points were chosen during delithiation in the voltage plateaus that were well-defined. The pristine electrode exhibited only the expected pure lead and copper substrate peaks. When lithiated to 5 mV (which relaxed to a potential of 0.24 V vs. Li/Li^+), two lead compounds were present: Li_3Pb and Li_7Pb_2; there was no $Li_{4.5}Pb$ or $Li_{17}Pb_4$ detected. Therefore, the phase that was richest in lithium was Li_7Pb_2. One potential reason for the discrepancy between the presently observed phases and those of Wang et al. is that their Li-Pb compounds were synthesized chemically followed by electrochemical measurement of their potentials, all of which was performed at equilibrium conditions. Conversely, the compounds discussed in the present study were synthesized *in situ* under dynamic electrochemical conditions that may be more characteristic of those found in lithium-ion batteries. We believe that the different synthesis methods are the root cause of the disparate reaction sequences and observed phases.

When the electrodes were delithiated to 0.39 V and 0.46 V (which relaxed to potentials of 0.34 and 0.44 V, respectively), the observed phases were LiPb, Li_8Pb_3, and Pb, their ratio varying slightly at the two potentials. The mixed phases and unexpected early presence of Pb were most likely caused by the different sizes of the Pb particles used to make the electrodes. Tin particles of different size have been shown to lithiate/delithiate at different rates, leading to a non-uniform distribution of varying Li_xSn phases.[11,12] In our Li-Pb system, the smallest particles may also delithiate completely before the larger particles, leading to the presence of phases that are not at their reversible potentials.

Upon further delithiation to 0.61 V, all of the Li_8Pb_3 was absent from the spectrum, leaving only LiPb and Pb in similar amounts. During the final delithiation to

1.00 V (which relaxed to a potential of 0.60 V), nearly all of the LiPb disappeared. The residual LiPb may remain because of either a) incomplete delithiation due to sluggish kinetics or b) fracturing of the particles caused by the massive volume change during lithiation/delithiation which leaves portions of particles electrically isolated and unavailable for further reaction. When lithiated to its final phase of Li_7Pb_2, the Pb volume increases by 177%.

Based on these XRD spectra, we propose the series of reactions for the lithiation of lead shown in Equation 4.5 through Equation 4.8. In Figure 4.3, these reactions were incorporated into the charge/discharge curves from Figure 4.1, showing good agreement of our proposed steps with the experimental data both in terms of the potentials of the observed plateaus and the coulometrically-reached final phase. Using these reactions, the theoretical capacity of lead as a lithium-ion battery anode material is 453 mAh g^{-1}, and it has an average lithiation potential of 0.45 V vs. Li/Li^+.

Equation 4.5: $Pb + Li \leftrightarrow LiPb$ $E_0 = 0.60$ V

Equation 4.6: $LiPb + \frac{5}{3} Li \leftrightarrow Li_8Pb_3$ $E_0 = 0.44$ V

Equation 4.7: $Li_8Pb_3 + \frac{1}{3} Li \leftrightarrow Li_3Pb$ $E_0 = 0.34$ V

Equation 4.8: $Li_3Pb + \frac{1}{2} Li \leftrightarrow Li_7Pb_2$ $E_0 = 0.24$ V

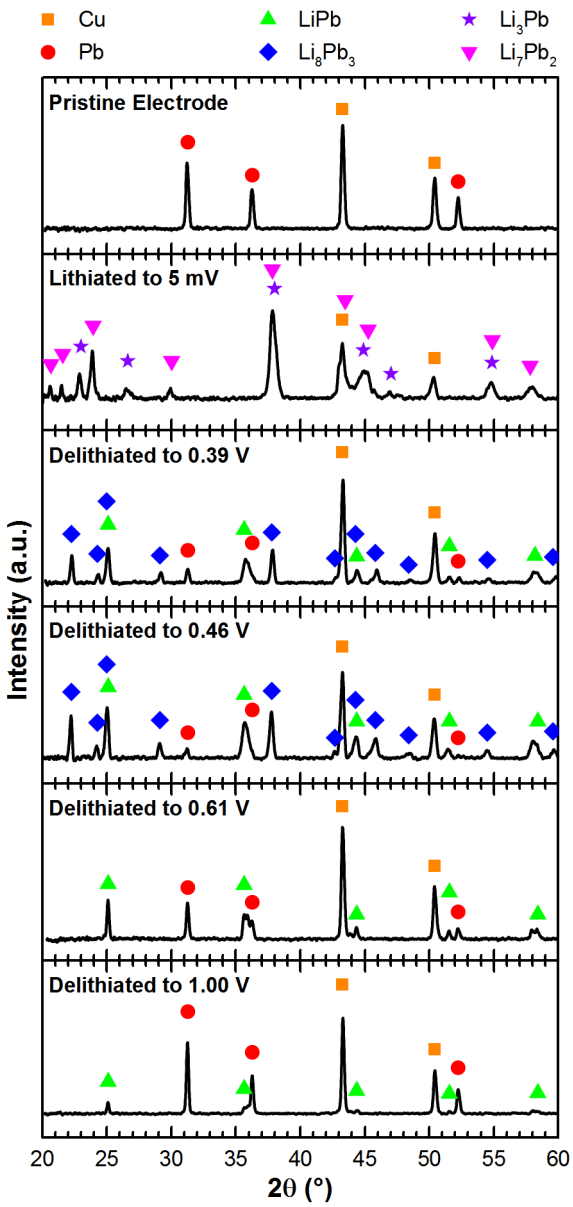

Figure 4.2. *Ex situ* XRD spectra of lead electrodes extracted at the points indicated in Figure 4.1.

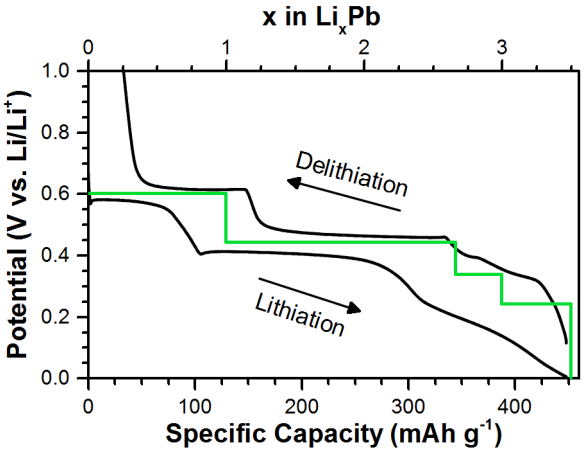

Figure 4.3. Lithiation/delithiation potential profiles for a lead electrode cycled at a 30 mA g^{-1} (~C/15) specific current. The green line shows the proposed (de)lithiation sequence.

REFERENCES

(1) Wang, J.; King, P.; Huggins, R. Investigations of Binary Lithium-Zinc, Lithium-Cadmium and Lithium-Lead Alloys as Negative Electrodes in Organic Solvent-Based Electrolyte. *Solid State Ionics* **1986**, *20*, 185–189.

(2) Huggins, R. Alloy Negative Electrodes for Lithium Batteries Formed in-Situ from Oxides. *Ionics (Kiel).* **1997**, *3*, 245–255.

(3) Huggins, R. Lithium Alloy Negative Electrodes. *J. Power Sources* **1999**, *81-82*, 13–19.

(4) Huggins, R. Lithium Alloy Negative Electrodes Formed from Convertible Oxides. *Solid State Ionics* **1998**, *113-115* (1-2), 57–67.

(5) Goward, G. R.; Taylor, N. J.; Souza, D. C. S.; Nazar, L. F. The True Crystal Structure of Li17M4 (M=Ge, Sn, Pb)-Revised from Li22M5. *J. Alloys Compd.* **2001**, *329* (1-2), 82–91.

(6) Wang, D.; Wu, K.; Shao, L.; Shui, M.; Ma, R.; Lin, X.; Long, N.; Ren, Y.; Shu, J. Facile Fabrication of Pb(NO3)2/C as Advanced Anode Material and Its Lithium Storage Mechanism. *Electrochim. Acta* **2014**, *120* (3), 110–121.

(7) Wang, J.; Feng, C.-Q.; Sun, Z.-Q.; Chou, S.-L.; Liu, H.-K.; Wang, J.-Z. In-Situ One-Step Hydrothermal Synthesis of a Lead Germanate-Graphene Composite as a Novel Anode Material for Lithium-Ion Batteries. *Sci. Rep.* **2014**, *4* (7030), 1–7.

(8) Xie, J.; Tu, F.; Su, Q.; Du, G.; Zhang, S.; Zhu, T.; Cao, G.; Zhao, X. *In situ* TEM Characterization of Single PbSe/reduced-Graphene-Oxide Nanosheet and the Correlation with Its Electrochemical Lithium Storage Performance. *Nano Energy* **2014**, *5*, 122–131.

(9) Obrovac, M. N.; Christensen, L. Structural Changes in Silicon Anodes during Lithium Insertion/Extraction. *Electrochem. Solid-State Lett.* **2004**, *7* (5), A93–A96.

(10) van de Krol, R.; Goossens, A.; Meulenkamp, E. A. *In situ* X-Ray Diffraction of Lithium Intercalation in Nanostructured and Thin Film Anatase TiO2. *J. Electrochem. Soc.* **1999**, *146* (9), 3150–3154.

(11) Gonzalez, J.; Sun, K.; Huang, M.; Dillon, S.; Chasiotis, I.; Lambros, J. X-Ray Microtomography Characterization of Sn Particle Evolution during Lithiation/delithiation in Lithium Ion Batteries. *J. Power Sources* **2015**, *285*, 205–209.

(12) Ebner, M.; Marone, F.; Stampanoni, M.; Wood, V. Visualization and Quantification of Electrochemical and Mechanical Degradation in Li Ion Batteries. *Science (80-.).* **2013**, *342* (6159), 716–720.

Chapter 5:
PbO vs. PbTe[†]

INTRODUCTION

One recent method for improving the stability and rate capabilities of alloy anodes is to combine them with chalcogenides,[1,2] as Abel et al. did in their recent work.[3] The addition of small amounts of Se in Ge allowed for superfast charge/discharge rates while maintaining high capacities. Li_2Se and Li_2Te act as superionic conductors in such systems,[4–6] greatly improving the diffusion of Li^+ ions throughout the particle. Tu et al. were able to achieve capacities of 500 mA h g^{-1} that faded to 300 mA h g^{-1} after 100 cycles with their graphene-sandwiched PbTe nanoparticles.[7] Additionally, the addition small amounts of Te to Ge also improved its performance over plain Ge.[8]

This chapter follows a similar approach by combining Pb with Te to form lead telluride, PbTe, with the intention of improving the capacity, stability, and rate capability of Pb-based materials. Here, synthetic details and electrochemical characterization results for PbO and PbTe nanoparticles are presented. PbTe exhibited stable cycling at a C/5 rate and maintained its stability at rates up to 10C. It was compared with PbO, and it is believed that the superionic conductivity of Li_2Te was responsible for the improved performance. Because of these characteristics, this material would be particularly well-suited for use in a low power application such as cellular telephones. For a typical 2,100 mA h cell phone battery, replacing the graphite in the battery with PbTe could increase its weight by about 6.5 g (less than the weight of three U.S. dimes) and its active material cost by just over one U.S. dollar. This tradeoff would allow for a slight reduction in the

[†] This work was previously published: Sean M. Wood, Kyle C. Klavetter, Adam Heller, C. Buddie Mullins, "Fast lithium transport in PbTe for lithium-ion battery anodes", *J. Mater. Chem. A*, 2 (2014) 7238-7243. The author of the dissertation was responsible for development and execution of all experiments, as well as data analysis.

volume of the anode and the option for rapid constant-current charging (0 – 100% in 30 minutes) without the risk of electroplating.

EXPERIMENTAL INFORMATION

Synthesis and Characterization

All chemicals were purchased from Sigma-Aldrich, unless otherwise noted, and used as received. Based on a procedure by Zhu et al.,[9] PbTe nanoparticles were prepared as follows. 10 g of NaOH were dissolved in 100 mL of water with stirring, and the solution was heated to 100 °C. To the hot solution, 5 mmol of Te powder and 5 g of $NaBH_4$ were added; the solution turned purple-black with stirring. A second solution of 5 mmol $Pb(NO_3)_2$ in 10 mL of water was prepared and added dropwise to the first solution. The mixture was reacted at 100°C for 30 minutes and allowed to cool to room temperature. The resultant PbTe particles were collected by centrifugation and washed three times with distilled water and once with absolute ethanol. They were then dried in a vacuum oven at 70°C overnight.

To prepare massicot PbO nanoparticles,[10] a first solution was created by adding 15.9 g of $Pb(NO_3)_2$ to 40 mL of distilled H_2O, stirring, and heating to 90 °C. A second solution was created by adding 30.4 g of NaOH to 40 mL of water (19 M) with stirring. Both of these solutions must be prepared in quartz glassware. If borosilicate glass is used, a small amount of SiO_2 must be added. If Teflon beakers are used, the litharge form of PbO will be synthesized. The first solution was quickly poured into the second solution and allowed to stir for about 30 seconds. Stirring was stopped and the solution sat for another 60 seconds to allow the particles to settle. The solution was decanted and the particles were rinsed with ice cold distilled water. The particles were then centrifuged and

washed three times with distilled water and absolute ethanol. The particles were dried in a vacuum oven at 70 °C overnight.

X-Ray Diffraction (XRD) measurements were performed on a Spider R-axis diffractometer with a Cu Ka radiation source at 40 kV and 40 mA. Scanning Electron Microscopy (SEM) micrographs were obtained using a Hitachi S-5500 electron microscope.

Electrochemical Measurements

An aqueous slurry of PbTe nanoparticles (60 wt%), 90 kDa carboxymethyl cellulose (20 wt%) binder, and Super P Li conductive carbon (Timcal, 20 wt%) was slurry cast onto copper foil and dried in a vacuum oven at 120°C for at least 6 h. This film was punched into disks that formed the working electrodes of CR 2032 coin-type cells. Each electrode had a PbTe mass loading of approximately 0.3 – 0.4 mg cm^{-2}. PbO electrodes were prepared by forming a slurry comprised of as-prepared PbO nanoparticles (40 wt %), polyacrylonitrile (20 wt %) binder,[11] and Super P Li conductive carbon (Timcal, 40 wt %), using dimethylformamide as the solvent. This formulation was selected because the particles did not create a functioning slurry with the carboxymethyl cellulose/water preparation. The use of polyacrylonitrile as a binder does not significantly affect the cycling results. The slurry was cast onto copper foil and dried in a vacuum oven at 120 °C for at least 6 h. This film was punched into disks that formed the working electrodes of CR 2032 coin-type cells. Each electrode had a mass of approximately 0.2 mg cm^{-2}. The cells were assembled in an argon-filled glovebox with Li foil as the counter and reference electrodes and Celgard 2400 polypropylene membrane as the separator. A solution of 1 M $LiPF_6$ in fluoroethylene carbonate (Solvay Fluor)/diethyl carbonate (1 : 1

w/w) was used as the electrolyte. Electrochemical measurements were performed on an Arbin BT 2043 or BT 2143 multichannel battery testing system.

RESULTS & DISCUSSION

The XRD spectrum of the synthesized black PbTe powder (Figure 5.1a) shows it to be phase-pure PbTe (Figure 5.1). As seen in the SEM micrograph in Figure 5.1c, the diameter of the particles was roughly 30 – 40 nm.

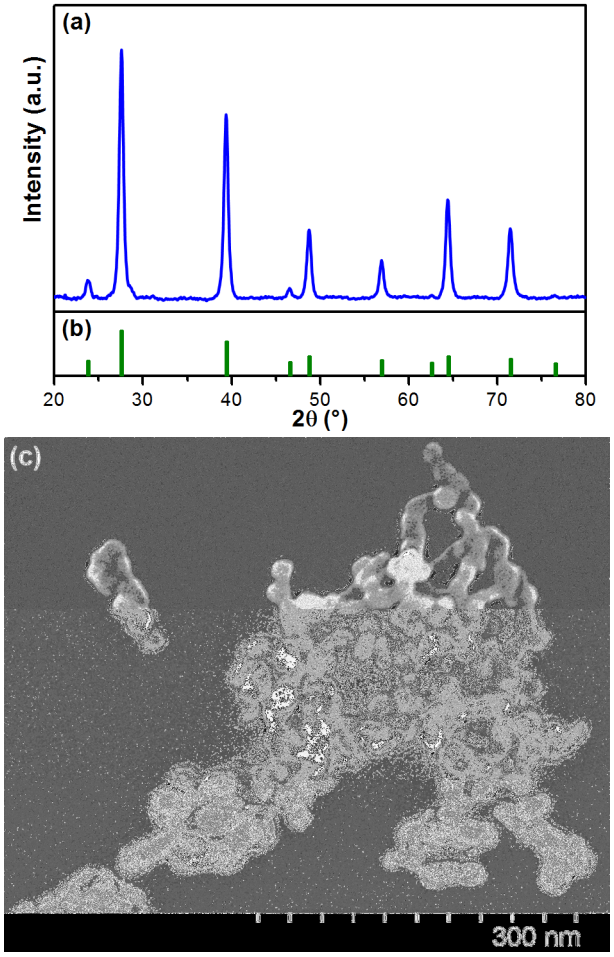

Figure 5.1. (a) XRD pattern of the as-synthesized PbTe nanoparticles. (b) PbTe reference spectrum (JCPDS # 01-072-6645). (c) SEM image of the PbTe nanoparticles.

The XRD spectrum of the synthesized gold-colored PbO powder (Figure 5.2a) shows that it was phase-pure massicot PbO (Figure 5.2b). SEM shows that the diameter of the particles was 50 – 60 nm (Figure 5.2c).

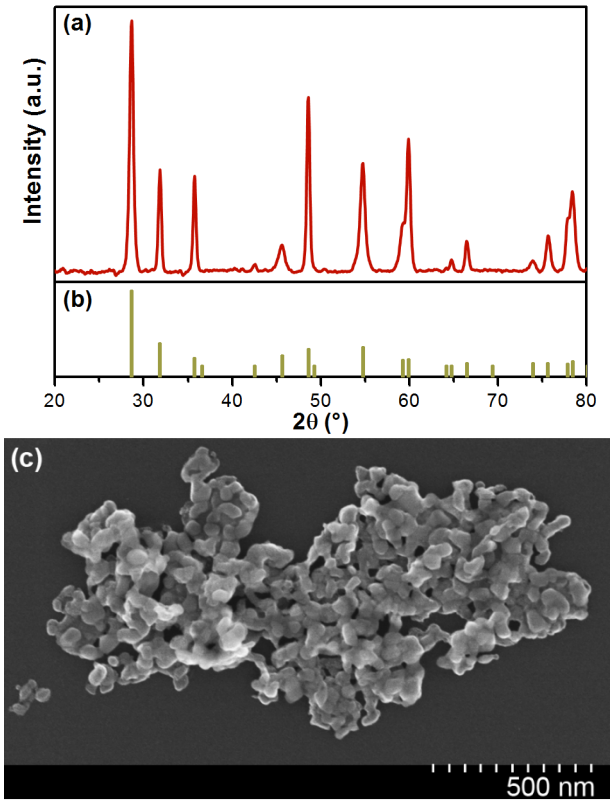

Figure 5.2. (a) XRD pattern of the as-synthesized PbO nanoparticles. (b) PbO reference spectrum (JCPDS # 01-076-1796). (c) SEM image of the PbO nanoparticles.

The third-cycle cyclic voltammogram of a PbTe electrode is shown in Figure 5.3a. Additional voltammograms, including those of the remaining cycles and of different voltage ranges, are shown in Figure 5.3b and Figure 5.3c. During the first lithium insertion half cycle, the PbTe was reduced to a series of Li-Pb and Li-Te alloys, which were seen in easy to distinguish, well-separated potential domains. The voltammograms show that the removal of Li from Pb and Te was facile and reversible. However, because of the much larger electronegativity difference between Li and O, Li_2O was much more

thermodynamically stable and its formation was therefore irreversible.[12] The stages of Li alloying with PbTe are given by Equation 5.1 though Equation 5.6 below. These reactions occurred sequentially during reduction/Li-insertion and in the opposite order for oxidation/Li-removal.

Equation 5.1: $3\ PbTe + Li \leftrightarrow 3\ Pb + LiTe_3$

Equation 5.2: $Pb + LiTe_3 + 5\ Li \leftrightarrow Pb + 3\ Li_2Te$

Equation 5.3: $Pb + Li + Li_2Te \leftrightarrow LiPb + Li_2Te$

Equation 5.4: $LiPb + \frac{5}{3}\ Li + Li_2Te \leftrightarrow Li_8Pb_3 + Li_2Te$

Equation 5.5: $Li_8Pb_3 + \frac{1}{3}\ Li + Li_2Te \leftrightarrow Li_3Pb + Li_2Te$

Equation 5.6: $Li_3Pb + \frac{1}{2}\ Li + Li_2Te \leftrightarrow Li_7Pb_2 + Li_2Te$

The voltammetric waves in the 0.8 – 2.5 V domain represent the formation and electrolysis of $LiTe_3$ and Li_2Te (Equation 5.1 and Equation 5.2), which are the only two stable crystalline phases of the Li-Te phase diagram,[13–15] as well as the recombination of Pb and Te to form PbTe. The four waves in the 0.01 – 0.7 V domain in Figure 5.3a for PbTe represent the stages of Li alloying with Pb, which are shown in Equation 5.3 through Equation 5.6.[16]

When the upper voltage range was limited to 0.7 V, only Li-Pb alloys were formed/electrolyzed while the Li_2Te remained fixed after initial formation and did not participate in cycling, and the theoretical capacity was 280 mA h g^{-1}. However if the upper limit was increased to 2.5 V, the Li-Te alloys were formed/electrolyzed in addition to the Li-Pb alloys, and the theoretical capacity increased to 440 mA h g^{-1}. Gravimetric and volumetric capacity cycling data for these two voltage ranges are shown in Figure 5.4, where 1C corresponds to 280 mA g^{-1} for both.

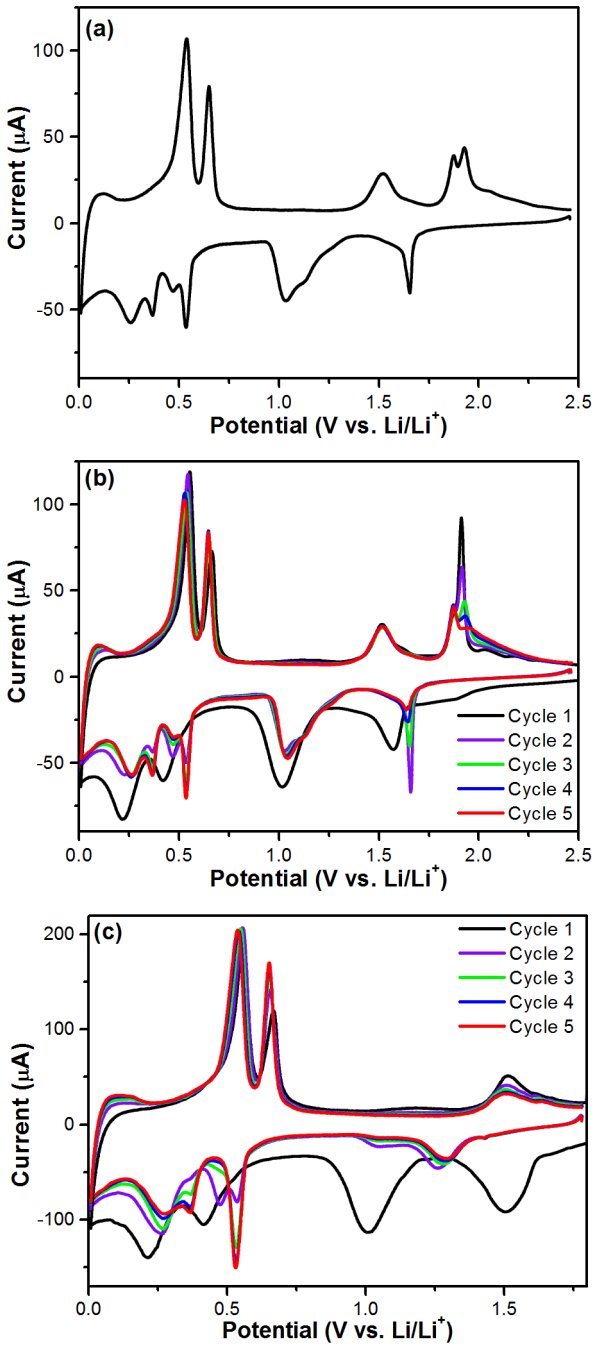

Figure 5.3. (a) Third cycle of cyclic voltammetry for PbTe nanoparticles in the potential range 0.01 – 2.5 V at a scan rate of 0.1 mV s^{-1}. Cycling voltammograms of PbTe at a scan rate of 0.1 mV s^{-1} in the voltage range (b) 0.01 – 2.5 V and (c) 0.01 – 1.8 V.

Figure 5.4a shows the PbTe cycled at a rate of C/5. When the potential cutoff was limited to 0.7 V (average discharge potential of 0.31 V), the capacity was stable at 250 mA h g^{-1} (2,100 mA h cm^{-3}) through 100 cycles. When the potential cutoff was raised to 2.5 V (average discharge potential of 0.69 V), the capacity was stable at 500 mA h g^{-1} (4,100 mA h cm^{-3}) through 100 cycles. Figure 5.4b shows the PbTe cycled at higher rates, with substantial capacity retention up to 5C and the absence of permanent damage after cycling at 10C. When the upper voltage cut-off was 0.7 V, the capacities were 250, 240, 210, 190, 170, 110, and 30 mA h g^{-1} at C/10, C/5, C/2, 1C, 2C, 5C, and 10C, respectively. When the C-rate was again lowered to C/10, the capacity fully recovered to 250 mA h g^{-1}. For a 2.5 V cutoff, the capacities were 530, 500, 490, 460, 430, 370, and 300 mA h g^{-1} at C/10, C/5, C/2, 1C, 2C, 5C, and 10C, respectively.

Coulombic efficiencies for PbTe in these two voltage ranges are shown in Figure 5.5. The Coulombic efficiency was over 99.5% when the upper voltage cut-off was kept at 0.7 V, but decreased to only 94 – 97% when the voltage range was expanded to a full 2.5 V.

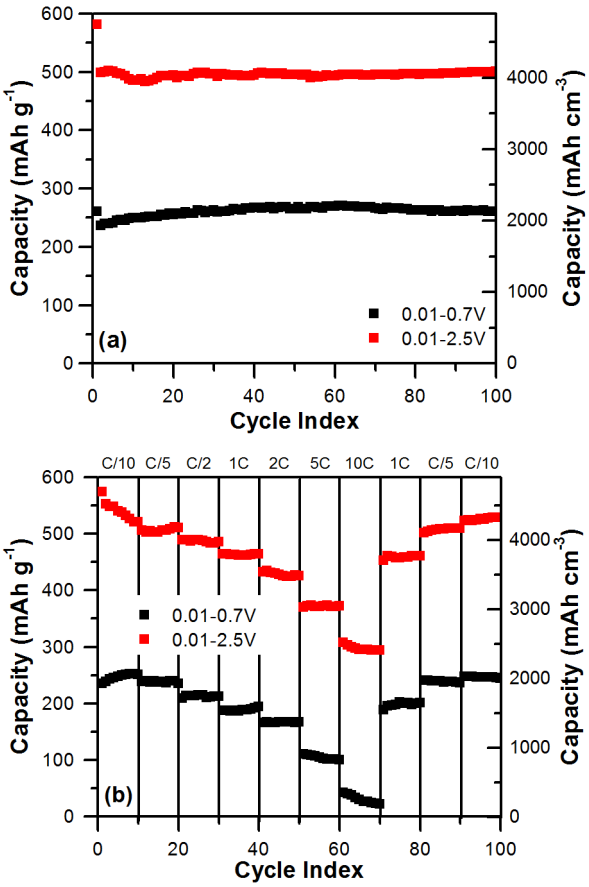

Figure 5.4. Discharge capacity vs. cycle index for PbTe in two potential ranges at (a) C/5 and (b) varying C-rates. Volumetric capacity is calculated by multiplying the specific gravimetric capacity by the density of PbTe.

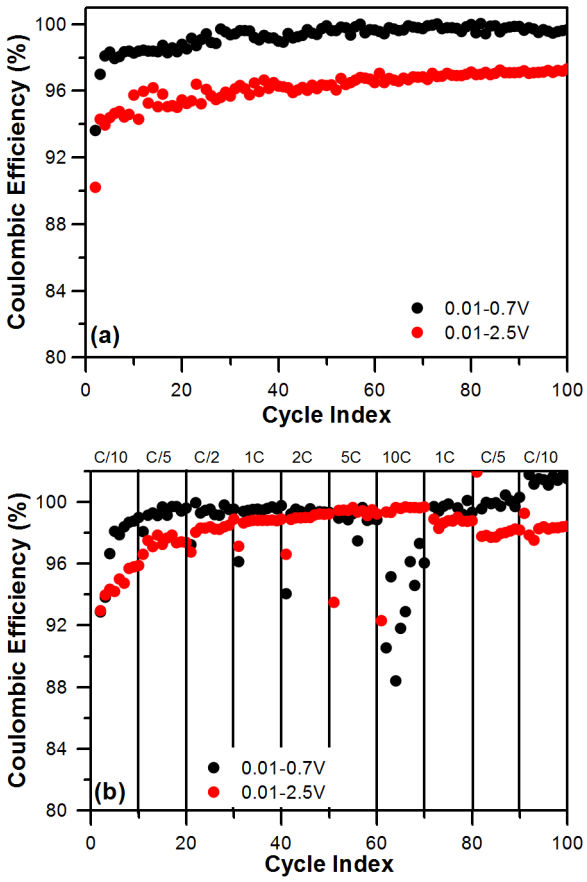

Figure 5.5. Coulombic efficiency versus cycle index for PbTe in two voltage ranges at (a) C/5 and (b) varying C-rates.

Figure 5.6a shows the PbO cycled at a rate of C/10. At both potential cutoffs, the capacity faded rapidly over the first twenty cycles, ending below 300 mAh g^{-1} after 100 cycles. Figure 5.6b shows the corresponding PbO rate-test cycling data. The PbO exhibited rapid capacity fading at all rates except for 1C, which had a capacity of 290 mA h g^{-1}. After returning to C/10, PbO again experienced rapid capacity fade.

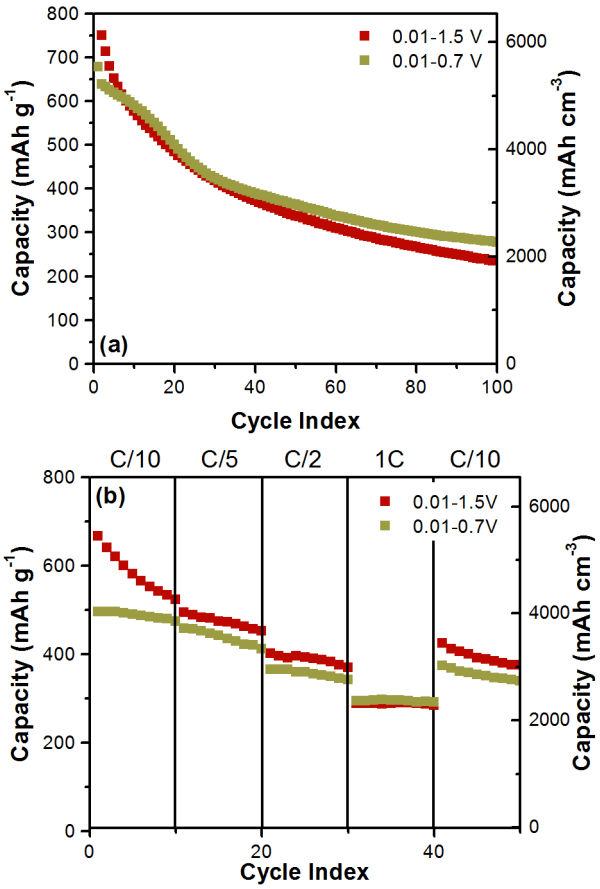

Figure 5.6. Discharge capacity vs. cycle index for PbO in two potential ranges at (a) C/10 and (b) varying C-rates. Volumetric capacity is calculated by multiplying the specific gravimetric capacity by the density of PbO.

Coulombic efficiencies for PbO in these two voltage ranges are shown in Figure 5.7. The Coulombic efficiency was well over 100% when the upper voltage cut-off was kept at 0.7 V, perhaps due to parasitic side reactions. It decreased to only 92 – 96% when the voltage range was expanded to a full 1.5 V.

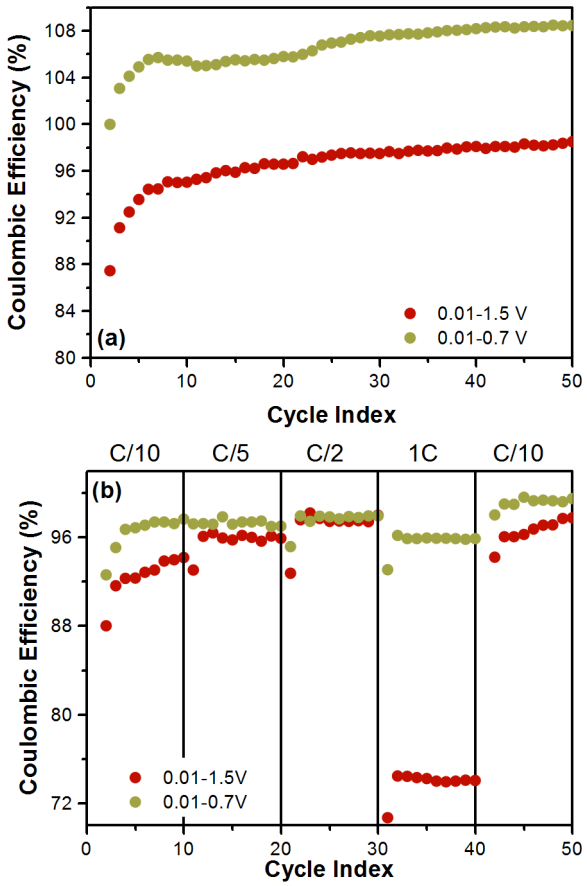

Figure 5.7. Coulombic efficiency versus cycle index for PbO in two voltage ranges at (a) C/5 and (b) varying C-rates.

In Figure 5.8, differential capacity profiles for PbTe are shown for each of the C-rates of Figure 5.4b in the 0.01 – 2.5 V range. The overpotentials exceeded 300 mV only at rates higher than 5C, where the anodic Li-Pb alloy peaks were up-shifted. One of the peaks eventually shifted past 0.7 V, which was consistent with the abrupt drop in capacity when the Li-Pb alloy was completely delithiated at these C-rates.

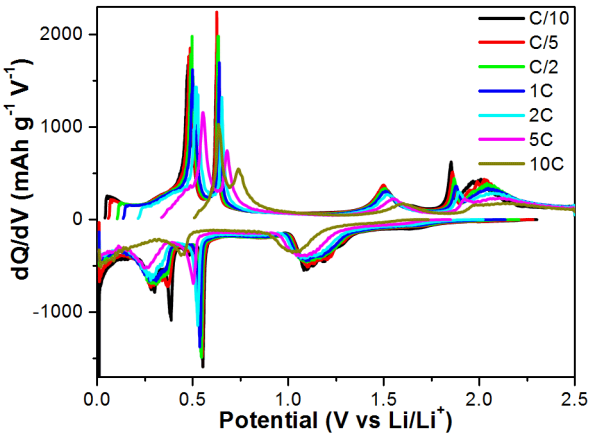

Figure 5.8. Differential capacity profiles for PbTe at varying C-rates over the voltage range 0.01 – 2.5 V.

Differential capacity profiles for select cycles are shown for both potential domains in Figure 5.9. As shown in Figure 5.9a, the nature of the Li-Pb alloys changed upon cycling: the peak pair at 0.28 V/0.52 V decreased as cycling progressed and completely disappeared by cycle 50. Concurrently, the pair at 0.37 V/0.48 V increased and then remained stable from cycle 50 to cycle 100. The peak pair at 0.56 V/0.63 V also increased as cycling progressed. This behavior was also seen below 0.7 V when the potential limit was extended to 2.5 V, as in Figure 5.9b. Three peak pairs were observed in the potential region between 0.7 V and 2.5 V, matching those in the voltammetric waves. The peak pair at 1.67 V/1.88 V, which was attributed to the reformation of PbTe following the delithiation of the Li-Pb and Li-Te alloys,[7] completely vanished after the 5th cycle. The lithiation of a PbTe particle is sequential: at higher potentials, Te is first lithiated to Li_2Te (with a 204% volume change), and then at lower potentials Pb is lithiated to Li_7Pb_2 (with a 277% volume change). We believe that the disappearance of this peak pair was a consequence of the mismatch in both the magnitude and the

sequence of the expansions in the PbTe particle, which unevenly strained the original PbTe lattice to the point of irreversible destruction during the initial cycles.

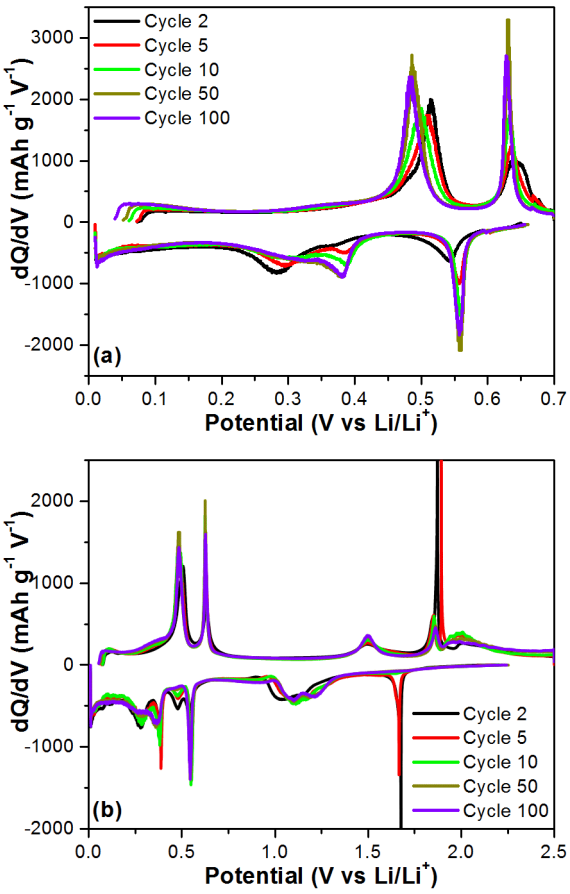

Figure 5.9. Differential capacity profiles for PbTe at C/5 over the potential range (a) 0.01 – 0.7 V and (b) 0.01 – 2.5 V.

The differential capacity profiles for the 10th cycle at C-rates of C/10, C/5, C/2, and 1C are shown in Figure 5.10a for PbTe and Figure 5.10b for PbO, corresponding to the cycling data of Figure 5.4b and Figure 5.6b, respectively. Greater upshifting of the peaks implies lesser stability (i.e. lower free energy of formation of the alloy or compound). Comparison of peak upshifting for PbTe and PbO showed increasing

destabilization caused by the stress associated with a higher C-rate, which was much greater for the PbO-based anode than it was for the PbTe-based anode. The PbO anode showed upshifting and severely diminished peak heights at a 1C rate; however, the PbTe anode showed little peak shifting with increasing C-rate and only minor attenuation of peak height at a 1C rate.

The extent of peak upshifting is summarized in the bar chart of Figure 5.10c, where the leftmost edge of each bar represents the potential of a cathodic peak and the rightmost edge represents the potential of its matching anodic peak. The values written within the bars represent the splitting of the anodic and cathodic wave pairs. The vertical line that runs through each set of bars is the reversible (thermodynamic) potential for a given Li-Pb alloying reaction. At all C-rates, the more negative the reversible potentials were, the greater was the splitting of their anodic and cathodic peaks. Furthermore, as expected for Li diffusion-limited electrode reaction rates, the splitting increased with the C-rate. The increases were much more pronounced for PbO than for PbTe, indicating that Li permeated more rapidly through Li_2Te than through Li_2O. For example, as the C-rate increased from C/10 to 1C, the peak splitting for PbTe increased by only about 32 – 34 mV, while for PbO it increased by 83 – 90 mV.

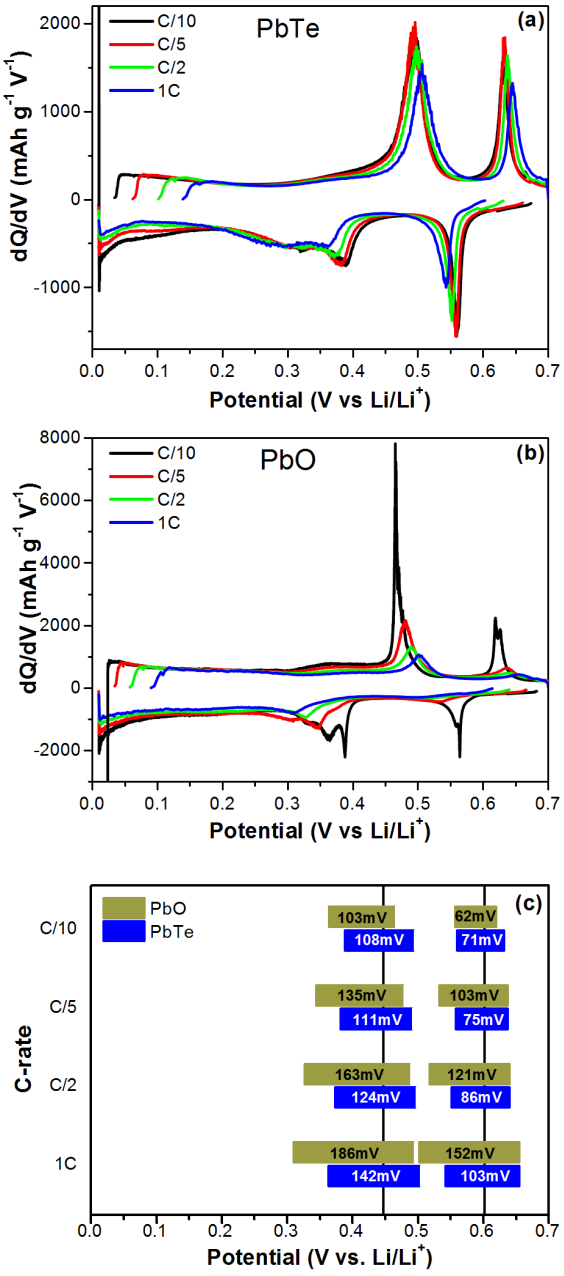

Figure 5.10. Differential capacity profiles at varying C-rates over the potential range 0.01 – 0.7 V for (a) PbTe and (b) PbO. (c) Bar plot comparing the positions and splittings of the peaks seen in (a) and (b). The left and right edges of each bar represent the position of the cathodic peak and anodic peak, respectively. The width of each bar represents the difference in potential between the two peaks (given by the text in each bar). The vertical line through each set of bars is the reversible potential for the given peak.

When electrode reactions of solids are too slow for the rate to be reactant diffusion-controlled, the peak width at half height of the differential capacity profiles is smaller for crystalline lattices than it is for non-crystalline materials. When reduced or oxidized species are identically bound as in crystalline materials, they are equipotential. In amorphous materials, the same species can be differently bound and are not equipotential. As seen in Figure 5.10a and Figure 5.10b, at the slowest C/10 rate several of the PbO peaks are sharp, indicative of crystalline order, while those of PbTe are broad, indicative of an amorphous structure. Amorphization of particles has been shown to occur during cycling,[17,18] indicated here by the broadening of the peaks at higher rates. The broadening of the PbO peaks was minor, and the peak width at half maximum was greater for PbTe relative to PbO, indicating greater amorphousness in the PbTe. When Li^+ diffuses by hopping between defects, its diffusional transport is enhanced by disorder such as an increased number of grain boundaries; diffusivities are 3 – 16 orders of magnitude higher along grain boundaries than in the crystalline lattice.[19] Evidently, the Li-Pb alloys formed by PbTe are less crystalline than those formed by PbO.

Figure 5.11a shows Galvanostatic Intermittent Titration Technique (GITT) measurements with the potential plotted vs. the capacity normalized to the theoretical value.[20] Current was pulsed at C/20 for one hour, followed by a three hour rest. The positions of the spikes represent the relaxation or equilibrium lithium insertion potentials. Larger spikes indicate larger Li insertion or stripping overpotentials. In Figure 5.11b, the overpotentials are plotted as a function of the number of lithium ions inserted. It is seen that Li insertion and stripping were facile only after Li_2Te was formed, supporting the hypothesis that Li_2Te is a superionic conductor, as suggested by computational models.[4]

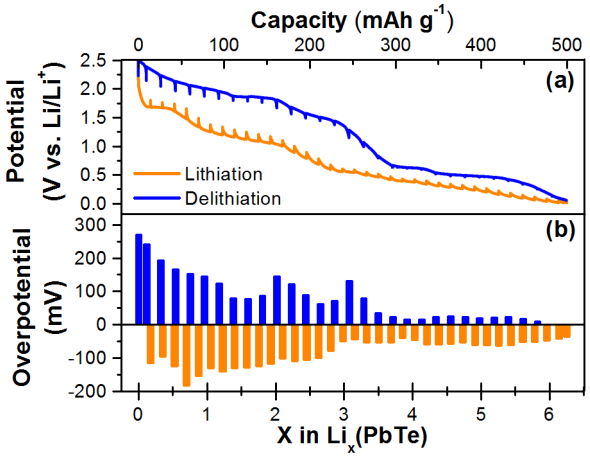

Figure 5.11. Galvanostatic intermittent titration technique (GITT) curve for the PbTe. The electrode was rested for 3 h after each hour-long charge or discharge cycle at a C/20 rate in a potential range of 0.01 – 2.5 V. (b) Overpotential values for each rest point as a function of the total number of lithiums inserted into the PbTe compound.

REFERENCES

(1) Im, H. S.; Cho, Y. J.; Lim, Y. R.; Jung, C. S.; Jang, D. M.; Park, J.; Shojaei, F.; Kang, H. S. Phase Evolution of Tin Nanocrystals in Lithium Ion Batteries. *ACS Nano* **2013**, *7* (12), 11103–11111.

(2) Cho, Y. J.; Im, H. S.; Kim, H. S.; Myung, Y.; Back, S. H.; Lim, Y. R.; Jung, C. S.; Jang, D. M.; Park, J.; Cha, E. H.; Cho, W. Il; Shojaei, F.; Kang, H. S. Tetragonal Phase Germanium Nanocrystals in Lithium Ion Batteries. *ACS Nano* **2013**, *7* (10), 9075–9084.

(3) Abel, P. R.; Klavetter, K. C.; Heller, A.; Mullins, C. B. Thin Nanocolumnar Ge0.9Se0.1 Films Are Rapidly Lithiated/Delithiated. *J. Phys. Chem. C* **2014**, *118*, 17407–17412.

(4) Kishida, I.; Koyama, Y.; Kuwabara, A.; Yamamoto, T.; Oba, F.; Tanaka, I. First-Principles Calculations of Migration Energy of Lithium Ions in Halides and Chalcogenides. *J. Phys. Chem. B* **2006**, *110* (16), 8258–8262.

(5) Eithiraj, R. D.; Jaiganesh, G.; Kalpana, G.; Road, S. P. First-Principles Study of Electronic Structure and Ground-State Properties of Alkali-Metal Selenides and Tellurides (M2A) [M: Li, Na, K; A: Se, Te]. *Int. J. Mod. Phys. B* **2009**, *23* (25), 5027–5037.

(6) Alay-e-Abbas, S. M.; Shaukat, a. FP-LAPW Calculations of Structural, Electronic, and Optical Properties of Alkali Metal Tellurides: M2Te [M: Li, Na, K and Rb]. *J. Mater. Sci.* **2010**, *46* (4), 1027–1037.

(7) Tu, F.; Huo, Y.; Xie, J.; Cao, G.; Zhu, T.; Zhao, X.; Zhang, S. Reduced Graphene Oxide Induced Confined Growth of PbTe Crystals and Enhanced Electrochemical Li-Storage Properties. *RSC Adv.* **2013**, *3* (45), 23612–23619.

(8) Powell, E. J.; Wood, S. M.; Heller, A.; Mullins, C. B. Obviating the Need for

Nanocrystallites in the Extended Lithiation/delithiation of Germanium. *J. Mater. Chem. A* accepted.

(9) Zhu, T. J.; Liu, Y. Q.; Zhao, X. B. Synthesis of PbTe Thermoelectric Materials by Alkaline Reducing Chemical Routes. *Mater. Res. Bull.* **2008**, *43* (11), 2850–2854.

(10) Perry, D. L.; Wilkinson, T. J. Synthesis of High-Purity α- and β-PbO and Possible Applications to Synthesis and Processing of Other Lead Oxide Materials. *Appl. Phys. A* **2007**, *89* (1), 77–80.

(11) Gong, L.; Nguyen, M. H. T.; Oh, E.-S. High Polar Polyacrylonitrile as a Potential Binder for Negative Electrodes in Lithium Ion Batteries. *Electrochem. commun.* **2013**, *29*, 45–47.

(12) Zhao, X. B.; Cao, G. S.; Lv, C. P.; Zhang, L. J.; Hu, S. H.; Zhu, T. J.; Zhou, B. C. Electrochemical Properties of Some Sb or Te Based Alloys for Candidate Anode Materials of Lithium-Ion Batteries. *J. Alloys Compd.* **2001**, *315* (1-2), 265–269.

(13) Cunningham, P.; Johnson, S.; Cairns, E. Phase Equilibria in Lithium-Chalcogen Systems III. Lithium-Tellurium. *J. Electrochem. Soc.* **1973**, *120* (3), 328–330.

(14) Morachevskii, A. Thermodynamic Analysis of Alloying in the System Lithium-Tellurium. *Russ. J. Appl. Chem.* **2001**, *74* (4), 564–568.

(15) Valentine, D. Y.; Cavin, O. B.; Yakel, H. L. On the Crystal Structure of LiTe3. *Acta Crystallogr.* **1977**, *B33*.

(16) Wood, S. M.; Pham, C. H.; Heller, A.; Mullins, C. B. Stages in the Dynamic Electrochemical Lithiation of Lead. *J. Electrochem. Soc.* **2016**, *163* (6), A1027–A1029.

(17) McDowell, M. T.; Lee, S. W.; Nix, W. D.; Cui, Y. 25th Anniversary Article: Understanding the Lithiation of Silicon and Other Alloying Anodes for Lithium-Ion Batteries. *Adv. Mater.* **2013**, *25* (36), 4966–4985.

(18) Fan, S.; Lim, L. Y.; Tay, Y. Y.; Pramana, S. S.; Rui, X.; Samani, M. K.; Yan, Q.; Tay, B. K.; Toney, M. F.; Hng, H. H. Rapid Fabrication of a Novel Sn–Ge Alloy: Structure–property Relationship and Its Enhanced Lithium Storage Properties. *J. Mater. Chem. A* **2013**, *1* (46), 14577.

(19) Han, S.; Park, J.; Lu, W.; Sastry, A. M. Numerical Study of Grain Boundary Effect on Li+ Effective Diffusivity and Intercalation-Induced Stresses in Li-Ion Battery Active Materials. *J. Power Sources* **2013**, *240*, 155–167.

(20) Ding, N.; Xu, J.; Yao, Y. X.; Wegner, G.; Fang, X.; Chen, C. H.; Lieberwirth, I. Determination of the Diffusion Coefficient of Lithium Ions in Nano-Si. *Solid State Ionics* **2009**, *180* (2-3), 222–225.

Chapter 6:
PbS‡

INTRODUCTION

PbS was studied earlier by Sanusi et al.,[1] but they only elucidated the lithiation mechanism and did not attempt to cycle it. Past studies have found that GeS[2,3] and SnS[4] exhibit improved cycling performance over their base-metal and oxide counterparts. In this chapter, PbS nanoparticles were synthesized via a facile wet chemical route and galvanostatically cycled to probe whether PbS confers similar benefits over Pb and PbO. When cycled in the 0.01 – 1.0 V range, the electrodes did not lose their sulfur; when cycled in the 0.01 – 3.0 V range, they lost their sulfur through lithium polysulfide dissolution. Following the dissolution of sulfur, the specific capacities were similar for 100 cycles whether the cutoff was 1.0 V or 3.0 V, decreasing to less than 200 mAh g^{-1} after 100 cycles.

EXPERIMENTAL INFORMATION

Synthesis and Characterization

All chemicals were purchased from Sigma-Aldrich, unless otherwise noted, and used as received. Based on a procedure by Zhang et al.,[5] PbS nanoparticles were prepared as follows. 10 mmol of elemental sulfur was added to 100 mL of deionized water with magnetic stirring. 0.2 mol of NaOH was added in order to dissolve the sulfur. The solution was heated to ~80 °C to facilitate dissolution of the sulfur. The solution was dark yellow, but still transparent. A second solution was created by dissolving 10.2 mmol of $Pb(Ac)_2 \bullet 3H_2O$ in 10 ml of DI water. The first solution was allowed to cool to room

‡ This work was previously published: Sean M. Wood, Emily J. Powell, Adam Heller, C. Buddie Mullins, "Lithiation and Delithiation of Lead Sulfide (PbS)", *J. Electrochem. Soc.*, 162 (2015) A1182-A1185. The author of the dissertation was responsible for development and execution of all experiments, as well as data analysis.

temperature, and the second solution was added all at once. A black precipitate appeared immediately. The resultant PbS particles were collected by centrifugation and washed twice with DI water and once with acetone. They were then dried under vacuum at 70 °C overnight.

X-Ray Diffraction (XRD) measurements were performed on a Spider R-axis diffractometer with a Cu Kα radiation source at 40 kV and 40 mA. Scanning Electron Microscopy (SEM) micrographs were obtained using a Hitachi S-5500 electron microscope.

Electrochemical Measurements

A slurry of PbS nanoparticles (60 wt%), polyacrylonitrile (20 wt%) binder,[6] and Super P Li conductive carbon (Timcal, 20 wt%) with dimethylformamide as the solvent was coated onto copper foil and dried in a vacuum oven at 120 °C for at least 6 h. This film was punched into disks that formed the working electrodes of CR 2032 coin-type cells. Each electrode had a PbS mass loading of approximately 0.5 mg cm^{-2}. The cells were assembled in an argon-filled glove box with Li foil as the counter and reference electrodes and Celgard 2400 polypropylene membrane as the separator. A solution of 1 M $LiPF_6$ in fluoroethylene carbonate (Solvay Fluor)/diethyl carbonate (1:1 w/w) was used as the electrolyte. Electrochemical measurements were performed on an Arbin BT 2143 multichannel battery testing system.

RESULTS & DISCUSSION

The XRD spectrum of the synthesized black powder is shown in Figure 6.1a, and it matches with the galena reference spectrum (JCPDS # 01-077-0244), confirming that the material was phase-pure galena PbS. An SEM micrograph (Figure 6.1b) shows that

the synthesized particles were roughly 50 – 100 nm in size with a rough texture and nonspherical shape.

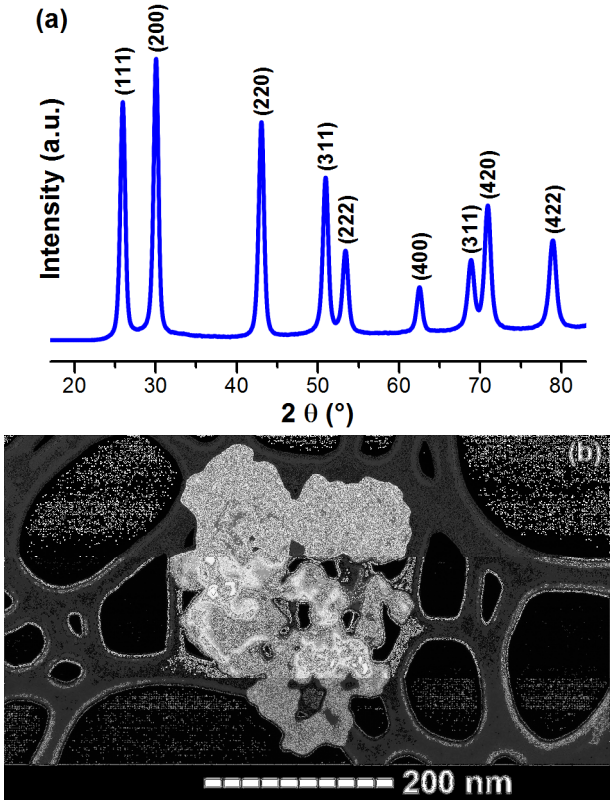

Figure 6.1. (a) XRD pattern of the PbS nanoparticles. (b) SEM image of the PbS nanoparticles.

The first two cyclic voltammetry cycles for a PbS electrode are shown in Figure 6.2, conducted at a scan rate of 0.1 mV s^{-1}. The pairs of reduction/oxidation peaks at potentials positive of 1.0 V vs. Li/Li^+ correspond to sequential formation of polysulfides and Li_2S according to Equation 6.1 and Equation 6.2.[3,4] The reduction/oxidation peaks negative of 1.0 V correspond to the sequential formation of Li-Pb alloys: LiPb, Li_8Pb_3, Li_3Pb, and Li_7Pb_2.[7] The overall lithium-lead alloying reaction is given in Equation 6.3.

Equation 6.1: $PbS + \frac{2}{n} Li \leftrightarrow Pb + \frac{1}{n} Li_2S_n$

Equation 6.2: $Pb + \frac{1}{n} Li_2S_n + (2 - \frac{2}{n}) Li \leftrightarrow Pb + Li_2S$

Equation 6.3: $Pb + 3.5\ Li + Li_2S \leftrightarrow Li_{3.5}Pb + Li_2S$

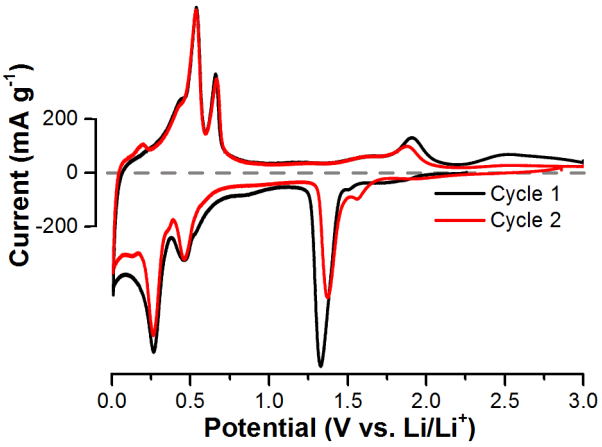

Figure 6.2. First two cycles of cyclic voltammetry for PbS nanoparticles in the potential range 0.01 – 3.0 V vs. Li/Li^+ at a scan rate of 0.1 mV s^{-1}.

The reduction peaks positive of 1.0 V vs. Li/Li^+ shift toward a more positive potential after the first cycle, indicating an activation step in which there is an overpotential associated with nucleation during the initial lithiation.[8,9] These peaks' magnitudes also shrink going from cycle 1 to cycle 2 due to irreversible dissolution of lithium polysulfide, a problem common in sulfur and sulfur-based electrodes.[10–13] The reduction peaks negative of 1.0 V vs. Li/Li^+ do not shift potentials in going from cycle 1 to cycle 2, but the magnitude of the current density is larger for the first cycle due to the initial solid electrolyte interphase (SEI) layer formation at potentials lower than about 1.1 V.[14]

According to the reactions above, there are two different theoretical capacities depending on the voltage cutoff. Negative of 1.0 V the lead is lithiated/delithiated. With

3.5 Li ions reversibly reacting as in Equation 6.3, the theoretical specific capacity is 392 mAh g^{-1}. If the upper cutoff is extended to 3.0 V and if the reaction remains reversible (i.e. sulfur is not irreversibly extracted from the electrode by formation of lithium polysulfides), then 2 more Li ions react as in Equation 6.1 and Equation 6.2, providing a total theoretical specific capacity of 616 mAh g^{-1}.

The results for galvanostatic cycling in the potential ranges 0.01 V ↔ 1.0 V and 0.01 V ↔ 3.0 V are shown in Figure 6.3. The electrodes were first cycled at a C/20 rate for a single conditioning cycle, and then at a 1 C rate for 100 cycles. The electrodes exceeded their theoretical capacities on the C/20 cycle, reaching 455 mAh g^{-1} for the 1.0 V cutoff and 689 mAh g^{-1} for the 3.0 V cutoff. After 10 cycles, cycling to either 1 V or 3 V provided nearly identical capacities for the 11th through 100th cycles. Through the 20th cycle a capacity of around 400 mAh g^{-1} was maintained. After the 20th cycle the capacities faded, dropping to about 140 mAh g^{-1} at the 100th cycle.

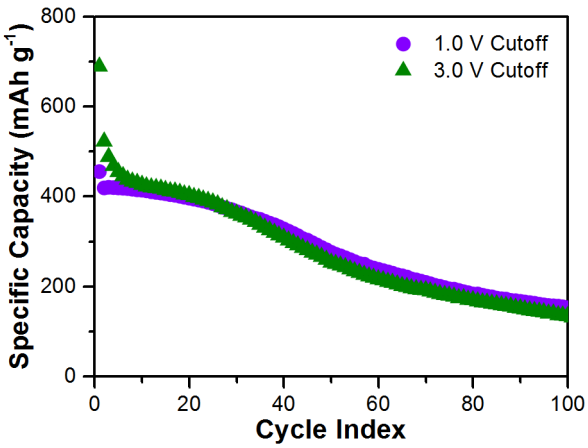

Figure 6.3. Discharge capacity versus cycle index in two potential ranges at a rate of 1 C following one C/20 conditioning cycle.

The capacity-voltage profiles in Figure 6.4 reveal why cycling to the different cutoff potentials provided similar capacities after the 10th cycle. The large plateau in cycle 2 at 1.4 V is associated with the reversible reaction of lithium with PbS, as in Equation 6.1 and Equation 6.2. This plateau rapidly decreased throughout the first ten cycles (shown by the arrow in Figure 6.4) and was nearly absent by the tenth cycle. Its fading is consistent with the loss of sulfur through lithium polysulfide dissolution.[13] After ten cycles, electrodes cycled only to 1.0 V contain both Pb and Li_2S, whereas those cycled to 3.0 V contain only Pb. The lower potential lead-lithium alloying features persist, irrespective of the presence or absence of Li_2S.

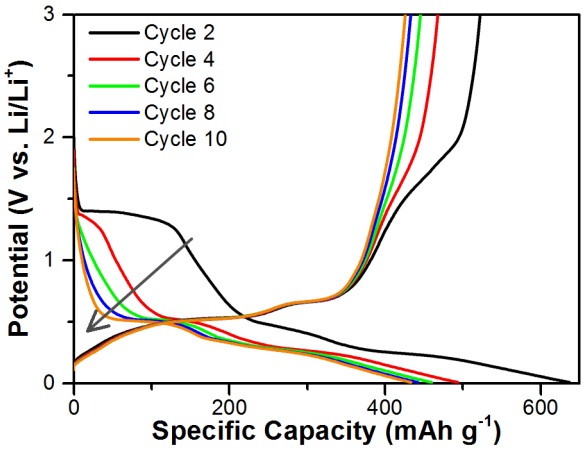

Figure 6.4. The first five even-numbered capacity-voltage profiles for an electrode cycled in the potential range 0.01 – 3.0 V at a rate of 1 C.

Figure 6.5a shows that the 0.4 – 0.5 V reduction peak shifts toward lower potentials during cycling, and Figure 6.5b tracks this peak as a function of cycle index. The peak's potentials became more positive for both systems for the first few cycles, which is indicative of an activation step after which this lithium insertion reaction becomes more facile. The peak then begins to shift toward more negative potentials for

both systems. Upon cycling only to 1.0 V the peak-potential downshift is much slower than upon cycling to 3.0 V. One possible reason the peak may shift negative during cycling is that the particles undergo massive expansion and contraction during cycling (277% in going from Pb to $Li_{3.5}Pb$),[7] experiencing significant strain and fracture. This destruction sometimes electrically isolates particle fragments, making them unavailable to participate in the lithiation reactions. When this occurs, the remaining electrically connected particles experience a higher current density (i.e., the same current is now being applied to a smaller mass). Higher current densities cause higher overpotentials and a negative shift of the reduction peak. Upon cycling to 3.0 V in our system, the 0.4 – 0.5 V reduction peak shifts negative more quickly and earlier in cycling, indicating a higher current density and thus a larger loss of active material via this mechanism. This behavior should correlate to a more rapid capacity fade. However, because there is little difference in capacity fade upon cycling between the systems cycled to 1.0 V and 3.0 V, this explanation can be ruled out.

Instead, we attribute the downshift to the formation of envelopes of Li_2S around the Li-Pb alloy particles that are resistive to Li-ion transport.[15,16] These are in sharp contrast to the Li-ion conducting Li_2Te envelopes that form around the Li-Pb alloy particles in PbTe electrodes.[17] Li_2Te has been computationally predicted to be Li-ion conducting,[18] whereas Li_2S is Li-ion insulating. In the Li_2S-free system, dissolved polysulfide species may contaminate the electrolyte or damage the lithium counter electrode,[13] leading to the more rapid negative shift of the 0.4 – 0.5 V reduction peak and reduced cycling performance.

An alternate explanation for the downshift is that the Li_2S helps to retard particle sintering, a problem which is common in low melting point materials such as tin[19] and lead. These materials are particularly susceptible to sintering during cycling, and the Li_2S

may serve as a physical barrier to prevent particle agglomeration. The lack of Li_2S to help prevent sintering in the system cycled to 3.0 V could explain its more rapid peak downshift.

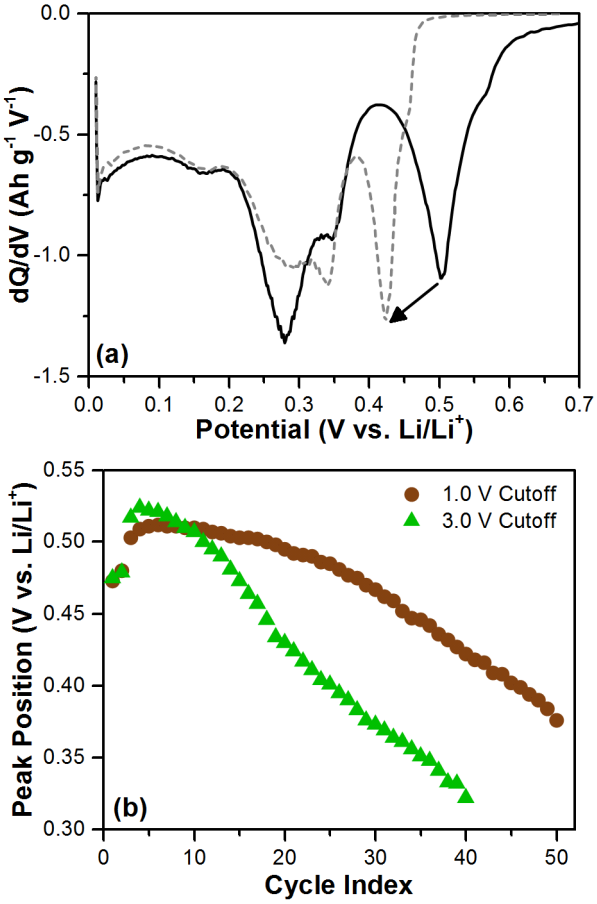

Figure 6.5. (a) Differential capacity profiles for the reduction reaction showing the shift of the 0.4 – 0.5 V reduction peak upon cycling. (b) Position of the first reduction peak's potential as a function of cycle index.

Figure 6.6 shows the accelerated loss of capacity as the C-rate is increased after a single C/20 conditioning cycle (not shown). The electrodes were sequentially cycled ten times each at rates of C/10, C/5, C/2, 1 C, 2 C, 1 C, and C/5. Capacity loss was observed for both the 1.0 V cutoff and the 3.0 V cutoff. For cycling to 1.0 V, the capacities were

469, 453, 395, 294, and 190 mAh g^{-1} after 10 cycles at C/10, C/5, C/2, 1 C, and 2 C, respectively. For cycling to 3.0 V, the capacities were 461, 427, 343, 248, and 159 mAh g^{-1}. Upon returning to the slower C/5 rate, the electrode cycled to 1.0 V recovered more of its initial capacity than that cycled to 3.0 V.

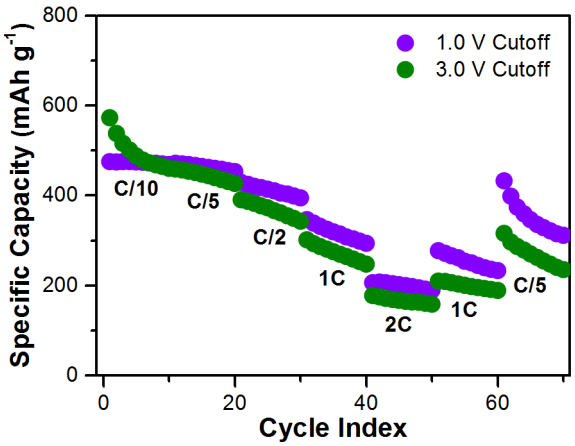

Figure 6.6. Discharge capacity versus cycle index in two potential ranges at varying C-rates.

REFERENCES

(1) Sanusi, A.; Yahya, M. Z. A.; Navaratnam, S.; Basirun, W. J.; Alias, Y.; Mohamed, N. S.; Arof, A. K. Sulphide Based Anode Material for Lithium Rechargeable Battery. *Ionics (Kiel).* **2003**, *9* (3-4), 253–257.

(2) Abel, P. R.; Klavetter, K. C.; Jarvis, K.; Heller, A.; Mullins, C. B. Sub-Stoichiometric Germanium Sulfide Thin-Films as a High-Rate Lithium Storage Material. *J. Mater. Chem. A* **2014**, *2*, 19011–19018.

(3) Cho, Y. J.; Im, H. S.; Kim, H. S.; Myung, Y.; Back, S. H.; Lim, Y. R.; Jung, C. S.; Jang, D. M.; Park, J.; Cha, E. H.; Cho, W. Il; Shojaei, F.; Kang, H. S. Tetragonal Phase Germanium Nanocrystals in Lithium Ion Batteries. *ACS Nano* **2013**, *7* (10), 9075–9084.

(4) Im, H. S.; Cho, Y. J.; Lim, Y. R.; Jung, C. S.; Jang, D. M.; Park, J.; Shojaei, F.; Kang, H. S. Phase Evolution of Tin Nanocrystals in Lithium Ion Batteries. *ACS Nano* **2013**, *7* (12), 11103–11111.

(5) Zhang, W.; Zhang, L.; Cheng, Y.; Hui, Z.; Zhang, X. Synthesis of Nanocrystalline Lead Chalcogenides PbE (E = S , Se , or Te) from Alkaline Aqueous Solutions. *Mater. Res. Bull.* **2000**, *35*, 2009–2015.

(6) Gong, L.; Nguyen, M. H. T.; Oh, E.-S. High Polar Polyacrylonitrile as a Potential Binder for Negative Electrodes in Lithium Ion Batteries. *Electrochem. commun.* **2013**, *29*, 45–47.

(7) Wood, S. M.; Pham, C. H.; Heller, A.; Mullins, C. B. Stages in the Dynamic Electrochemical Lithiation of Lead. *J. Electrochem. Soc.* **2016**, *163* (6), A1027–A1029.

(8) Yu, D. Y. W.; Prikhodchenko, P. V; Mason, C. W.; Batabyal, S. K.; Gun, J.; Sladkevich, S.; Medvedev, A. G.; Lev, O. High-Capacity Antimony Sulphide

Nanoparticle-Decorated Graphene Composite as Anode for Sodium-Ion Batteries. *Nat. Commun.* **2013**, *4* (2922), 1–7.

(9) He, M.; Yuan, L.; Zhang, W.; Hu, X.; Huang, Y. Enhanced Cyclability for Sulfur Cathode Achieved by a Water-Soluble Binder. *J. Phys. Chem. C* **2011**, *115*, 15703–15709.

(10) Zheng, G.; Yang, Y.; Cha, J. J.; Hong, S. S.; Cui, Y. Hollow Carbon Nanofiber-Encapsulated Sulfur Cathodes for High Specific Capacity Rechargeable Lithium Batteries. *Nano Lett.* **2011**, *11* (10), 4462–4467.

(11) Yu, D. Y. W.; Hoster, H. E.; Batabyal, S. K. Bulk Antimony Sulfide with Excellent Cycle Stability as next-Generation Anode for Lithium-Ion Batteries. *Sci. Rep.* **2014**, *4* (4562), 1–6.

(12) Jayaprakash, N.; Shen, J.; Moganty, S. S.; Corona, a.; Archer, L. a. Porous Hollow Carbon@Sulfur Composites for High-Power Lithium-Sulfur Batteries. *Angew. Chemie* **2011**, *123* (26), 6026–6030.

(13) Chung, J.-S.; Sohn, H.-J. Electrochemical Behaviors of CuS as a Cathode Material for Lithium Secondary Batteries. *J. Power Sources* **2002**, *108*, 226–231.

(14) Profatilova, I. A.; Stock, C.; Schmitz, A.; Passerini, S.; Winter, M. Enhanced Thermal Stability of a Lithiated Nano-Silicon Electrode by Fluoroethylene Carbonate and Vinylene Carbonate. *J. Power Sources* **2013**, *222*, 140–149.

(15) Yang, L.; Hua-Qing, X.; Jiang-Ping, T. SnS with Various Morphologies and Sizes as Anode Material for Lithium Ion Batteries. *Acta Physico-Chimica Sin.* **2009**, *25* (2), 365–370.

(16) Li, Y.; Tu, J. P.; Wu, H. M.; Yuan, Y. F.; Shi, D. Q. Mechanochemical Synthesis and Electrochemical Properties of Nanosized SnS as an Anode Material for Lithium Ion Batteries. *Mater. Sci. Eng. B* **2006**, *128* (1-3), 75–79.

(17) Wood, S. M.; Klavetter, K. C.; Heller, A.; Mullins, C. B. Fast Lithium Transport in PbTe for Lithium-Ion Battery Anodes. *J. Mater. Chem. A* **2014**, *2* (20), 7238–7243.

(18) Kishida, I.; Koyama, Y.; Kuwabara, A.; Yamamoto, T.; Oba, F.; Tanaka, I. First-Principles Calculations of Migration Energy of Lithium Ions in Halides and Chalcogenides. *J. Phys. Chem. B* **2006**, *110* (16), 8258–8262.

(19) Kim, D. G.; Kim, H.; Sohn, H. J.; Kang, T. Nanosized Sn-Cu-B Alloy Anode Prepared by Chemical Reduction for Secondary Lithium Batteries. *J. Power Sources* **2002**, *104*, 221–225.

Chapter 7:
PbSe[§]

INTRODUCTION

Addition of Se has been shown to greatly improve the performance of both Ge[1,2] and Sn[3,4] materials, allowing for superfast charge/discharge rates while maintaining high capacities by acting as a superionic conductor once reduced to Li_2Se. In this chapter, Se was added to Pb to form PbSe and see whether or not similar benefits were conferred.

Although the PbSe electrode did not cycle either stably or rapidly, its capacity in the first 25 cycles greatly exceeded the theoretical coulometric capacity of PbSe. The excess capacity was added by an electrolyte-derived polymer gel film (PGF) that was electroreduced and electrooxidized during cycling. Such a film, contributing up to 150 mAh g^{-1}, was first reported for a CoO electrode by Laruelle et al. who attributed its formation to the catalysis of solvent polymerization.[5] Li et al. found that on an Fe_2O_3 electrode, the solvent-derived PGF contributed 100 mAh g^{-1},[6] and on MnO it contributed 480 mAh g^{-1}.[7] When Xu et al. prevented a C/Sn composite from forming the solvent-derived PGF, its capacity dropped by 620 mAh g^{-1}.[8] Seng et al. showed that the capacity of NiO can increase by as much as 680 mAh g^{-1} with a PGF.[9] In this chapter, an electroactive PGF also formed on the PbSe electrode, adding as much as 300 mAh g^{-1} to its nominal capacity.

[§] This work was previously published: Sean M. Wood, Codey H. Pham, Adam Heller, C. Buddie Mullins, "Formation of an Electroactive Polymer Gel Film upon Lithiation and Delithiation of PbSe", *J. Electrochem. Soc.*, 163 (2016) A1666-A1671. The author of the dissertation was responsible for development of experiments, electrochemical measurements, *ex situ* XRD measurements and XRD calculations, *ex situ* SEM measurements, and data analysis.

EXPERIMENTAL INFORMATION

Synthesis and Characterization

All chemicals were purchased from Sigma-Aldrich, unless otherwise noted, and used as received. Following a procedure by Zhang et al.,[10] PbSe nanoparticles were prepared by adding 5 mmol of elemental selenium to 100 mL of stirred deionized (DI) water. To this solution 1.12 mol of NaOH was added followed by heating to ~80 °C to dissolve the Se. The solution was deep burgundy colored, nearly black. A second solution was prepared by dissolving 5.2 mmol of $Pb(Ac)_2 \cdot 3H_2O$ in 10 mL of DI water. After the Se solution cooled to room temperature, the Pb solution was added all at once. The resultant black PbSe particles were collected by centrifugation and washed twice with DI water and once with acetone then dried under vacuum at 70 °C overnight.

Scanning Electron Microscopy (SEM) micrographs were obtained using a Hitachi S-5500 electron microscope. Powder X-Ray Diffraction (XRD) spectra were obtained with a Spider R-axis diffractometer with a Cu Kα radiation source at 40 kV and 40 mA. *Ex situ* measurements were performed by extracting electrodes after cycling and rinsing lightly in diethyl carbonate (DEC). *Ex situ* XRD measurements were performed on a Rigaku MiniFlex 600 diffractometer with a Cu Kα radiation source at 40 kV and 15 mA. The lattice constants in Table 7.1 were calculated using Bragg's Law,

$$\lambda = 2 d \sin(\theta),$$

where λ is the wavelength of the incident X-ray source (1.5406 Å for Cu Kα radiation), d is the interlayer atomic spacing, and θ is the scattering angle. Using the peak positions from the XRD spectra, d was solved for. Knowing d, the lattice constant, a, could be calculated using the d-spacing equation for a cubic crystal,

$$a^2 = d^2 (h^2 + k^2 + l^2),$$

where h, k, and l are the Miller indices for the peaks found in the XRD spectra.

Electrochemical Measurements

An aqueous slurry of PbSe nanoparticles (60 wt %), sodium carboxymethylcellulose (90 kDa, 20 wt %) binder, and Super P Li conductive carbon (Timcal, 20 wt %) was coated onto copper foil and dried in a vacuum oven at 120 °C for at least 6 h. The coated foil was punched into disks that formed the working electrodes of CR 2032 coin-type cells. Each electrode had an average PbSe mass loading of about 1.1 mg cm^{-2}. The cells were assembled in an argon-filled glovebox with Li foil counter and reference electrodes and Celgard 2400 polypropylene membrane separators. A solution of 1M $LiPF_6$ in fluoroethylene carbonate (FEC, Solvay Fluor)/DEC (1:1 w/w) was used as the electrolyte. The use of FEC as a co-solvent rather than as an additive was previously found to greatly enhance cycling performance.[11–13] Cyclic voltammetry and galvanostatic cycling were performed on an Arbin BT 2143 multichannel battery testing system. Electrochemical impedance spectra were collected with a CH Instruments 608D electrochemical analyzer/workstation in the frequency range 100 kHz to 10 mHz with a perturbing voltage amplitude of 5 mV.

RESULTS & DISCUSSION

The XRD spectrum of the synthesized black powder is shown in Figure 7.1a, and its match with the clausthalite reference spectrum (JCPDS # 01-077-0245) confirmed that the material was phase-pure clausthalite PbSe. The sharpness of the XRD peaks indicated the crystallites were not particularly small, consistent with the SEM micrograph of Figure 6.1b showing non-spherical 50 – 100 nm diameter particles with a rough texture.

Cyclic voltammograms (CVs) in the 0.01 – 3.0 V and 0.01 – 2.45 V vs. Li/Li^+ potential ranges (Figure 7.2a and Figure 7.2b, respectively) show persistent, reversible redox wave pairs at 0.44/0.67 V and 0.20/0.58 V vs. Li/Li^+. Above 1.0 V vs. Li/Li^+, there were wave pairs at 1.3/1.8 V and 1.9/2.3 V. In the first cycle, the reduction wave at 1.9 V

was shifted to 1.65 V, indicative of an activation step that is characteristic of chalcogenide materials.[14–18] The activation step is a result of stress relaxation within the particles caused by their expansion-induced deformation during the first cycle. Once the initial stresses within the particles are dissipated, subsequent lithiation becomes more facile, which pushes the reduction peak to the higher potential seen in the second cycle.[19,20]

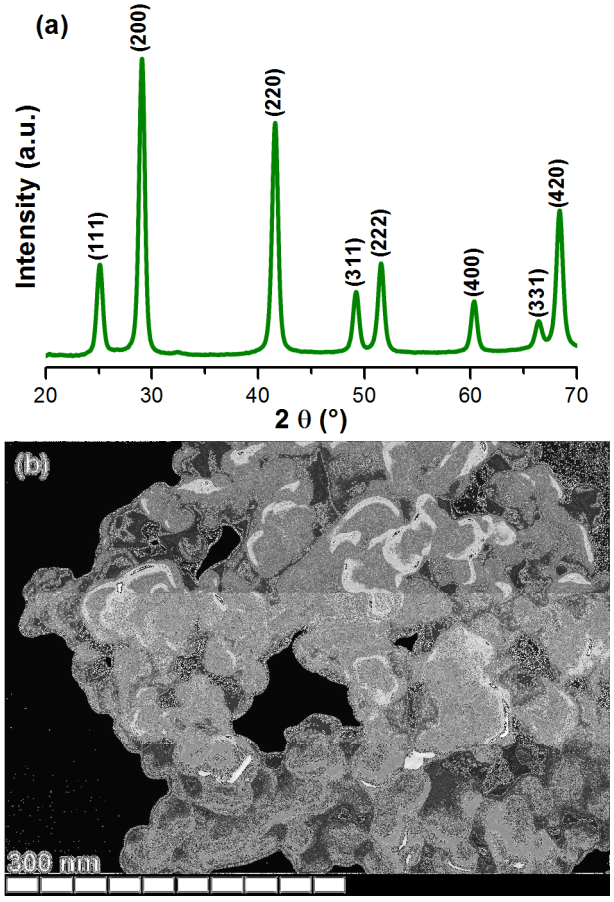

Figure 7.1. (a) XRD pattern of the PbSe nanoparticles. (b) SEM micrograph of the PbSe nanoparticles.

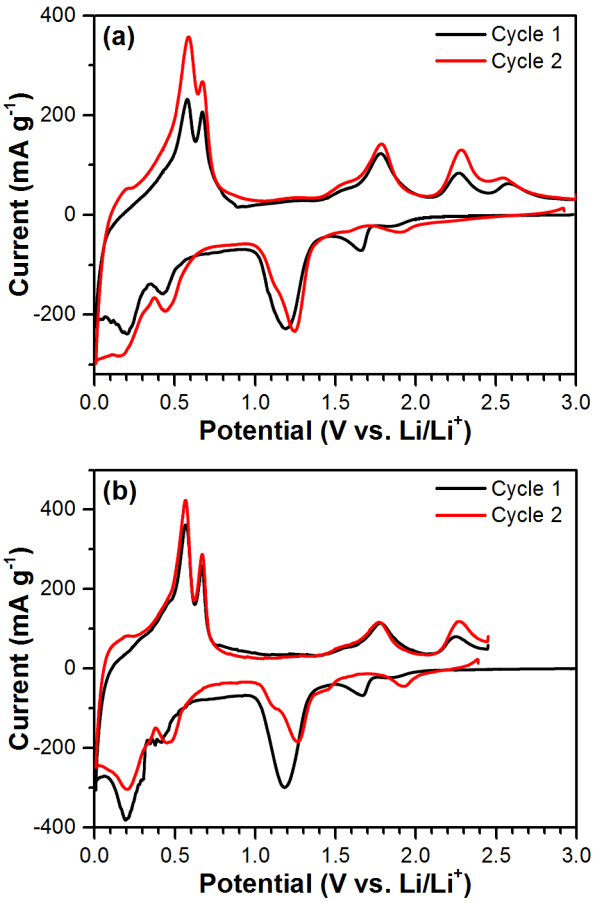

Figure 7.2. The two initial voltammetric cycles of the PbSe electrode. Scan rate 0.1 mV s^{-1}. (a) 0.01 – 3.0 V vs. Li/Li^+ and (b) 0.01 – 2.45 V vs. Li/Li^+.

According to Xie et al., the redox couple at 1.9/2.3 V seen in Figure 7.2 corresponds to the breakdown and re-formation of PbSe,[16] possibly involving the reversible insertion of one Li atom in the PbSe lattice (Equation 7.1) analogous to a similar insertion in the PbS lattice.[21–23] The redox wave at 1.3/1.8 V corresponded accordingly to the reduction of Li(PbSe) to Pb and Li_2Se (Equation 7.2). These reaction steps were confirmed by comparison of the *ex situ* XRD spectra of electrodes lithiated to 1.4 V and 1.0 V (Figure 7.3b and Figure 7.3c, respectively) with that of a pristine electrode (Figure 7.3a). The spectrum of the pristine electrode showed only peaks of

PbSe and Cu; upon lithiation to 1.4 V, the PbSe peaks had shifted to the lower 2θ values shown in Table 7.1. Although uniform shifting of the 2θ values could derive from an artifact introduced by the height of the sample in the holder, such errors were avoided by aligning the Cu (1 1 1) internal reference peak to 2θ = 43.342° (JCPDS Card #01-070-3039).[24] The non-uniform shifting of the PbSe peaks to lower values indicates therefore a true lattice expansion upon insertion of Li atoms in the PbSe lattice without altering the phase, i.e. the crystalline structure. Lattice constants for each of the peak positions in Table 7.1 were calculated and are also shown in Table 7.1. The pristine electrode had a calculated lattice constant of 6.12 Å, which agreed well with the reported value.[25] Upon lithiation to 1.4 V the lattice constant was calculated as 6.13 Å, and at 1.0 V it increased to 6.14 Å, indicating that the lattice expansion did in fact take place.

Upon lithiation to 1.0 V (Figure 7.3c), the expanded PbSe lattice remained, but Pb and Li_2Se peaks appeared (as in Equation 7.2). Magnified portions of Figure 7.3a and Figure 7.3c are provided in Figure 7.3d and Figure 7.3e. Li_2Se formation was confirmed by the 25.6° to 26.0° shoulder. Below 1.0 V, the 0.45/0.65 V and 0.20/0.55 V waves corresponded to the formation of the known Li-Pb alloys with $Li_{3.5}Pb$ being the end member of the series (as in Equation 7.3).[26] An XRD spectrum of an electrode fully lithiated to 0.01 V (Figure 7.3d) showed the presence of Li_2Se, reaffirming its presence from Figure 7.3c. The PbSe peaks entirely disappeared, replaced by Pb and Li_8Pb_3. The fully-lithiated reaction product, Li_7Pb_2, was not seen perhaps due to the small size of the particles making it invisible to X-rays or due to incomplete lithiation at the relatively fast 1C charge rate.

Equation 7.1: $PbSe + Li^+ + e^- \leftrightarrow Li(PbSe)$

Equation 7.2: $Li(PbSe) + Li^+ + e^- \leftrightarrow Pb + Li_2Se$

Equation 7.3: $Pb + 3.5\ Li^+ + 3.5\ e^- + Li_2Se \leftrightarrow Li_{3.5}Pb + Li_2Se$

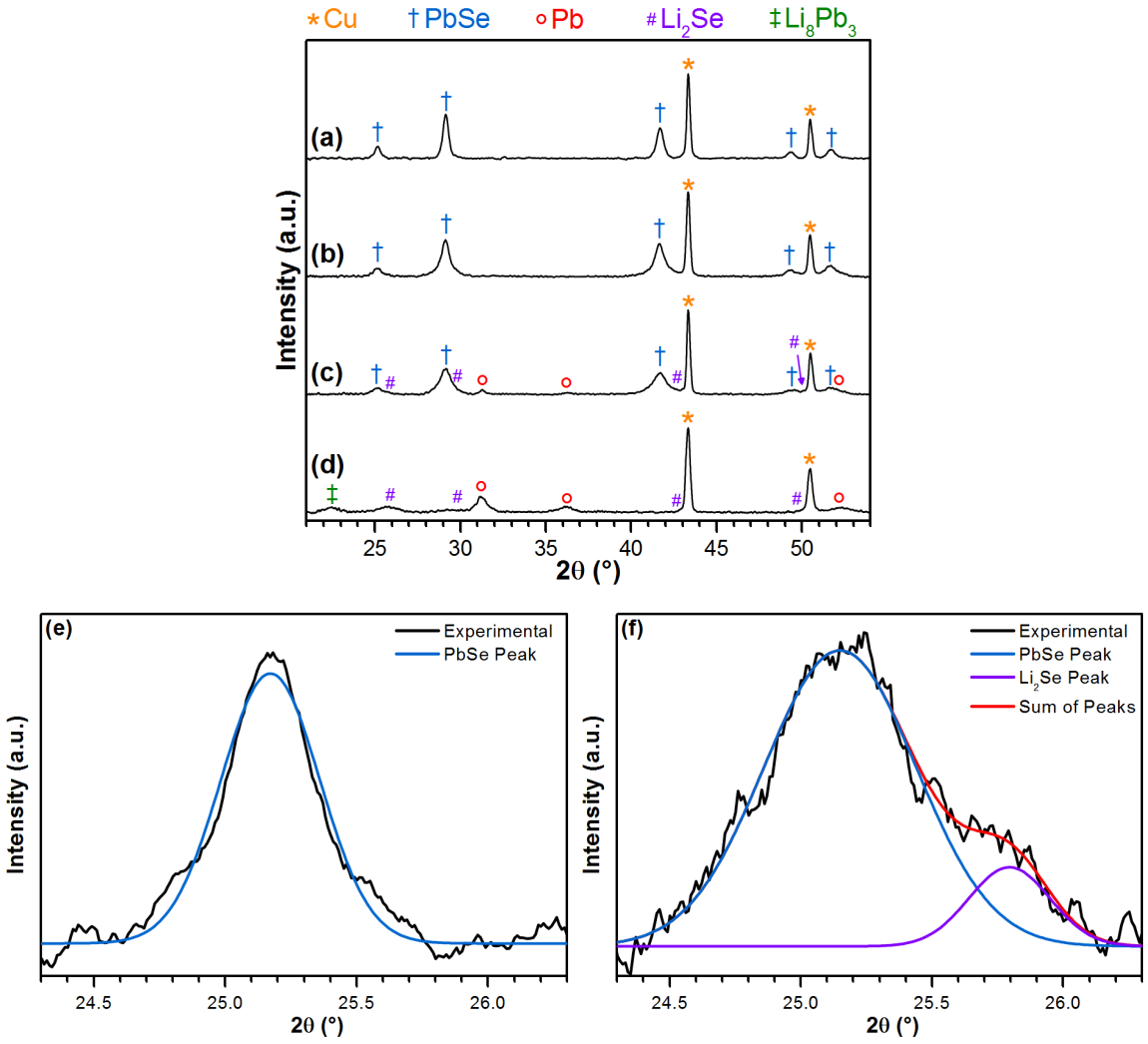

Figure 7.3. XRD spectra of (a) a pristine PbSe electrode, (b) a PbSe electrode lithiated to 1.4 V vs. Li/Li^+, (c) a PbSe electrode lithiated to 1.0 V vs. Li/Li^+, and (d) a PbSe electrode lithiated to 0.01 V vs. Li/Li^+, with zoomed-in portions of the (1 1 1) peak region from (a) and (c) shown in (e) and (f), respectively.

Table 7.1. 2θ peak positions and calculated lattice constants for selected PbSe peaks from the XRD spectra of Figure 7.3.

Peak:	**(1 1 1)**		**(2 0 0)**		**(2 2 0)**	
	2θ	**a (Å)**	**2θ**	**a (Å)**	**2θ**	**a (Å)**
Pristine Electrode	25.18°	6.121	29.16°	6.120	41.71°	6.120
Lithiated to 1.0 V	25.14°	6.131	29.11°	6.130	41.63°	6.131
Lithiated to 1.4 V	25.10°	6.140	29.06°	6.141	41.57°	6.140

The presence and size of the reduction waves near 1.3 V and below 0.2 V directly depended on the oxidation wave above 2.5 V. In the second cycle, a wave below 0.2 V was absent and a wave at 1.3 V was smaller when the greater than 2.5 V oxidation wave was excluded by restricting the cutoff potential to 2.45 V. These waves are attributed to solvent electroreduction resulting in the formation of a polymer gel film (PGF) to be discussed below. The major reduction wave at 1.3 V (Figure 7.2a) is a superposition of the PGF formation wave and the Li(PbSe) lithiation wave (per Equation 7.2).

Upon galvanostatic cycling in the potential range 0.01 – 3.0 V vs. Li/Li^+ for one C/20 rate cycle (not shown) followed by 100 cycles at a 1C rate (Figure 7.4a), the capacity increased in the first 25 cycles from 592 mAh g^{-1} to 695 mAh g^{-1} then decreased for the following 75 cycles, ending at 550 mAh g^{-1} on the 100^{th} cycle. When cycled once at C/20 (not shown) then sequentially for ten cycles each at C/10, C/5, C/2, 1C, 2C, 1C, and C/5 (Figure 7.4b), the capacity increased through the first ten C/10 cycles, was stable at C/5, and faded at all faster rates. The respective tenth cycle capacities were 813, 767, 597, 429, and 255 mAh g^{-1}. Upon returning to 1C and C/5 rates, the initial capacities were not recovered.

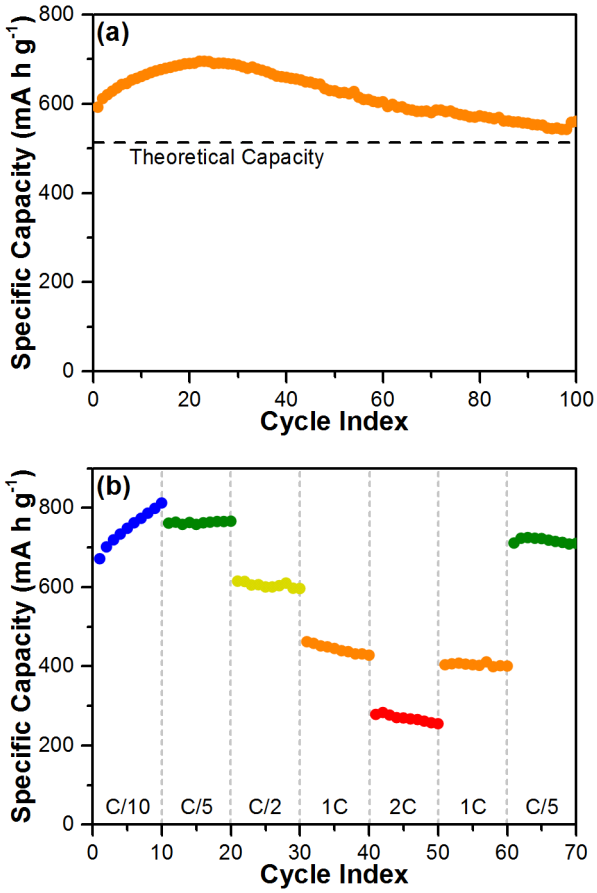

Figure 7.4. Discharge capacity versus cycle index in the potential range 0.01 – 3.0 V vs. Li/Li^+ (a) at a rate of 1C following one C/20 conditioning cycle (not shown) and (b) at varying C-rates following one C/20 conditioning cycle (not shown).

The theoretical capacity for the full lithiation of PbSe by 5.5 Li atoms (as in Equation 7.1 through Equation 7.3) is 515 mAh g^{-1}. Throughout the 100 cycles the capacity was, however, higher (dashed line in Figure 7.4a) because of capacity gain in the first 25 cycles. Potential-capacity profiles of cycles 2 and 24 are shown in Figure 7.5a and of cycles 24 and 100 in Figure 7.5d. Subtraction of the capacities at particular potentials provided the difference profiles shown in Figure 7.5b and Figure 7.5e; their derivatives are shown in Figure 7.5c and Figure 7.5f, respectively. Full voltage-capacity profiles and differential capacity profiles are available in Figure 7.6 for the interested

reader. In Figure 7.5c and Figure 7.5f, areas of capacity gain are positive and areas of capacity fade are negative. The capacity gain of the first 25 cycles was a combination of reduction in the potential ranges 0.01 – 0.2 V and 1.3 – 1.6 V and oxidation in the range 2.3 – 3.0 V. Electroactive PGFs have been known to reversibly form from kinetically activated electrolyte degradation at low potentials during reduction then disappear upon reoxidation at higher potentials above 2.5 V vs. Li/Li^+.[5–9,18,27–29] These PGFs have been known to form from both the standard EC/DMC electrolyte and also FEC-containing electrolytes, such as the one used in this work. The negative regions around the 0.5 – 0.7 V range (during oxidation) and the 1.1 – 1.3 V range (during reduction) were introduced by amorphization and do not indicate an actual decrease in capacity.

In cycles 26 – 100 (Figure 7.5f), the PGF formation/removal still added to the capacity but now the intrinsic capacity of PbSe lithiation/delithiation faded. Major capacity fade was seen in the 0.2 – 2.2 V region caused by the severe volume changes experienced during lithiation and delithiation, which resulted in particles that were fractured, electrically isolated, and unavailable for cycling. The beginnings of this destruction can be found in the XRD spectra of Figure 7.7 which compares a pristine electrode (Figure 7.7a) and an electrode after 20 cycles (Figure 7.7b). The pristine electrode showed only peaks for PbSe and Cu, whereas the cycled electrode also showed peaks for Li_8Pb_3 and Pb. These new peaks were from the remnants of fractured, electrically-isolated particles, no longer available for lithiation or delithiation. Additionally, the cycled electrode showed smaller, broader PbSe peaks, with the full width at half maximum for the (2 0 0) peak increasing from 0.38° to 1.11° after twenty cycles, signaling particle amorphization.

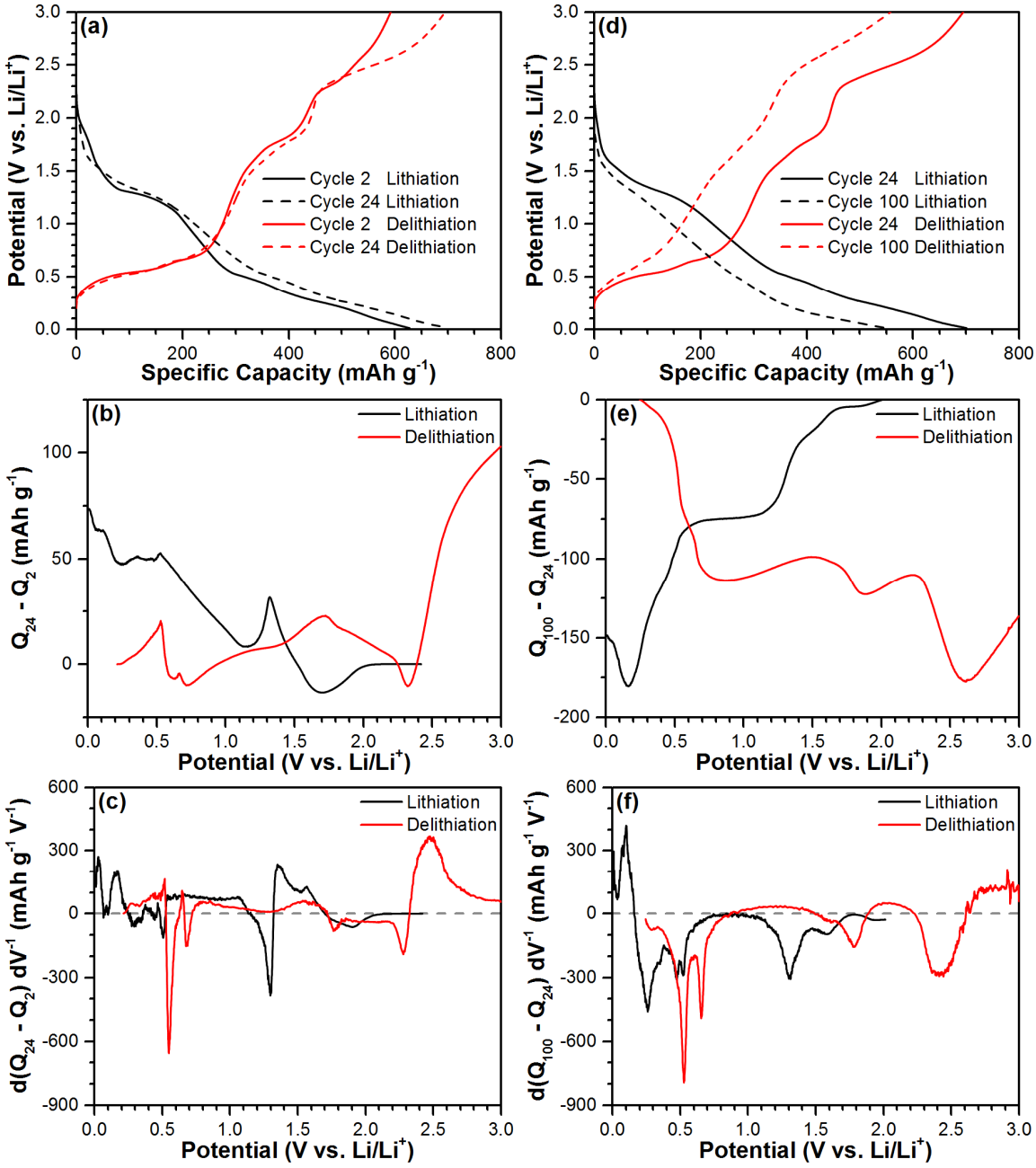

Figure 7.5. Potential vs. capacity profiles for the (a) 2nd and 24th cycles and (d) 24th and 100th cycles. The differences of the capacities between the (b) 2nd and 24th cycles and (e) 24th and 100th cycles. Potential dependence of the derivative of the capacity-difference between the (c) 24th and 2nd cycles and (f) 100th and 24th cycles.

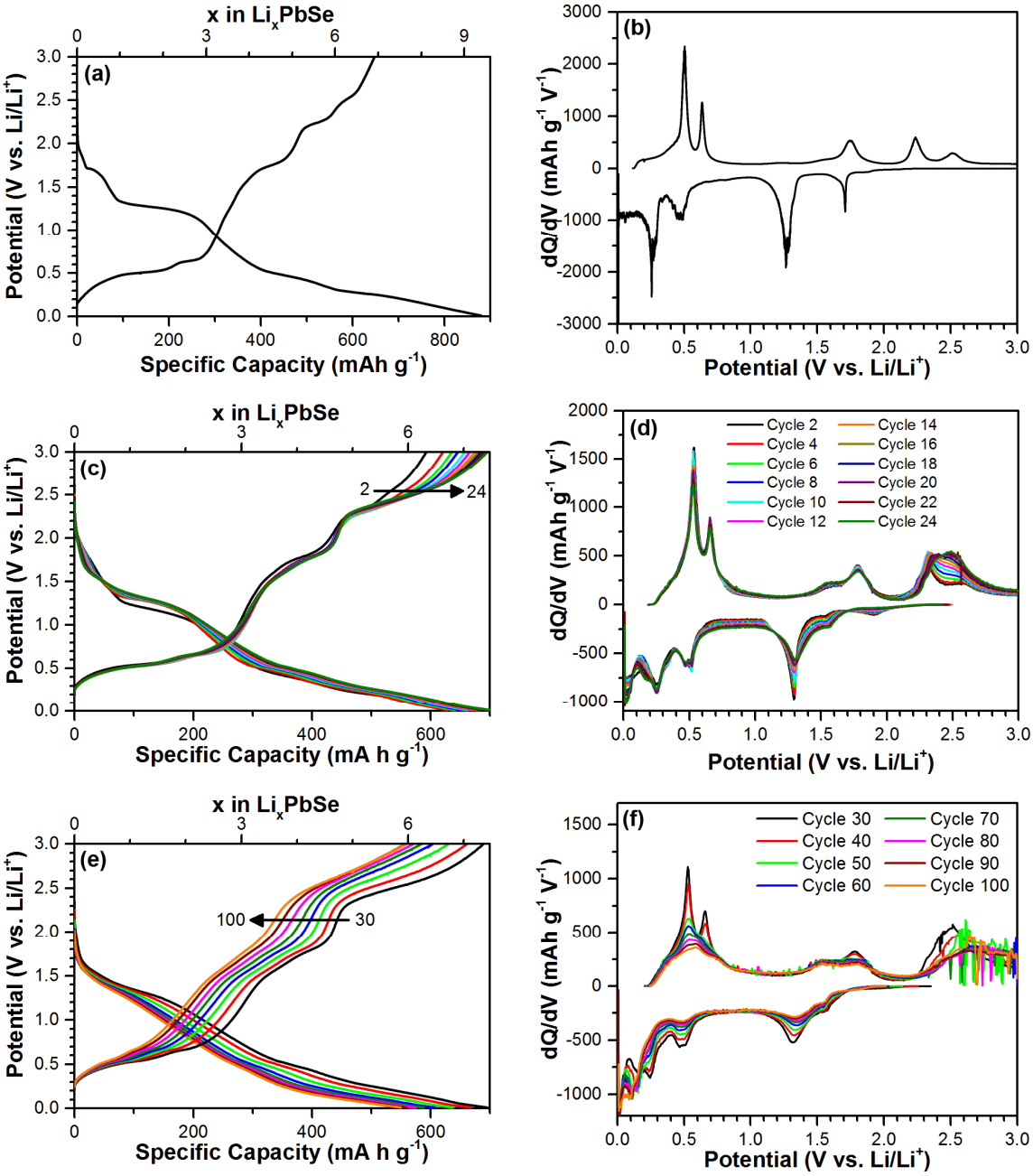

Figure 7.6. (a, c, e) Capacity-voltage profiles and (b, d, f) differential capacity profiles for PbSe electrodes in the 0.01 – 3.0 V vs. Li/Li$^+$ potential range for (a, b) cycle 1, (c, d) cycles 2 – 24, and (e, f) cycles 30 – 100.

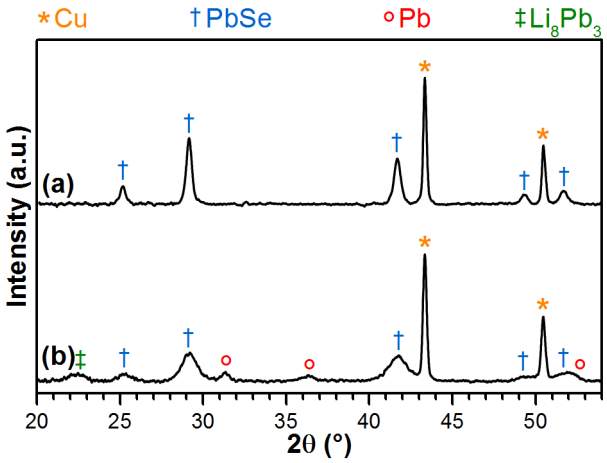

Figure 7.7. XRD spectra of (a) a pristine PbSe electrode and (b) a PbSe electrode after cycling (one C/20 cycle and twenty 1C cycles) and fully delithiated to 3.0 V.

During the C-rate test in Figure 7.4b, the capacity increased through the first ten C/10 cycles and ended 300 mAh g^{-1} above the theoretical capacity; the excess capacity at 1C was much less. Thus, the formation of the capacity-adding PGF is slow, most likely because of a rate-determining chemical step which is avoided at higher rates. The capacity at 1C in Figure 7.4b was much lower than it was after an equivalent number of cycles in Figure 7.4a. The increased severity of the PGF formation at slower rates earlier in cycling harmed the cycling performance compared to cycling at a consistently faster C-rate.

Figure 7.8a shows the equivalent circuit to which a model of electrochemical impedance spectra (EIS) was fit. Nyquist plots of EIS data for a single cell that had been cycled 20 times and then lithiated to either 0.1 V or 0.01 V are shown in Figure 7.8b, while the data for a similar cell delithiated to either 2.5 V or 3.0 V are shown in Figure 7.8c. In the equivalent circuit, R_e, R_{SEI}, and R_{ct} are the resistances due to the electrolyte, the solid electrolyte interphase (SEI) layer, and charge-transfer, respectively. CPE_{SEI} and CPE_{ct} are the capacitances that relate to the SEI and charge-transfer, respectively. Z_w is

the Warburg impedance factor which relates to mass transfer of lithium through the electrode material.[6,9] Values for the resistances that were used to fit the model to the data are given in Table 7.2. Upon lithiation from 0.1 V to 0.01 V, a region in which the PGF is formed by electroreduction, R_{SEI} increased from 4.0 Ω to 10.5 Ω and R_{ct} increased from 80.6 Ω to 125.4 Ω. The increases were consistent with the formation of an electroactive PGF that became more resistive and impeded charge transfer. Upon delithiation from 2.5 V to 3.0 V, the region in which the PGF is removed by electrooxidation, R_{SEI} decreased from 6.3 Ω to 1.2 Ω and R_{ct} decreased from 39.3 Ω to 24.3 Ω. These decreases indicated the removal of more-resistive PGF from the surface of the electrode.

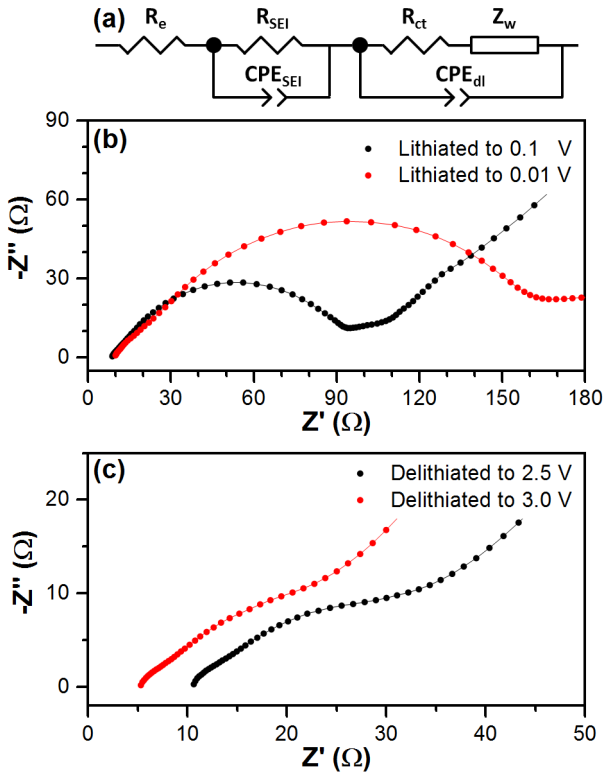

Figure 7.8. (a) Equivalent circuit to which a model for the electrochemical impedance spectroscopy data was fit. Nyquist plots derived from EIS spectra of electrodes after cycling (one C/20 cycle and twenty 1C cycles) followed by (b) lithiation to either 0.1 V or 0.01 V or (c) delithiation to either 2.5 V or 3.0 V.

Table 7.2. Values for the resistances fit to the equivalent circuit model in Figure 7.8.

	R_e (Ω)	R_{SEI} (Ω)	R_{ct} (Ω)
Lithiated to 0.1 V	8.9	4.0	80.6
Lithiated to 0.01 V	10.6	10.5	125.4
Delithiated to 2.5 V	10.8	6.3	39.3
Delithiated to 3.0 V	5.5	1.2	24.3

The PGF can be seen in the SEM of Figure 7.9. The pristine electrode in Figure 7.9a had many large voids between the PbSe and Super P Li particles. After 20 complete cycles followed by delithiation up to 2.5 V (Figure 7.9b), a thick film encased the particles, leaving almost no voids. Upon further oxidation to 3.0 V (Figure 7.9c), the PGF was stripped. The PbSe and Super P Li particles were then encased only in a thin SEI layer, making the particles more distinguishable.

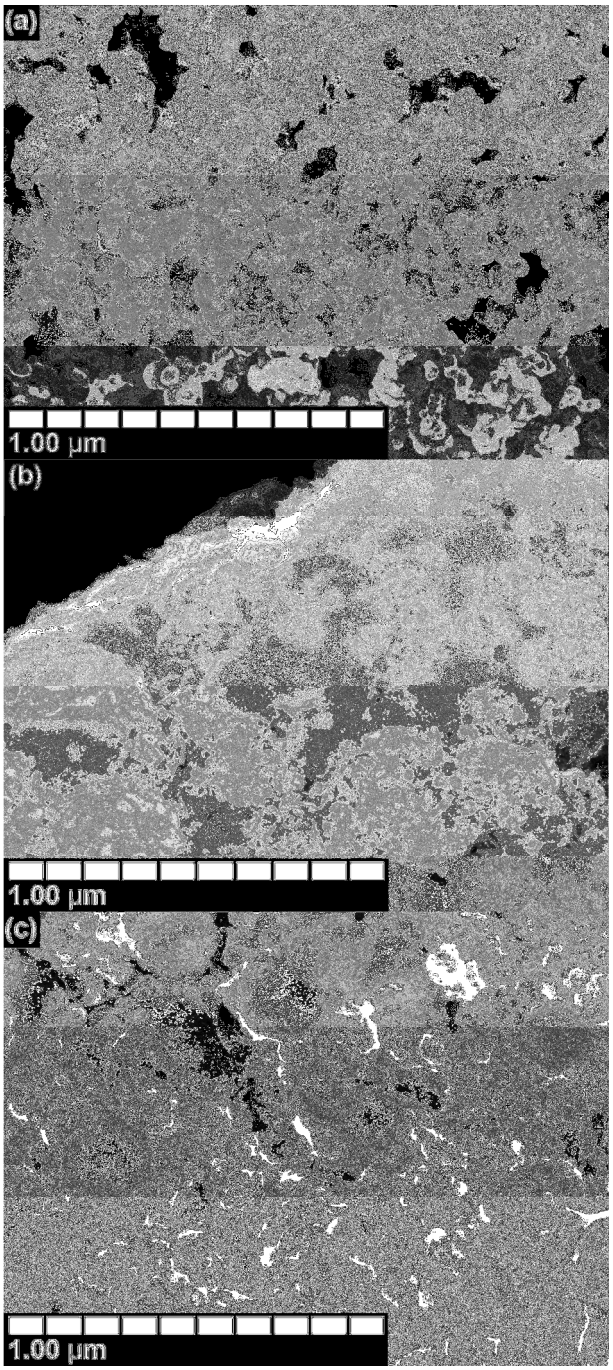

Figure 7.9. SEM micrographs of (a) a pristine PbSe electrode, (b) a PbSe electrode after cycling (one C/20 cycle and twenty 1C cycles) and subsequent delithiation to 2.5 V, and (c) after cycling (one C/20 cycle and twenty 1C cycles) and subsequent delithiation to 3.0 V.

REFERENCES

(1) Abel, P. R.; Klavetter, K. C.; Heller, A.; Mullins, C. B. Thin Nanocolumnar Ge0.9Se0.1 Films Are Rapidly Lithiated/Delithiated. *J. Phys. Chem. C* **2014**, *118*, 17407–17412.

(2) Klavetter, K. C.; Pedro de Souza, J.; Heller, A.; Mullins, C. B. High Tap Density Microparticles of Selenium-Doped Germanium as a High Efficiency, Stable Cycling Lithium-Ion Battery Anode Material. *J. Mater. Chem. A* **2015**, *3* (11), 5829–5834.

(3) Wang, X.; Liu, B.; Xiang, Q.; Wang, Q.; Hou, X.; Chen, D.; Shen, G. Spray-Painted Binder-Free SnSe Electrodes for High-Performance Energy-Storage Devices. *ChemSusChem* **2014**, *7* (1), 308–313.

(4) Dang, H. X.; Klavetter, K. C.; Meyerson, M. L.; Heller, A.; Mullins, C. B. Tin Microparticles for a Lithium Ion Battery Anode with Enhanced Cycling Stability and Efficiency Derived from Se-Doping. *J. Mater. Chem. A* **2015**, *3* (25), 13500–13506.

(5) Laruelle, S.; Grugeon, S.; Poizot, P.; Dollé, M.; Dupont, L.; Tarascon, J.-M. On the Origin of the Extra Electrochemical Capacity Displayed by MO/Li Cells at Low Potential. *J. Electrochem. Soc.* **2002**, *149* (5), A627–A634.

(6) Li, X.; Qiao, L.; Li, D.; Wang, X.; Xie, W.; He, D. Three-Dimensional Network Structured α-Fe2O3 Made from a Stainless Steel Plate as a High-Performance Electrode for Lithium Ion Batteries. *J. Mater. Chem. A* **2013**, *1* (21), 6400–6406.

(7) Li, X.; Shang, X.; Li, D.; Yue, H.; Wang, S.; Qiao, L.; He, D. Facile Synthesis of Porous MnO Microspheres for High-Performance Lithium-Ion Batteries. *Part. Part. Syst. Charact.* **2014**, *31* (9), 1001–1007.

(8) Xu, Y.; Guo, J.; Wang, C. Sponge-like Porous Carbon/tin Composite Anode

Materials for Lithium Ion Batteries. *J. Mater. Chem.* **2012**, *22*, 9562–9567.

(9) Seng, K. H.; Li, L.; Chen, D. P.; Chen, Z. X.; Wang, X. L.; Liu, H. K.; Guo, Z. P. The Effects of FEC (Fluoroethylene Carbonate) Electrolyte Additive on the Lithium Storage Properties of NiO (Nickel Oxide) Nanocuboids. *Energy* **2013**, *58*, 707–713.

(10) Zhang, W.; Zhang, L.; Cheng, Y.; Hui, Z.; Zhang, X. Synthesis of Nanocrystalline Lead Chalcogenides PbE (E = S , Se , or Te) from Alkaline Aqueous Solutions. *Mater. Res. Bull.* **2000**, *35*, 2009–2015.

(11) Etacheri, V.; Haik, O.; Goffer, Y.; Roberts, G. A.; Stefan, I. C.; Fasching, R.; Aurbach, D. Effect of Fluoroethylene Carbonate (FEC) on the Performance and Surface Chemistry of Si-Nanowire Li-Ion Battery Anodes. *Langmuir* **2012**, *28* (1), 965–976.

(12) Lin, Y.-M.; Klavetter, K. C.; Abel, P. R.; Davy, N. C.; Snider, J. L.; Heller, A.; Mullins, C. B. High Performance Silicon Nanoparticle Anode in Fluoroethylene Carbonate-Based Electrolyte for Li-Ion Batteries. *Chem. Commun.* **2012**, *48* (58), 7268–7270.

(13) Klavetter, K. C.; Wood, S. M.; Lin, Y.-M.; Snider, J. L.; Davy, N. C.; Chockla, A. M.; Romanovicz, D. K.; Korgel, B. a.; Lee, J.-W.; Heller, A.; Mullins, C. B. A High-Rate Germanium-Particle Slurry Cast Li-Ion Anode with High Coulombic Efficiency and Long Cycle Life. *J. Power Sources* **2013**, *238*, 123–136.

(14) Yu, D. Y. W.; Prikhodchenko, P. V; Mason, C. W.; Batabyal, S. K.; Gun, J.; Sladkevich, S.; Medvedev, A. G.; Lev, O. High-Capacity Antimony Sulphide Nanoparticle-Decorated Graphene Composite as Anode for Sodium-Ion Batteries. *Nat. Commun.* **2013**, *4* (2922), 1–7.

(15) Lu, J.; Nan, C.; Li, L.; Peng, Q.; Li, Y. Flexible SnS Nanobelts: Facile Synthesis,

Formation Mechanism and Application in Li-Ion Batteries. *Nano Res.* **2012**, *6* (1), 55–64.

(16) Xie, J.; Tu, F.; Su, Q.; Du, G.; Zhang, S.; Zhu, T.; Cao, G.; Zhao, X. *In situ* TEM Characterization of Single PbSe/reduced-Graphene-Oxide Nanosheet and the Correlation with Its Electrochemical Lithium Storage Performance. *Nano Energy* **2014**, *5*, 122–131.

(17) Wood, S. M.; Powell, E. J.; Heller, A.; Mullins, C. B. Lithiation and Delithiation of Lead Sulfide (PbS). *J. Electrochem. Soc.* **2015**, *162* (7), A1182–A1185.

(18) Han, F.; Li, W.-C.; Li, M.-R.; Lu, A.-H. Fabrication of Superior-Performance SnO2@C Composites for Lithium-Ion Anodes Using Tubular Mesoporous Carbon with Thin Carbon Walls and High Pore Volume. *J. Mater. Chem.* **2012**, *22* (19), 9645–9651.

(19) Luo, C.; Xu, Y.; Zhu, Y.; Liu, Y.; Zheng, S.; Liu, Y.; Langrock, A.; Wang, C. Selenium@Mesoporous Carbon Composite with Superior Lithium and Sodium Storage Capacity. *ACS Nano* **2013**, *7* (9), 8003–8010.

(20) Rui, K.; Wen, Z.; Huang, X.; Lu, Y.; Jin, J.; Shen, C. High-Performance Lithium Storage in an Ultrafine Manganese Fluoride Nanorod Anode with Enhanced Electrochemical Activation Based on Conversion Reaction. *Phys. Chem. Chem. Phys.* **2016**, *18* (5), 3780–3787.

(21) Yong-Fang, L.; Hao-Qing, W. Electrochemical Intercalation Reaction of Lithium into Sulfides of Nonlayer Structure. I. Lithium Intercalation in Lead Sulfide. *Acta Chim. Sin.* **1987**, *45*, 1147–1151.

(22) Lavela, P.; Morales, J.; Sánchez, L.; Tirado, J. L. Novel Layered Chalcogenides as Electrode Materials for Lithium-Ion Batteries. *J. Power Sources* **1997**, *68* (2), 704–707.

(23) Sanusi, A.; Yahya, M. Z. A.; Navaratnam, S.; Basirun, W. J.; Alias, Y.; Mohamed, N. S.; Arof, A. K. Sulphide Based Anode Material for Lithium Rechargeable Battery. *Ionics (Kiel).* **2003**, *9* (3-4), 253–257.

(24) van de Krol, R.; Goossens, A.; Meulenkamp, E. A. *In situ* X-Ray Diffraction of Lithium Intercalation in Nanostructured and Thin Film Anatase TiO2. *J. Electrochem. Soc.* **1999**, *146* (9), 3150–3154.

(25) Madelung, O.; Rössler, U.; Schulz, M. Lead Selenide (PbSe) Crystal Structure, Lattice Parameters, Thermal Expansion. In *Non-Tetrahedrally Bonded Elements and Binary Compounds I*; 1998; pp 1–4.

(26) Wood, S. M.; Pham, C. H.; Heller, A.; Mullins, C. B. Stages in the Dynamic Electrochemical Lithiation of Lead. *J. Electrochem. Soc.* **2016**, *163* (6), A1027–A1029.

(27) Grugeon, S.; Laruelle, S.; Dupont, L.; Tarascon, J. M. An Update on the Reactivity of Nanoparticles Co-Based Compounds towards Li. *Solid State Sci.* **2003**, *5* (6), 895–904.

(28) Ponrouch, A.; Taberna, P. L.; Simon, P.; Palacín, M. R. On the Origin of the Extra Capacity at Low Potential in Materials for Li Batteries Reacting through Conversion Reaction. *Electrochim. Acta* **2012**, *61*, 13–18.

(29) Xu, Y.; Zhu, Y.; Liu, Y.; Wang, C. Electrochemical Performance of Porous Carbon/tin Composite Anodes for Sodium-Ion and Lithium-Ion Batteries. *Adv. Energy Mater.* **2013**, *3* (1), 128–133.

Chapter 8:
Summary & Conclusions about Lead-Based Anode Materials

In Chapter 5, the intermediates and end phase in the dynamic electrochemical lithiation of lead in 1 M $LiPF_6$ in 1:1 FEC/DEC (w/w) at room temperature were re-determined using *ex situ* XRD measurements. They were found to be LiPb, Li_8Pb_3, Li_3Pb, and Li_7Pb_2. From these phases and their relaxation potentials, a new set of reaction stages was proposed which agreed well with the electrochemical data. The resulting theoretical capacity of lead as a lithium-ion battery material is 453 mAh g^{-1}.

In Chapter 6, PbO and PbTe were synthesized by relatively simple wet chemical routes and electrochemically characterized in lithium-ion half cells. For both materials Li-Pb alloys were formed and electrolyzed in the 0.01 – 0.7 V vs. Li/Li^+ potential domain. In the 0.8 – 2.5 V vs. Li/Li^+ potential domain, lithium tellurides were reversibly formed and electrolyzed for PbTe while no reactions occurred for PbO. The lithium tellurides accelerated the formation and electrolysis of the Li-Pb alloys, providing for rapid, stable cycling of the electrodes at a 5C rate at half their C/5 capacity. The lithium oxide, on the other hand, did not provide any improvement or stability, and the capacity of PbO faded rapidly.

In Chapter 7, the lithiation/delithiation of electrodes made with slurry-cast galena PbS particles was studied. When cycled in the 0.01 – 1.0 V range, the electrodes did not lose their sulfur; when cycled in the 0.01 – 3.0 V range, they lost their sulfur through lithium polysulfide dissolution. Following the dissolution of sulfur, the specific capacities were similar for 100 cycles whether the cutoff was 1.0 V or 3.0 V. The overpotentials were smaller when sulfur was retained, possibly due to contamination of the electrolyte and/or lithium counter electrode with dissolved polysulfides or from the Li_2S preventing electrochemical sintering of the Pb particles. At higher rates, the presence of sulfur

provided for higher capacities of Li alloying and de-alloying with Pb. The PbS electrode was clearly inferior to the earlier-studied PbTe electrode, as its capacity faded substantially and rapidly through 100 cycles.

In Chapter 8, the study of PbSe showed that formation of an electroactive polymer gel film (PGF) during cycling added to the overall capacity, raising it by up to 300 mAh g^{-1} above its theoretical value of 515 mAh g^{-1}. This PGF was oxidatively stripped when the electrode was cycled up to 3.0 V. The study also showed that in the initial reaction a Li atom was inserted into the PbSe lattice without changing the phase, i.e. crystal structure, in order to form Li(PbSe).

Most of the chalcogenides studied did not show the requisite performance necessary for commercial lithium-ion batteries, thus precluding their use. PbTe showed some promising characteristics, with its ability to charge and discharge rapidly without losing too much of its capacity. The expense of this material, however, would negate these potential benefits, and it would not be feasible at a large scale. Additional study of Pb-based materials is warranted; with appropriate tuning, lead could still potentially meet the requirements of large grid-scale battery applications. Because of its high density, lead also has a large volumetric capacity compared to other materials, potentially recommending its use in other applications where battery volume is an important consideration.

SECTION 3:
LITHIUM METAL AS AN ANODE MATERIAL

Chapter 9:
Potassium Additive to Reduce Dendrites on Lithium Metal[**]

INTRODUCTION

Lithium-ion batteries were developed after the failed introduction of batteries with metallic lithium anodes, which were plagued by over-pressurization and fires caused by the growth of lithium dendrites. The smaller, lighter and more reducing metallic lithium anodes were replaced by the heavier, bulkier and less reducing lithium-intercalating graphite anodes of Samar Basu.[1,2] When Wertheim, Van Attekum, and Basu showed that the lithium in graphite is ionized,[3] batteries with graphite anodes became known as "lithium-ion batteries". Although all manufactured rechargeable lithium batteries are presently lithium-ion batteries,[4,5] exploration of batteries with dendrite-free metallic lithium anodes continues.[6]

Dendrites form when lithium is unevenly electrodeposited on the lithium foil surface because of (a) inadequate nucleation or (b) a thick Li^+-depleted electrolyte layer proximal to the electrode when the current density is high. The dendrites traverse the concentration-polarized depletion layer such that a highly porous network of thin lithium fibers develops, extending through the layer.[7] When the current density is low and the depletion layer is thin, dendrites grow because of inadequate nucleation. The metallic lithium surface is passivated by an electronically and ionically insulating solid electrolyte interphase (SEI) layer; lithium nucleates only in its defects. The surface density of Li-nucleating defects depends on the thickness and Li^+ permeability of the SEI: the thinner

[**] This work has been submitted for publication at the time of the writing of this dissertation: Sean M. Wood, Codey H. Pham, Rodrigo Rodriguez, Sindhu S. Nathan, Andrei D. Dolocan, Hugo Celio, J. Pedro de Souza, Kyle C. Klavetter, Adam Heller, C. Buddie Mullins, "K^+ reduces lithium dendrite growth by forming a thin, Li_2CO_3-rich solid electrolyte interphase", *J. Am. Chem. Soc.*, submitted. The author of the dissertation was responsible for development of experiments, electrochemical measurements, characterization of XPS and TOF-SIMS data, and data analysis.

and more Li^+-permeable it is, the greater the surface density of Li-nuclei. Because the permeability is the product of the concentration and diffusivity of Li^+ in the SEI, it increases when the diffusivity is unchanged but the Li^+ concentration is increased. When the SEI is thin enough and its Li^+ permeability high enough, then in the absence of concentration polarization no dendrites grow.[8]

Approaches to address nucleation insufficiency through thinning of the SEI include replacement of the carbonate-based electrolytes by more expensive ionic liquids,[9–12] partial fluorination of the carbonates,[13] and blending with halogen-containing salts.[14] Alternatively, Cs^+ and Rb^+ salts added to the carbonate-based electrolytes to electrostatically shield protuberant lithium tips, form a nanocolumnar solid electrolyte interphase (SEI), and enrich the interphase in LiF.[15–17] In some of these approaches, the SEI-modifying additive reacted with lithium, and dendritic growth resumed once the additive was eventually exhausted.

Here it is shown that adding 10 mM KPF_6 to the widely used 1 M $LiPF_6$ ethylene carbonate (EC)/dimethyl carbonate (DMC) (1:1 v/v) electrolyte favorably alters the SEI. The KPF_6 depletes the SEI of the organic polymer formed upon reduction of EC-solvated Li^+, $(CH_2OCO_2Li)_2$, (lithium ethylene dicarbonate, abbr. LiEDC) and enriches the fraction of Li_2CO_3 8.6-fold, raising it to 88%. The Li_2CO_3-enriched SEI is thin enough and sufficiently Li^+-permeable for the electrodeposition of dense, smooth, dendrite-free metallic lithium at a low current density of 0.5 mA cm^{-2}. At the intermediate current density of 2.5 mA cm^{-2} dendrites persist, but the surface density of dendrites is vastly reduced.

EXPERIMENTAL INFORMATION

Except in the experiments involving an optical cell for photographing the dendrites, symmetrical Li | Li CR2032 coin cells with Li foil (Alfa Aesar) disk electrodes were used. Electrolytes were prepared by mixing a 1:1 (v/v) ratio of ethylene carbonate (EC, BASF) and dimethyl carbonate (DMC, Sigma-Aldrich) and dissolving 1 M of $LiPF_6$ (BASF) therein. In half the experiments, 10 mM KPF_6 (Sigma-Aldrich) was also dissolved (10 mM was found to be the optimal concentration out of the 1 mM, 10 mM, and 100 mM concentrations tried). The cells had Celgard 2400 polypropylene membranes as separators. They were assembled in an argon-atmosphere glovebox (MBRAUN) with less than 0.1 ppm of O_2 and less than 0.1 ppm of H_2O. An Arbin BT 2143 multichannel battery testing system was used for galvanostatic cycling.

Electrochemical impedance spectra (EIS) were measured with a CH Instruments 604D electrochemical analyzer between 10 mHz and 100 kHz with an amplitude of 5 mV. The spectra were analyzed with ZView software using the fitting parameters of the model shown in Figure 9.5b.

X-ray photoelectron spectra (XPS) were obtained with a Kratos Axis Ultra X-ray photoelectron spectrometer, having a monochromatic Al-Kα X-ray source ($h\nu$ = 1486.5 eV). The XPS samples were prepared by submerging pristine Li foil disks in the respective electrolyte solutions for 48 hours and briefly dipping in DMC to remove any residual $LiPF_6$. Samples were transferred from the Argon-filled glovebox to the XPS ultra-high vacuum (UHV) chamber using the pressure-to-vacuum transfer of environmentally sensitive samples (PV-TESS) interface designed by the Texas Materials Institute of The University of Texas at Austin.[18] CasaXPS analysis software was used to evaluate the spectra and provide corrected peak locations. Binding energies were calibrated using the adventitious carbon peak in the C 1s spectra aligned to 284.8 eV.

Time of flight – secondary ion mass spectrometric (TOF-SIMS) depth profiles were obtained using the TOF.SIMS 5 by ION-TOF GmbH, 2010. The electrolyte-exposed Li metal samples were transferred to the TOF-SIMS under an Ar atmosphere using the same transfer vessel as above. Non-interlaced mode was used with the sputtering and analysis beams alternating on the sampled area. A Bi^+ analysis beam (0.4 pA, 30 keV) was rastered over a 100 μm x 100 μm area, segmented into 256 pixels x 256 pixels in high current mode. In negative mode, a sputtering beam of Cs^+ ions (78 nA, 2 keV) impinged upon a 300 μm x 300 μm area. Cs was chosen so as to decrease the work function of the material and to increase the counts of negative species. In positive mode, an O_2 sputtering beam (307 nA, 1 keV) was used to increase the work function of the sample and accentuate the potassium signal so as to detect potassium traces in the surface.

Dendritic growth was observed and photographed *in situ* in a home-built optical cell, its schematic shown in Figure 9.1a. The body of the cell was made of high-density polyethylene; the cell had ports for electrolyte injection, stainless steel leads for electric connection, and a cutout for a polypropylene insert. It was hermetically sealed by an O-ring and a quartz glass lid fitted to a stainless steel cover. O-rings were used to seal the Swagelok electrolyte ports. The photographs were taken through the glass lid.

The cell's insert, shown in Figure 9.1b, was printed by Solid Prototype in white, poly-P-endur. It contained 5 mm x 5 mm x 1mm slots for the Li metal strips, with 1 mm x 2 mm inner face edges exposed for Li deposition and stripping. The insert also contained pathways for evolved gas to escape to side-spaces. Ports were included to connect the insert to the electrolyte and for the electrical leads. The Li foils and the potentiostat were connected by a stainless steel foil, springs (Century Spring Corp, Model 70047s), disks, and screws attached to an external wire. 5 mm x 5 mm Li electrodes were

punched from lithium foil with a stainless steel punch. The electrodes were soaked in electrolyte for at least 48 hours prior to cell assembly.

(a)

Stainless Steel Cover

Glass Lid

O28 O-ring

Assembled body + insert

Swagelok electrolyte port

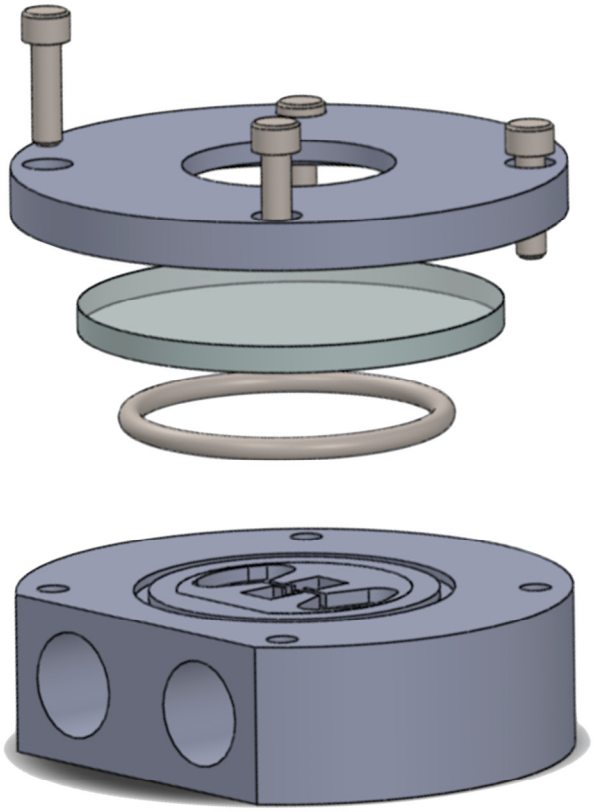

Figure 9.1. Continued on next page.

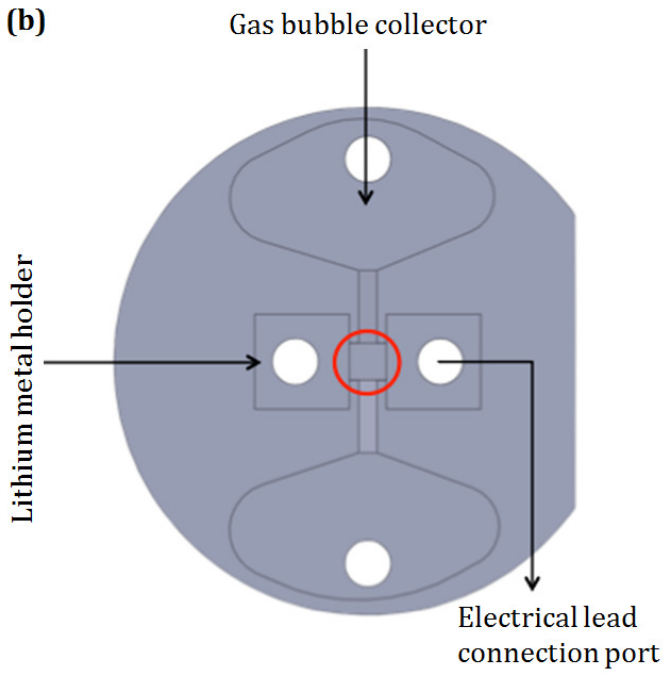

Figure 9.1. (a, previous page) Schematic of the homemade electrochemical cell used to perform optical microscopy. (b, above) Schematic of the 3D printed plastic insert used to hold the lithium metal in the homemade electrochemical cell of (a).

Photographs were taken with a camera-equipped Keyence VHX-5000 digital microscope. A VH-250R lens was used to capture images of the lithium foil edge at 500x magnification before and after the electrodepositions of Li either at a current density of 0.5 mA cm^{-2} for 18 hours or at 2.5 mA cm^{-2} for 3 hours and 36 minutes, both providing 9 mAh cm^{-2}. The current was applied using a CHI 604D electrochemical analyzer.

RESULTS & DISCUSSION

Photographs of metallic lithium/electrolyte interfaces taken after 18 h of lithium deposition at a current density of 0.5 mA cm^{-2} show a vast change when 10 mM KPF_6 was added to the 1M $LiPF_6$ EC/DMC electrolyte (Figure 9.2). In the absence of KPF_6, the electrodeposited lithium was porous and had numerous protrusions, indicated by red arrows. In its presence, the electrodeposited lithium was smooth, dense, and free of

protrusions. When the same total amount of charge was passed but at a 5-fold higher current density for a 5-fold shorter period (i.e. 2.5 mA cm^{-2} for 3.6 hours), the change when 10 mM KPF_6 was added to the electrolyte was similarly vast (Figure 9.3); some fibrous dendrites persisted (indicated by red arrows) but their number was at least 100 times smaller. Gas bubbles (not shown) were observed proximal to the lithium surface at this current density both in the presence and absence of KPF_6.

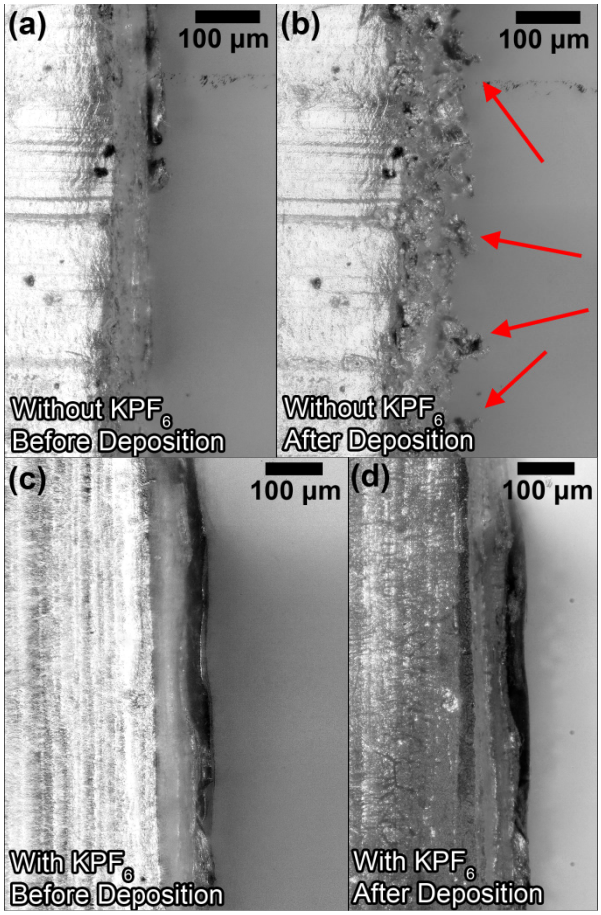

Figure 9.2. Photographs of the lithium foil (left side of each image)/electrolyte (right side of each image) interface before (a, c) and after (b, d) 18 h of lithium deposition at a current density of 0.5 mA cm^{-2} in 1M $LiPF_6$ in 1:1 EC/DMC (v/v) electrolyte without (a, b) and with (c, d) 10 mM KPF_6 added. Red arrows point to lithium protrusions. The view is normal to the plane of the lithium foil.

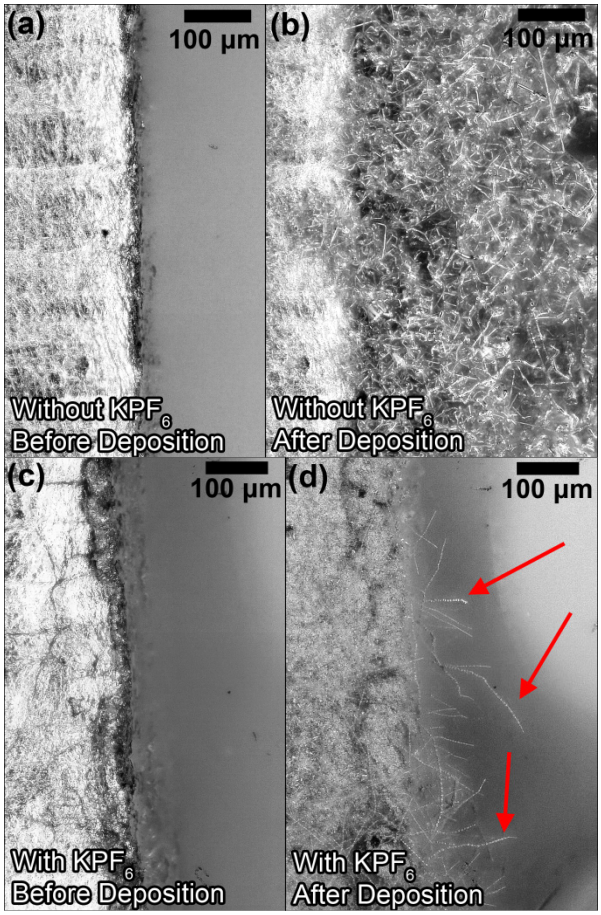

Figure 9.3. Photographs of the lithium foil (left side of each image)/electrolyte (right side of each image) interface before (a, c) and after (b, d) 3 h 36 min of lithium deposition at a current density of 2.5 mA cm^{-2} in 1M $LiPF_6$ in 1:1 EC/DMC (v/v) electrolyte without (a, b) and with (c, d) 10 mM KPF_6 added. Red arrows indicate the much sparser needle-like dendrites grown in the presence of KPF_6. The view is normal to the plane of the lithium foil.

Figure 9.4 shows that the adding of 10 mM KPF_6 also drastically lowered the resistance of the SEI formed on lithium foil electrodes when aged for 2 days at open circuit. When a current density of 1 mA cm^{-2} was applied across lithium foil electrode pairs aged in 1M $LiPF_6$ in 1:1 EC/DMC without KPF_6, the voltage increased promptly to 4 V as the feedback loop of the Arbin system attempted to adjust for the high resistance. It then oscillated as the feedback loop periodically re-adjusted the voltage for the

decreasing resistance, dropping after 2 min to 0.5 V. In contrast, with the 10 mM KPF_6 added the resistance remained low and the voltage never exceeded 0.5 V, which was consistent with a more Li^+ conductive SEI.

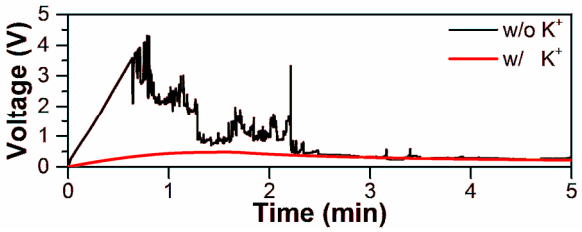

Figure 9.4. Time dependence of the initial voltage of symmetrical Li | Li cells at an applied current density of 1 mA cm^{-2} after 48 h aging at open circuit in 1 M $LiPF_6$ in EC/DMC (1:1 v/v) electrolyte without and with KPF_6 added.

A less resistive SEI was corroborated by the drastic change in the Nyquist plots upon adding 10 mM KPF_6 (Figure 9.5a). The plots comprise parts attributed to Ohmic resistance, provided by the x-intercept in the high-frequency region, and to the surface resistance, represented by the depressed semicircle in the low frequency region.[19] The Ohmic resistance is the inverse of the ionic conductivity of the electrolyte, while the surface resistance results from the electronic and/or ionic insulation, mostly of the SEI. The low-frequency semicircle can be modeled with the equivalent circuit in Figure 9.5b. The summed surface resistances ($R_2 + R_3 + R_4$) were 2,192 Ω in the absence of KPF_6 and 408 Ω in the presence of KPF_6. Aptly, addition of K_2CO_3 was reported earlier to reduce the resistance of a lithium-intercalating graphite electrode.[20]

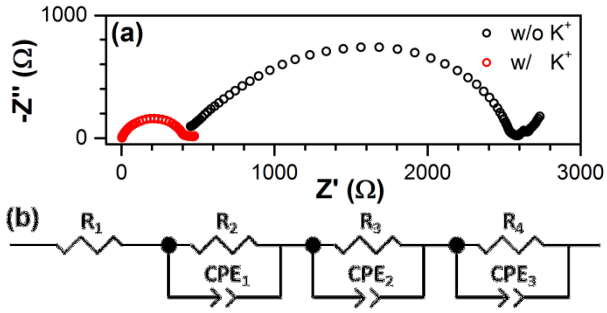

Figure 9.5. (a) Nyquist plots derived from EIS spectra of Li | Li symmetric cells after aging for 48 h in 1M $LiPF_6$ in EC/DMC electrolyte without and with 10 mM KPF_6. (b) The equivalent circuit applied to fit the impedance spectra.

X-ray photoelectron spectra (XPS) of the SEI (Figure 9.6) showed that in the absence of 10 mM KPF_6 the SEI was thick and mostly organic, i.e. polymeric LiEDC, while in its presence it was thin and mostly Li_2CO_3. In the Li 1s spectra, the KPF_6 increased both the metallic Li band[21] and the Li^+ band, indicating a thin, dense SEI. In the O 1s spectra, where the LiEDC and Li_2CO_3 peaks were readily distinguishable,[22–24] the Li_2CO_3/LiEDC ratio was 0.85 in the absence of KPF_6 which increased 8-fold to 7.3 in its presence. The F 1s peak increased in the presence of KPF_6 and when paired with the larger metallic Li band of the Li 1s spectrum, it was consistent with that of a thinner denser LiF layer. The C 1s spectra (the adventitious carbon peak of which was used to align the other spectra) and the P 2p spectra are also shown in Figure 9.6.

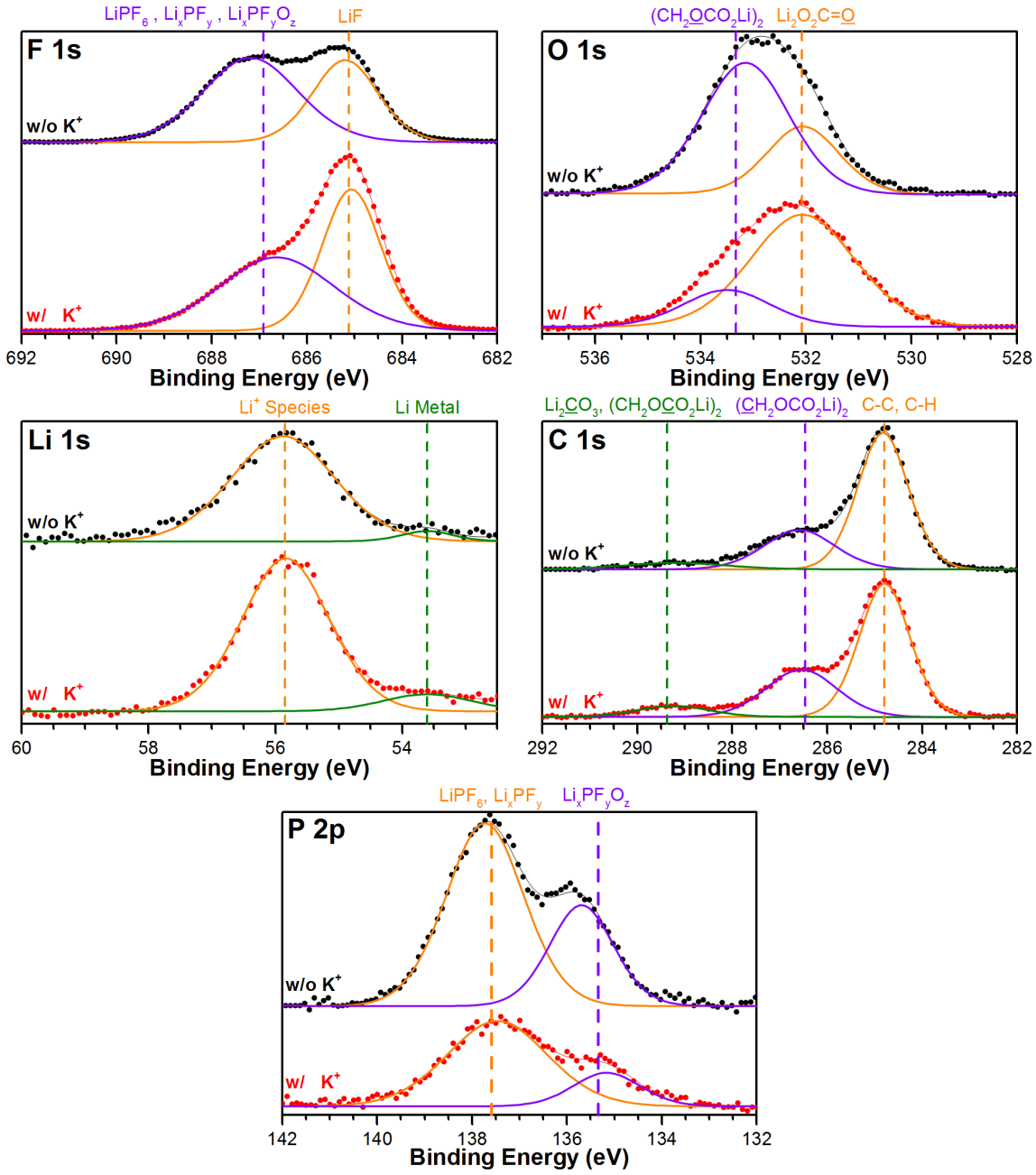

Figure 9.6. F 1s, O 1s, Li 1s, C 1s, and P 2p XPS spectra of the surface of Li foil after aging in 1M $LiPF_6$ in 1:1 EC/DMC (v/v) for 48 h with and without the 10 mM KPF_6.

Time of flight-secondary ion mass spectra (TOF-SIMS) of the SEI are shown in Figure 9.7. Based on instrumental settings and calibrations performed elsewhere, one second of sputtering time corresponds to roughly 1 nm of depth.[25] The C_2HO^- fragment originates from the middle carbons of lithium ethylene dicarbonate, whereas the CO_3^- fragment originates from carbonate. As seen in Figure 9.7a, the ratio of the C_2HO^-/CO_3^- fragments was lowered and persisted only through a shorter sputtering time, i.e. a lesser depth, when 10 mM of KPF_6 was added, supporting the thinning of the SEI and its CO_3^{2-} enrichment. The LiF_2^- fragment in Figure 9.7b serves as a proxy for LiF in the SEI; its counts dropped off more rapidly when KPF_6 was added, consistent with a thin layer of LiF. Without KPF_6, the LiF layer was thicker and persisted at a greater depth.

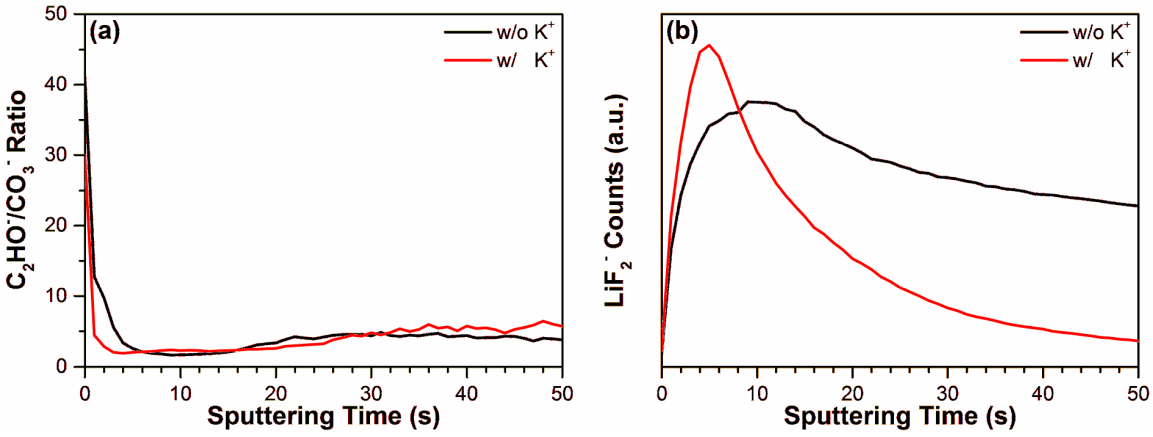

Figure 9.7. TOF-SIMS spectra of the surface of Li foil submerged in 1M $LiPF_6$ in 1:1 EC/DMC (v/v) electrolyte for 48 h with and without the 10 mM KPF_6 showing (a) the ratio of the counts of the CH_2O^- fragment to the CO_3^- fragment and (b) the counts of the LiF_2^- fragment.

Figure 9.8 compares the voltage excursions in symmetrical Li | Li cells without and with KPF_6 cycling at 0.5 mA cm^{-2}, the direction of the current reversed every hour. Addition of 10 mM KPF_6 reduced the baseline voltage 2 - 5 fold to ~50 mV through the

18 days of cycling, as expected for electrodes with a more Li^+-conducting SEI layer. In the absence of KPF_6, the voltage averaged 200 - 250 mV on the first day of cycling and 100 - 150 mV on the 18th day. The halving of the voltage is attributed to current density reduction as a result of surface roughening, i.e. dendritic protrusions.[19] The large, sudden voltage drops detected after cycling for more than 14 days in the absence of KPF_6 (marked with arrows in Figure 9.9) are attributed to shorting by dendrites.

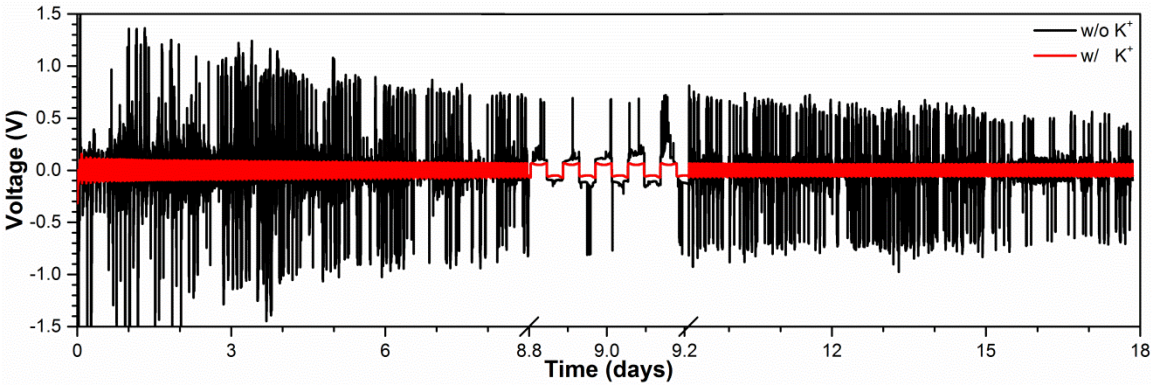

Figure 9.8. Voltage of Li | Li symmetric cells with and without KPF_6 added to the 1M $LiPF_6$ in 1:1 EC/DMC (v/v) electrolyte at an applied current density of 0.5 mA cm^{-2} reversed every 1 hour.

Additionally, 20 – 30 daily voltage excursions as large as 0.7 – 1.5 V were observed in the absence of KPF_6, but not a single excursion was seen during the 18 days of cycling when 10 mM KPF_6 was added. Such large voltage excursions were earlier observed by Howlett et al. in symmetrical Li | Li cells with a 1 M $LiPF_6$ in propylene carbonate electrolyte and by Song et al. in Li | Li cells with a 1 M $LiPF_6$ in EC/ethyl methyl carbonate electrolyte.[13] Howlett et al. associated the voltage excursions with dendritic growth resulting in formation of dead lithium. This electrically disconnected lithium reduced the conductance of the cells, lowering the active surface area of the electrodes (by physically preventing lithium ions from reaching the surface), in turn

increasing the current density and further promoting dendritic deposition.[9] The dead lithium deposit also reduced the volume of the electrolyte near the surface, increasing the Li^+ concentration gradient and promoting dendritic deposition.[9] The symmetrical cell of Song et al. exploded after 10 cycles, its explosion attributed to dendrite formation.[13]

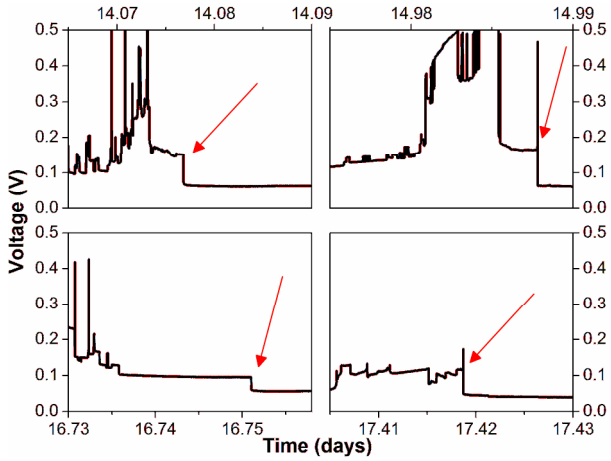

Figure 9.9. Zoomed-in voltage versus time plots for Li | Li symmetric cells cycled at 0.5 mA cm^{-2} reversed every 1 h in a 1M $LiPF_6$ in 1:1 EC/DMC electrolyte without K^+ additive. Arrows show dendritic shorting events.

In Figure 9.10, the current density was increased to 2.5 mA cm^{-2}. Large voltage excursions of the type seen in Figure 9.8 were not observed. However, after 2 days of cycling the voltage increased rapidly towards the end of each cycle. This behavior may be more indicative of continuous SEI buildup rather than dendrite formation.[19,26]

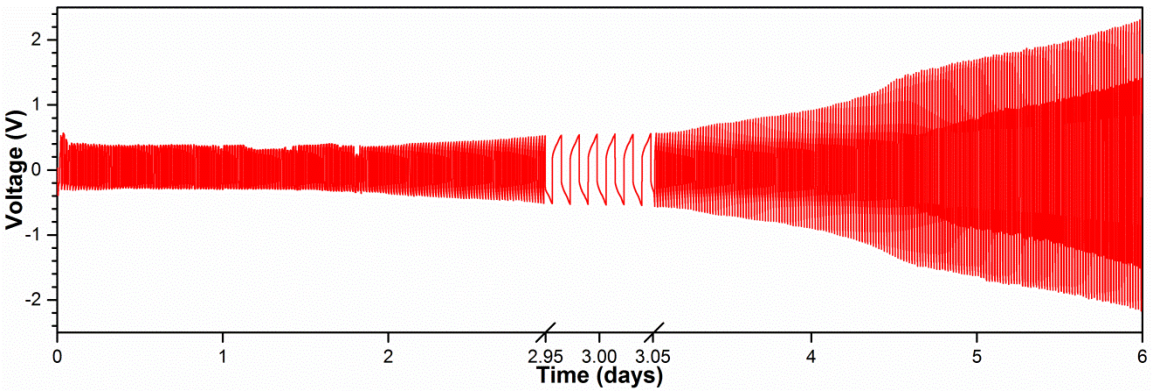

Figure 9.10. Voltage of Li | Li symmetric cell with KPF_6 added to the 1M $LiPF_6$ in 1:1 EC/DMC (v/v) electrolyte at an applied current density of 2.5 mA cm^{-2} reversed every 12 min.

The benefits of KPF_6 are attributed to the difference in solvations of Li^+ and K^+. Experimental[27,28] and theoretical[29–31] studies have shown that Li^+ is solvated almost exclusively by EC in EC/DMC; it is the EC that is preferentially electroreduced[31–33] to form an SEI comprised of both Li_2CO_3 (Equation 9.1) and LiEDC (Equation 9.2).[20,34–37] The ratio Li_2CO_3/LiEDC is determined by the relative rates of the two reactions.

Equation 9.1. $EC + 2\ Li^+ + 2\ e^- \rightarrow Li_2CO_3\downarrow + H_2C{=}CH_2\uparrow$

Equation 9.2. $2\ EC + 2\ Li^+ + 2\ e^- \rightarrow (CH_2OCO_2Li)_2\downarrow + H_2C{=}CH_2\uparrow$

When the concentration of EC in the EC/DMC solution is high, Equation 9.2 is sterically favored because the Li^+ is increasingly solvated by EC.[38,39] When the EC concentration is low, Equation 9.1 dominates. Being a small cation, Li^+ is solvated on average by 4 EC molecules,[40] whereas the large K^+ cation is solvated by only a single EC molecule.[41] Hence during the electroreduction of K^+ as in (Equation 9.3), only a single solvent molecule is reduced, and carbonate and ethylene are produced.

Equation 9.3. $EC + 2\ K^+ + 2\ e^- \rightarrow K_2CO_3\downarrow + H_2C{=}CH_2\uparrow$

Equation 9.2, in which four solvent molecules are released, is expected to have a large Marcus reorganization energy and to be slow. With only a single solvent molecule released, Equation 9.3 is expected to have a lesser Marcus reorganization energy and be so much faster that it would be the dominant reaction,[42] even though the K^+ concentration is only 10 mM, two orders of magnitude lower than the Li^+ concentration. Because the only solution-phase product of the reaction is CO_3^{2-} and because the concentration of Li^+ is 100 times greater than the concentration of K^+, only the solubility product of the less soluble Li_2CO_3 is exceeded and only Li_2CO_3 precipitates to form the SEI, explaining the absence of any K^+ salt. While no potassium was detected in the SEI by energy dispersive X-ray (EDX) spectroscopy or XPS (Figure 9.11a and Figure 9.11b), the highly sensitive TOF-SIMS did detect a trace, but it also detected traces of sodium, aluminum, and calcium, none of which was intentionally added. As seen in Figure 9.11c, the ratio of sodium to potassium ions did not change upon sputtering whether or not KPF_6 was added, confirming that the potassium was an adventitious surface impurity rather than an SEI constituent originating from the KPF_6 salt.

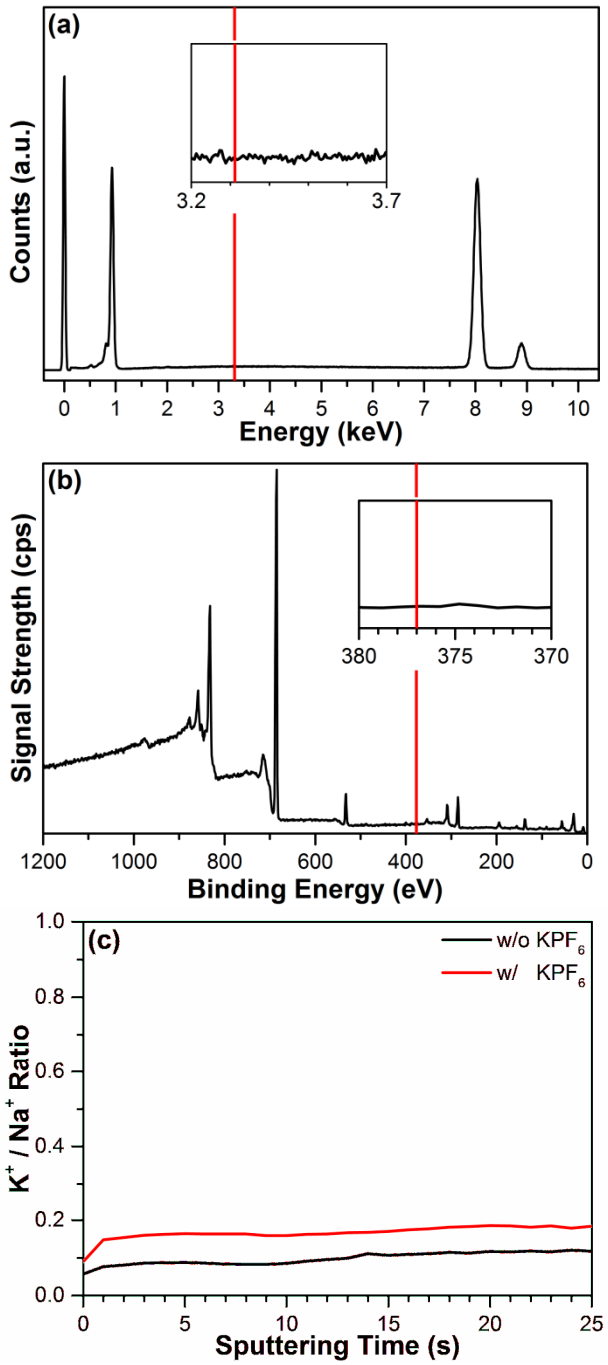

Figure 9.11. (a) EDX spectrum and (b) XPS spectrum showing no K^+ present on the surface of Li foil submerged in 1M $LiPF_6$ in 1:1 EC/DMC (v/v) electrolyte with 10 mM KPF_6. (c) TOF-SIMS spectra showing the ratio of K^+ to Na^+ fragment counts from the surface of Li foil submerged in 1M $LiPF_6$ in 1:1 EC/DMC (v/v) electrolyte without and with 10 mM KPF_6.

CONCLUSIONS

These results agree with the finding of Aurbach et al. who reported that Li_2CO_3 is one of the best passivating agents of Li electrodes and that surface films comprised of Li_2CO_3 are thin, compact, and have low interfacial impedance.[43] The Li_2CO_3-rich SEI formed on the non-intercalating lithium foil electrodes of Li | Li cells with a 1 M $LiPF_6$ in EC/DMC electrolyte with 10 mM KPF_6 added was sufficiently thin and Li^+-permeable to provide ample nucleation for the electrodeposition of a smooth, dense, dendrite-free lithium film at a 0.5 mA cm^{-2} current density where the depletion layer is thin. Although it reduces the surface density of dendrites at least 100-fold while at a 2.5 mA cm^{-2} current density, it is unlikely to eliminate dendrites at the typical 10 mA cm^{-2} current density where the depletion layer is thick.

REFERENCES

(1) Basu, S. Ambient Temperature Rechargeable Battery. US Patent 4,423,125, 1983.

(2) Basu, S. Rechargeable Battery. US Patent 4,304,825, 1981.

(3) Wertheim, G. K.; Van Attekum, P. T. T. M.; Basu, S. Electronic Structure of Lithium Graphite. *Solid State Commun.* **1980**, *33* (11), 1127–1130.

(4) Aurbach, D.; Zinigrad, E.; Cohen, Y.; Teller, H. A Short Review of Failure Mechanisms of Lithium Metal and Lithiated Graphite Anodes in Liquid Electrolyte Solutions. *Solid State Ionics* **2002**, *148* (3-4), 405–416.

(5) Aurbach, D. Review of Selected Electrode-Solution Interactions Which Determine the Performance of Li and Li Ion Batteries. *J. Power Sources* **2000**, *89* (2), 206–218.

(6) Xu, W.; Wang, J.; Ding, F.; Chen, X.; Nasybulin, E.; Zhang, Y.; Zhang, J.-G. Lithium Metal Anodes for Rechargeable Batteries. *Energy Environ. Sci.* **2014**, *7*, 513.

(7) Mayers, M. Z.; Kaminski, J. W.; Miller, T. F. Suppression of Dendrite Formation via Pulse Charging in Rechargeable Lithium Metal Batteries. *J. Phys. Chem. C* **2012**, *116* (50), 26214–26221.

(8) Aurbach, D.; Zaban, A.; Gofer, Y.; Ely, Y. E.; Weissman, I.; Chusid, O.; Abramson, O. Recent Studies of the Lithium-Liquid Electrolyte Interface Electrochemical, Morphological and Spectral Studies of a Few Important Systems. *J. Power Sources* **1995**, *54* (1), 76–84.

(9) Howlett, P. C.; MacFarlane, D. R.; Hollenkamp, A. F. A Sealed Optical Cell for the Study of Lithium-Electrodelelectrolyte Interfaces. *J. Power Sources* **2003**, *114*, 277–284.

(10) Howlett, P. C.; MacFarlane, D. R.; Hollenkamp, A. F. High Lithium Metal

Cycling Efficiency in a Room-Temperature Ionic Liquid. *Electrochem. Solid-State Lett.* **2004**, *7* (5), A97–A101.

(11) Goodman, J. K. S.; Kohl, P. A. Effect of Alkali and Alkaline Earth Metal Salts on Suppression of Lithium Dendrites. *J. Electrochem. Soc.* **2014**, *161* (9), D418–D424.

(12) Kim, H.; Ding, Y.; Kohl, P. A. LiSICON – Ionic Liquid Electrolyte for Lithium Ion Battery. *J. Power Sources* **2012**, *198*, 281–286.

(13) Song, J.-H.; Yeon, J.-T.; Jang, J.-Y.; Han, J.-G.; Lee, S.-M.; Choi, N.-S. Effect of Fluoroethylene Carbonate on Electrochemical Performances of Lithium Electrodes and Lithium-Sulfur Batteries. *J. Electrochem. Soc.* **2013**, *160* (6), A873–A881.

(14) Lu, Y.; Tu, Z.; Archer, L. A. Stable Lithium Electrodeposition in Liquid and Nanoporous Solid Electrolytes. *Nat. Mater.* **2014**, *13* (October), 961–969.

(15) Ding, F.; Xu, W.; Graff, G. L.; Zhang, J.; Sushko, M. L.; Chen, X.; Shao, Y.; Engelhard, M. H.; Nie, Z.; Xiao, J.; Liu, X.; Sushko, P. V.; Liu, J.; Zhang, J. G. Dendrite-Free Lithium Deposition via Self-Healing Electrostatic Shield Mechanism. *J. Am. Chem. Soc.* **2013**, *135* (11), 4450–4456.

(16) Zhang, Y.; Qian, J.; Xu, W.; Russell, S. M.; Chen, X.; Nasybulin, E.; Bhattacharya, P.; Engelhard, M. H.; Mei, D.; Cao, R.; Ding, F.; Cresce, A. V; Xu, K.; Zhang, J. Dendrite-Free Lithium Deposition with Self-Aligned Nanorod Structure. *Nano Lett.* **2014**, *14*, 6889–6896.

(17) Ding, F.; Xu, W.; Chen, X.; Zhang, J.; Shao, Y.; Engelhard, M. H.; Zhang, Y.; Blake, T. A.; Graff, G. L.; Liu, X.; Zhang, J. G. Effects of Cesium Cations in Lithium Deposition via Self-Healing Electrostatic Shield Mechanism. *J. Phys. Chem. C* **2014**, *118* (8), 4043–4049.

(18) Celio, H. Interface Designed with Differential Pumping and Built-in Figure of

Merit Method to Monitor Chambers Where Environmentally Sensitive Samples Are Prepared and Transferred for Analysis. US Patent Application 14/445,650, 2014.

(19) Bieker, G.; Bieker, P. M.; Winter, M. Electrochemical *In situ* Investigations of the SEI and Dendrite Formation on the Lithium Metal Anode. *Phys. Chem. Chem. Phys.* **2015**, *17*, 8670–8679.

(20) Zhuang, Q. C.; Li, J.; Tian, L. L. Potassium Carbonate as Film Forming Electrolyte Additive for Lithium-Ion Batteries. *J. Power Sources* **2013**, *222*, 177–183.

(21) Leroy, S.; Blanchard, F.; Dedryvère, R.; Martinez, H.; Carré, B.; Lemordant, D.; Gonbeau, D. Surface Film Formation on a Graphite Electrode in Li-Ion Batteries: AFM and XPS Study. *Surf. Interface Anal.* **2005**, *37* (10), 773–781.

(22) Nadimpalli, S. P. V; Sethuraman, V. a.; Dalavi, S.; Lucht, B.; Chon, M. J.; Shenoy, V. B.; Guduru, P. R. Quantifying Capacity Loss due to Solid-Electrolyte-Interphase Layer Formation on Silicon Negative Electrodes in Lithium-Ion Batteries. *J. Power Sources* **2012**, *215*, 145–151.

(23) Nie, M.; Abraham, D. P.; Chen, Y.; Bose, A.; Lucht, B. L. Silicon Solid Electrolyte Interphase (SEI) of Lithium Ion Battery Characterized by Microscopy and Spectroscopy. *J. Phys. Chem. C* **2013**, *117* (26), 13403–13412.

(24) Chan, C. K.; Ruffo, R.; Hong, S. S.; Cui, Y. Surface Chemistry and Morphology of the Solid Electrolyte Interphase on Silicon Nanowire Lithium-Ion Battery Anodes. *J. Power Sources* **2009**, *189* (2), 1132–1140.

(25) Zu, C.; Dolocan, A.; Xiao, P.; Stauffer, S.; Henkelman, G.; Manthiram, A. Breaking Down the Crystallinity: The Path for Advanced Lithium Batteries. *Adv. Energy Mater.* **2015**, *1501933*, 1–9.

(26) Liang, Z.; Lin, D.; Zhao, J.; Lu, Z.; Liu, Y.; Liu, C.; Lu, Y.; Wang, H.; Yan, K.; Tao, X.; Cui, Y. Composite Lithium Metal Anode by Melt Infusion of Lithium into a 3D Conducting Scaffold with Lithiophilic Coating. *Proc. Natl. Acad. Sci.* **2016**, *113* (11), 2862–2867.

(27) Matsuda, Y.; Fukushima, T.; Hashimoto, H.; Arakawa, R. Solvation of Lithium Ions in Mixed Organic Electrolyte Solutions by Electrospray Ionization Mass Spectroscopy. *J. Electrochem. Soc.* **2002**, *149* (8), A1045–A1048.

(28) Jeong, S. K.; Inaba, M.; Iriyama, Y.; Abe, T.; Ogumi, Z. Surface Film Formation on a Graphite Negative Electrode in Lithium-Ion Batteries: AFM Study on the Effects of Co-Solvents in Ethylene Carbonate-Based Solutions. *Electrochim. Acta* **2002**, *47* (12), 1975–1982.

(29) Bhatt, M. D.; Cho, M.; Cho, K. Density Functional Theory Calculations for the Interaction of Li+ Cations and PF6- Anions with Nonaqueous Electrolytes. *Can. J. Chem.* **2011**, *89* (12), 1525–1532.

(30) Seo, D. M.; Reininger, S.; Kutcher, M.; Redmond, K.; Euler, W. B.; Lucht, B. L. Role of Mixed Solvation and Ion Pairing in the Solution Structure of Lithium Ion Battery Electrolytes. *J. Phys. Chem. C* **2015**, *119*, 14038–14046.

(31) Wang, Y.; Balbuena, P. B. Theoretical Studies on Cosolvation of Li Ion and Solvent Reductive Decomposition in Binary Mixtures of Aliphatic Carbonates. *Int. J. Quantum Chem.* **2005**, *102* (5), 724–733.

(32) Ein-Eli, Y.; Markovsky, B.; Aurbach, D.; Carmeli, Y.; Yamin, H.; Luski, S. The Dependence of the Performance of Li-C Intercalation Anodes for Li-Ion Secondary Batteries on the Electrolyte Solution Composition. *Electrochim. Acta* **1994**, *39* (17), 2559–2569.

(33) Yang, C. R.; Wang, Y. Y.; Wan, C. C. Composition Analysis of the Passive Film

on the Carbon Electrode of a Lithium-Ion Battery with an EC-Based Electrolyte. *J. Power Sources* **1998**, *72*, 66–70.

(34) Xu, S. D.; Zhuang, Q. C.; Wang, J.; Xu, Y. Q.; Zhu, Y. B. New Insight into Vinylethylene Carbonate as a Film Forming Additive to Ethylene Carbonate-Based Electrolytes for Lithium-Ion Batteries. *Int. J. Electrochem. Sci.* **2013**, *8* (6), 8058–8076.

(35) Xu, S. D.; Zhuang, Q. C.; Tian, L. L.; Qin, Y. P.; Fang, L.; Sun, S. G. Impedance Spectra of Nonhomogeneous, Multilayered Porous Composite Graphite Electrodes for Li-Ion Batteries: Experimental and Theoretical Studies. *J. Phys. Chem. C* **2011**, *115* (18), 9210–9219.

(36) Naji, A.; Ghanbaja, J.; Humbert, B.; Willmann, P.; Billaud, D. Electroreduction of Graphite in LiClO4-Ethylene Carbonate Electrolyte. Characterization of the Passivating Layer by Transmission Electron Microscopy and Fourier-Transform Infrared Spectroscopy. *J. Power Sources* **1996**, *63*, 33–39.

(37) Naji, A.; Ghanbaja, J.; Willmann, P.; Humbert, B.; Billaud, D. First Characterization of the Surface Compounds Formed during the Reduction of a Carbonaceous Electrode in LiClO4-Ethylene Carbonate Electrolyte. *J. Power Sources* **1996**, *62*, 141–143.

(38) Wang, Y.; Nakamura, S.; Ue, M.; Balbuena, P. B. Theoretical Studies to Understand Surface Chemistry on Carbon Anodes for Lithium-Ion Batteries: Reduction Mechanisms of Ethylene Carbonate. *J. Am. Chem. Soc.* **2001**, *123* (47), 11708–11718.

(39) Aurbach, D.; Levi, M. D.; Levi, E.; Schechter, A. Failure and Stabilization Mechanisms of Graphite Electrodes. *J. Phys. Chem. B* **1997**, *101* (12), 2195–2206.

(40) Skarmoutsos, I.; Ponnuchamy, V.; Vetere, V.; Mossa, S. Li+ Solvation in Pure,

Binary and Ternary Mixtures of Organic Carbonate Electrolytes. *J. Phys. Chem. C* **2015**, *119*, 4502–4515.

(41) Wang, H.; Yoshio, M. KPF6 Dissolved in Propylene Carbonate as an Electrolyte for Activated Carbon/graphite Capacitors. *J. Power Sources* **2010**, *195* (4), 1263–1265.

(42) Xiang, H.; Mei, D.; Yan, P.; Bhattacharya, P.; Burton, S. D.; Cresce, A. V. W.; Cao, R.; Engelhard, M. H.; Bowden, M. E.; Zhu, Z.; Polzin, B. J.; Wang, C.-M.; Xu, K.; Zhang, J.-G.; Xu, W. The Role of Cesium Cation in Controlling Interphasial Chemistry on Graphite Anode in Propylene Carbonate-Rich Electrolytes. *ACS Appl. Mater. Interfaces* **2015**, *7*, 20687–20695.

(43) Aurbach, D.; Markovsky, B.; Levi, M. D.; Levi, E.; Schechter, A.; Moshkovich, M.; Cohen, Y. New Insights into the Interactions between Electrode Materials and Electrolyte Solutions for Advanced Nonaqueous Batteries. *J. Power Sources* **1999**, *81-82*, 95–111.

Chapter 10:
Future Research Directions

Based on the studies presented in this dissertation, there are three potential areas for future study. In the first area, as an extension of Chapter 4, the diffusion coefficients of lithium within various Li_xPb compounds would be studied. These values are known for other Si- and Ge-based compounds; studying the diffusion of lithium within lead would help to compare lead with the other Group IVA materials. Since lead is such a large atom, the diffusion coefficient may actually be higher, allowing it to charge and discharge more rapidly than materials such as silicon. This work would be carried out by synthesizing pure forms of the Li_xPb compounds using a melt synthesis technique developed within our lab. In this technique, the two elements lead and lithium would be sealed in a quartz ampule under vacuum and heated in a tube furnace above the melting point of the alloy so as to completely liquefy it and then allowing it to cool to room temperature. The compounds would be extracted from the ampules, ground into a powder, and characterized by XRD. The powder would be made into electrodes (using the conventional slurry casting technique described in Chapter 1) and EIS measurements taken. From the XRD measurements, grain sizes can be calculated which will then be used as the diffusion length in calculating the diffusion coefficient from the EIS data.

The second area of study would be to fully characterize the polymer gel film formed in Chapter 7. Our lab has the capability to grow nanostructured films of metals such as copper or nickel with high surface area for growing as much of the PGF as possible. Additionally, oxygen can be selectively leaked in to partially oxidize the nanostructured metal films. There is some debate in the literature about whether the PGFs grow as a result of nanocrystalline metallic domains within the metal particles or as a result of some sort of catalytic reaction of the Li_2O that forms upon reaction of the metal

oxide with lithium. Controlling the amount of oxide introduced on the metal would allow determination of the origin of these films. Once their origin is determined, they will be fully characterized using XPS and Fourier Transform Infrared (FTIR) spectroscopy to determine their chemical compositions. Performing these experiments on the nanostructured metallic electrodes obviates the need for the polymer binders typically used in typically slurry-cast films which may obfuscate and convolute the results of XPS and FTIR. Full characterization of this film may provide clues as to how to prevent its formation or to potentially utilize it in a controlled fashion to gain extra capacity in lithium-ion batteries.

The third area of study would be to extend the results of Chapter 9 based on the theory of Marcus reorganization presented therein by using bigger ions. The idea would be that bigger ions would be solvated by even fewer solvent molecules and further enrich the SEI in beneficial Li_2CO_3 while more fully suppressing the formation of LiEDC. Examples of other potential larger ions include tetramethylammonium, tetraethylammonium, and tetrabutylammonium. These ions have the benefit of not plating on the surface of the lithium as the Group 1 elements (Na^+, K^+, Rb^+, Cs^+) potentially do. Similar characterization techniques would be performed as in Chapter 9, with potential for additional support of the original theory by collaborating with another group to do computational studies such as Density Functional Theory.

Glossary

- **DMC**: dimethyl carbonate
- **EC**: ethylene carbonate
- **EDX**: energy dispersive X-ray spectroscopy
- **EIS**: electrochemical impedance spectroscopy
- **FEC**: fluoroethylene carbonate
- **GITT**: galvanostatic intermittent titration technique
- **KPF_6**: potassium hexafluorophosphate
- **$LiPF_6$**: lithium hexafluorophosphate
- **mA cm^{-2}**: milliamps per square centimeter
- **mAh g^{-1}**: milliamp-hours per gram
- **SEM**: scanning electron microscopy
- **TOF-SIMS**: time of flight – secondary ion mass spectrometry
- **V**: volts
- **XPS**: X-ray photoelectron spectroscopy
- **XRD**: X-ray diffraction

Bibliography

Abel, P. R., Klavetter, K. C., Heller, A., & Mullins, C. B. (2014). Thin Nanocolumnar Ge0.9Se0.1 Films Are Rapidly Lithiated/Delithiated. *Journal of Physical Chemistry C*, *118*, 17407–17412.

Abel, P. R., Klavetter, K. C., Jarvis, K., Heller, A., & Mullins, C. B. (2014). Sub-stoichiometric germanium sulfide thin-films as a high-rate lithium storage material. *Journal of Materials Chemistry A*, *2*, 19011–19018. doi:10.1039/c4ta04496g

Alay-e-Abbas, S. M., & Shaukat, a. (2010). FP-LAPW calculations of structural, electronic, and optical properties of alkali metal tellurides: M2Te [M: Li, Na, K and Rb]. *Journal of Materials Science*, *46*(4), 1027–1037. doi:10.1007/s10853-010-4868-7

Aravindan, V., Gnanaraj, J., Madhavi, S., & Liu, H.-K. (2011). Lithium-ion conducting electrolyte salts for lithium batteries. *Chemistry A European Journal*, *17*, 14326–14346. doi:10.1002/chem.201101486

Aurbach, D. (2000). Review of selected electrode-solution interactions which determine the performance of Li and Li ion batteries. *Journal of Power Sources*, *89*(2), 206–218. doi:10.1016/S0378-7753(00)00431-6

Aurbach, D., Levi, M. D., Levi, E., & Schechter, A. (1997). Failure and Stabilization Mechanisms of Graphite Electrodes. *The Journal of Physical Chemistry B*, *101*(12), 2195–2206. doi:10.1021/jp962815t

Aurbach, D., Markovsky, B., Levi, M. D., Levi, E., Schechter, A., Moshkovich, M., & Cohen, Y. (1999). New insights into the interactions between electrode materials and electrolyte solutions for advanced nonaqueous batteries. *Journal of Power Sources*, *81-82*, 95–111. doi:10.1016/S0378-7753(99)00187-1

Aurbach, D., Zaban, A., Gofer, Y., Ely, Y. E., Weissman, I., Chusid, O., & Abramson, O. (1995). Recent studies of the lithium-liquid electrolyte interface Electrochemical, morphological and spectral studies of a few important systems. *Journal of Power Sources*, *54*(1), 76–84. doi:10.1016/0378-7753(94)02044-4

Aurbach, D., Zinigrad, E., Cohen, Y., & Teller, H. (2002). A short review of failure mechanisms of lithium metal and lithiated graphite anodes in liquid electrolyte solutions. *Solid State Ionics*, *148*(3-4), 405–416. doi:10.1016/S0167-2738(02)00080-2

Basu, S. (1981). Rechargeable Battery. United States.

Basu, S. (1983). Ambient Temperature Rechargeable Battery. United States.

Bhatt, M. D., Cho, M., & Cho, K. (2011). Density functional theory calculations for the interaction of Li+ cations and PF6- anions with nonaqueous electrolytes. *Canadian Journal of Chemistry*, *89*(12), 1525–1532. doi:10.1139/v11-131

Bieker, G., Bieker, P. M., & Winter, M. (2015). Electrochemical *In situ* Investigations of the SEI and Dendrite Formation on the Lithium Metal Anode. *Phys. Chem. Chem. Phys.*, *17*, 8670–8679. doi:10.1039/C4CP05865H

Bruce, P. G., Scrosati, B., & Tarascon, J.-M. (2008). Nanomaterials for rechargeable lithium batteries. *Angewandte Chemie*, *47*, 2930–2946. doi:10.1002/anie.200702505

Celio, H. (2014). Interface Designed with Differential Pumping and Built-in Figure of Merit Method to Monitor Chambers where Environmentally Sensitive Samples are Prepared and Transferred for Analysis. US.

Chan, C. K., Ruffo, R., Hong, S. S., & Cui, Y. (2009). Surface chemistry and morphology of the solid electrolyte interphase on silicon nanowire lithium-ion battery anodes. *Journal of Power Sources*, *189*(2), 1132–1140. doi:10.1016/j.jpowsour.2009.01.007

Chen, Z., Cao, Y., Qian, J., Ai, X., & Yang, H. (2011). Pb-sandwiched nanoparticles as anode material for lithium-ion batteries. *Journal of Solid State Electrochemistry*, *16*(1), 291–295. doi:10.1007/s10008-011-1333-8

Cho, Y. J., Im, H. S., Kim, H. S., Myung, Y., Back, S. H., Lim, Y. R., … Kang, H. S. (2013). Tetragonal phase germanium nanocrystals in lithium ion batteries. *ACS Nano*, *7*(10), 9075–84. doi:10.1021/nn403674z

Chung, J.-S., & Sohn, H.-J. (2002). Electrochemical behaviors of CuS as a cathode material for lithium secondary batteries. *Journal of Power Sources*, *108*, 226–231.

Cunningham, P., Johnson, S., & Cairns, E. (1973). Phase Equilibria in Lithium-Chalcogen Systems III. Lithium-Tellurium. *Journal of The Electrochemical Society*, *120*(3), 328–330.

Dang, H. X., Klavetter, K. C., Meyerson, M. L., Heller, A., & Mullins, C. B. (2015). Tin microparticles for a lithium ion battery anode with enhanced cycling stability and efficiency derived from Se-doping. *Journal of Materials Chemistry A*, *3*(25), 13500–13506. doi:10.1039/C5TA02131F

Ding, F., Xu, W., Chen, X., Zhang, J., Shao, Y., Engelhard, M. H., … Zhang, J. G. (2014). Effects of cesium cations in lithium deposition via self-healing electrostatic shield mechanism. *Journal of Physical Chemistry C*, *118*(8), 4043–4049. doi:10.1021/jp4127754

Ding, F., Xu, W., Graff, G. L., Zhang, J., Sushko, M. L., Chen, X., … Zhang, J. G. (2013). Dendrite-free lithium deposition via self-healing electrostatic shield mechanism. *Journal of the American Chemical Society*, *135*(11), 4450–4456. doi:10.1021/ja312241y

Ding, N., Xu, J., Yao, Y. X., Wegner, G., Fang, X., Chen, C. H., & Lieberwirth, I. (2009). Determination of the diffusion coefficient of lithium ions in nano-Si. *Solid*

State Ionics, *180*(2-3), 222–225. doi:10.1016/j.ssi.2008.12.015

Ebner, M., Marone, F., Stampanoni, M., & Wood, V. (2013). Visualization and Quantification of Electrochemical and Mechanical Degradation in Li Ion Batteries. *Science*, *342*(6159), 716–720.

Ein-Eli, Y., Markovsky, B., Aurbach, D., Carmeli, Y., Yamin, H., & Luski, S. (1994). The dependence of the performance of Li-C intercalation anodes for Li-ion secondary batteries on the electrolyte solution composition. *Electrochimica Acta*, *39*(17), 2559–2569. doi:10.1016/0013-4686(94)00221-5

Eithiraj, R. D., Jaiganesh, G., Kalpana, G., & Road, S. P. (2009). First-Principles Study of Electronic Structure and Ground-State Properties of Alkali-Metal Selenides and Tellurides (M2A) [M: Li, Na, K; A: Se, Te]. *International Journal of Modern Physics B*, *23*(25), 5027–5037.

Etacheri, V., Haik, O., Goffer, Y., Roberts, G. A., Stefan, I. C., Fasching, R., & Aurbach, D. (2012). Effect of Fluoroethylene Carbonate (FEC) on the Performance and Surface Chemistry of Si-Nanowire Li-Ion Battery Anodes. *Langmuir*, *28*(1), 965–976. doi:10.1021/la203712s

Etacheri, V., Marom, R., Elazari, R., Salitra, G., & Aurbach, D. (2011). Challenges in the development of advanced Li-ion batteries: a review. *Energy & Environmental Science*, *4*, 3243–3262. doi:10.1039/c1ee01598b

Fan, S., Lim, L. Y., Tay, Y. Y., Pramana, S. S., Rui, X., Samani, M. K., … Hng, H. H. (2013). Rapid fabrication of a novel Sn–Ge alloy: structure–property relationship and its enhanced lithium storage properties. *Journal of Materials Chemistry A*, *1*(46), 14577. doi:10.1039/c3ta13315j

Gong, L., Nguyen, M. H. T., & Oh, E.-S. (2013). High polar polyacrylonitrile as a potential binder for negative electrodes in lithium ion batteries. *Electrochemistry*

Communications, *29*, 45–47. doi:10.1016/j.elecom.2013.01.010

Gonzalez, J., Sun, K., Huang, M., Dillon, S., Chasiotis, I., & Lambros, J. (2015). X-ray microtomography characterization of Sn particle evolution during lithiation/delithiation in lithium ion batteries. *Journal of Power Sources*, *285*, 205–209. doi:10.1016/j.jpowsour.2015.03.093

Goodenough, J. B., & Kim, Y. (2010). Challenges for Rechargeable Li Batteries. *Chemistry of Materials*, *22*(3), 587–603. doi:10.1021/cm901452z

Goodenough, J. B., & Park, K.-S. (2013). The Li-Ion Rechargeable Battery: A Perspective. *Journal of the American Chemical Society*, *135*(4), 1167–1176. doi:10.1021/ja3091438

Goodman, J. K. S., & Kohl, P. A. (2014). Effect of Alkali and Alkaline Earth Metal Salts on Suppression of Lithium Dendrites. *Journal of The Electrochemical Society*, *161*(9), D418–D424. doi:10.1149/2.0301409jes

Goward, G. R., Taylor, N. J., Souza, D. C. S., & Nazar, L. F. (2001). The true crystal structure of Li17M4 (M=Ge, Sn, Pb)-revised from Li22M5. *Journal of Alloys and Compounds*, *329*(1-2), 82–91. doi:10.1016/S0925-8388(01)01567-5

Grugeon, S., Laruelle, S., Dupont, L., & Tarascon, J. M. (2003). An update on the reactivity of nanoparticles Co-based compounds towards Li. *Solid State Sciences*, *5*(6), 895–904. doi:10.1016/S1293-2558(03)00114-6

Han, F., Li, W.-C., Li, M.-R., & Lu, A.-H. (2012). Fabrication of superior-performance SnO2@C composites for lithium-ion anodes using tubular mesoporous carbon with thin carbon walls and high pore volume. *Journal of Materials Chemistry*, *22*(19), 9645–9651. doi:10.1039/c2jm31359f

Han, J., Huang, Y., & Goodenough, J. (2011). New anode framework for rechargeable lithium batteries. *Chemistry of Materials*, *23*, 2027–2029.

Han, S., Park, J., Lu, W., & Sastry, A. M. (2013). Numerical study of grain boundary effect on Li+ effective diffusivity and intercalation-induced stresses in Li-ion battery active materials. *Journal of Power Sources*, *240*, 155–167. doi:10.1016/j.jpowsour.2013.03.135

He, M., Yuan, L., Zhang, W., Hu, X., & Huang, Y. (2011). Enhanced Cyclability for Sulfur Cathode Achieved by a Water-Soluble Binder. *Journal of Physical Chemistry C*, *115*, 15703–15709.

Howlett, P. C., MacFarlane, D. R., & Hollenkamp, A. F. (2003). A sealed optical cell for the study of lithium-electrode|electrolyte interfaces. *Journal of Power Sources*, *114*, 277–284. doi:10.1016/S0378-7753(02)00603-1

Howlett, P. C., MacFarlane, D. R., & Hollenkamp, A. F. (2004). High Lithium Metal Cycling Efficiency in a Room-Temperature Ionic Liquid. *Electrochemical and Solid-State Letters*, *7*(5), A97–A101. doi:10.1149/1.1664051

Huggins, R. (1997). Alloy negative electrodes for lithium batteries formed in-situ from oxides. *Ionics*, *3*, 245–255.

Huggins, R. (1998). Lithium alloy negative electrodes formed from convertible oxides. *Solid State Ionics*, *113-115*(1-2), 57–67. doi:10.1016/S0167-2738(98)00275-6

Huggins, R. (1999). Lithium alloy negative electrodes. *Journal of Power Sources*, *81-82*, 13–19. doi:10.1016/S0378-7753(99)00124-X

IEC. (2012). *Electrical Energy Storage White Paper*. *www.iec.ch*. doi:10.1016/j.icrp.2009.12.007

Im, H. S., Cho, Y. J., Lim, Y. R., Jung, C. S., Jang, D. M., Park, J., … Kang, H. S. (2013). Phase evolution of tin nanocrystals in lithium ion batteries. *ACS Nano*, *7*(12), 11103–11. doi:10.1021/nn404837d

Jayaprakash, N., Shen, J., Moganty, S. S., Corona, a., & Archer, L. a. (2011). Porous

Hollow Carbon@Sulfur Composites for High-Power Lithium-Sulfur Batteries. *Angewandte Chemie*, *123*(26), 6026–6030. doi:10.1002/ange.201100637

Jeong, S. K., Inaba, M., Iriyama, Y., Abe, T., & Ogumi, Z. (2002). Surface film formation on a graphite negative electrode in lithium-ion batteries: AFM study on the effects of co-solvents in ethylene carbonate-based solutions. *Electrochimica Acta*, *47*(12), 1975–1982. doi:10.1016/S0013-4686(02)00099-3

Kim, D. G., Kim, H., Sohn, H. J., & Kang, T. (2002). Nanosized Sn-Cu-B alloy anode prepared by chemical reduction for secondary lithium batteries. *Journal of Power Sources*, *104*, 221–225. doi:10.1016/S0378-7753(01)00918-1

Kim, H., Ding, Y., & Kohl, P. A. (2012). LiSICON – ionic liquid electrolyte for lithium ion battery. *Journal of Power Sources*, *198*, 281–286. doi:10.1016/j.jpowsour.2011.10.005

Kim, H., Jeong, G., Kim, Y.-U., Kim, J.-H., Park, C.-M., & Sohn, H.-J. (2013). Metallic anodes for next generation secondary batteries. *Chemical Society Reviews*, *42*(23), 9011–34. doi:10.1039/c3cs60177c

Kishida, I., Koyama, Y., Kuwabara, A., Yamamoto, T., Oba, F., & Tanaka, I. (2006). First-principles calculations of migration energy of lithium ions in halides and chalcogenides. *The Journal of Physical Chemistry B*, *110*(16), 8258–8262. doi:10.1021/jp0559229

Klavetter, K. C., Pedro de Souza, J., Heller, A., & Mullins, C. B. (2015). High tap density microparticles of selenium-doped germanium as a high efficiency, stable cycling lithium-ion battery anode material. *Journal of Materials Chemistry A*, *3*(11), 5829–5834. doi:10.1039/C5TA00319A

Klavetter, K. C., Wood, S. M., Lin, Y.-M., Snider, J. L., Davy, N. C., Chockla, A. M., … Mullins, C. B. (2013). A high-rate germanium-particle slurry cast Li-ion anode with

high Coulombic efficiency and long cycle life. *Journal of Power Sources*, *238*, 123–136. doi:10.1016/j.jpowsour.2013.02.091

Konstantinov, K., Ng, S. H., Wang, J. Z., Wang, G. X., Wexler, D., & Liu, H. K. (2006). Nanostructured PbO materials obtained *in situ* by spray solution technique for Li-ion batteries. *Journal of Power Sources*, *159*(1), 241–244. doi:10.1016/j.jpowsour.2006.04.029

Laruelle, S., Grugeon, S., Poizot, P., Dollé, M., Dupont, L., & Tarascon, J.-M. (2002). On the Origin of the Extra Electrochemical Capacity Displayed by MO/Li Cells at Low Potential. *Journal of The Electrochemical Society*, *149*(5), A627–A634. doi:10.1149/1.1467947

Lavela, P., Morales, J., Sánchez, L., & Tirado, J. L. (1997). Novel layered chalcogenides as electrode materials for lithium-ion batteries. *Journal of Power Sources*, *68*(2), 704–707. doi:10.1016/S0378-7753(96)02577-3

Lee, H., Yanilmaz, M., Toprakci, O., Fu, K., & Zhang, X. (2014). A review of recent developments in membrane separators for rechargeable lithium-ion batteries. *Energy & Environmental Science*, *7*(12), 3857–3886. doi:10.1039/C4EE01432D

Leroy, S., Blanchard, F., Dedryvère, R., Martinez, H., Carré, B., Lemordant, D., & Gonbeau, D. (2005). Surface film formation on a graphite electrode in Li-ion batteries: AFM and XPS study. *Surface and Interface Analysis*, *37*(10), 773–781. doi:10.1002/sia.2072

Li, C.-H., Sengodu, P., Wang, D.-Y., Kuo, T.-R., & Chen, C.-C. (2015). Highly stable cycling of a lead oxide/copper nanocomposite as an anode material in lithium ion batteries. *RSC Advances*, *5*(62), 50245–50252. doi:10.1039/C5RA07948A

Li, P., Lin, X., Shao, L., Shui, M., Wang, D., Long, N., & Shu, J. (2015). PbSbO2Cl@C nanocomposite as lithium storage material for secondary lithium-ion batteries.

Journal of Electroanalytical Chemistry, *747*, 39–44. doi:10.1016/j.jelechem.2015.04.001

Li, P., Shu, J., Shao, L., Lin, X., Wu, K., Shui, M., … Ren, Y. (2014). Comparison of morphology and electrochemical behavior between PbSbO2Cl and PbCl2/Sb4O5Cl2. *Journal of Electroanalytical Chemistry*, *731*(3), 128–132. doi:10.1016/j.jelechem.2014.08.027

Li, X., Qiao, L., Li, D., Wang, X., Xie, W., & He, D. (2013). Three-dimensional network structured α-Fe2O3 made from a stainless steel plate as a high-performance electrode for lithium ion batteries. *Journal of Materials Chemistry A*, *1*(21), 6400–6406. doi:10.1039/c3ta10821j

Li, X., Shang, X., Li, D., Yue, H., Wang, S., Qiao, L., & He, D. (2014). Facile synthesis of porous MnO microspheres for high-performance lithium-ion batteries. *Particle and Particle Systems Characterization*, *31*(9), 1001–1007. doi:10.1002/ppsc.201400010

Li, Y., Tu, J. P., Wu, H. M., Yuan, Y. F., & Shi, D. Q. (2006). Mechanochemical synthesis and electrochemical properties of nanosized SnS as an anode material for lithium ion batteries. *Materials Science and Engineering: B*, *128*(1-3), 75–79. doi:10.1016/j.mseb.2005.11.017

Li, Z., Huang, J., Yann Liaw, B., Metzler, V., & Zhang, J. (2014). A review of lithium deposition in lithium-ion and lithium metal secondary batteries. *Journal of Power Sources*, *254*, 168–182. doi:10.1016/j.jpowsour.2013.12.099

Liang, Z., Lin, D., Zhao, J., Lu, Z., Liu, Y., Liu, C., … Cui, Y. (2016). Composite lithium metal anode by melt infusion of lithium into a 3D conducting scaffold with lithiophilic coating. *Proceedings of the National Academy of Sciences*, *113*(11), 2862–2867. doi:10.1073/pnas.1518188113

Lin, Y.-M., Klavetter, K. C., Abel, P. R., Davy, N. C., Snider, J. L., Heller, A., & Mullins, C. B. (2012). High performance silicon nanoparticle anode in fluoroethylene carbonate-based electrolyte for Li-ion batteries. *Chemical Communications*, *48*(58), 7268–7270. doi:10.1039/c2cc31712e

Liu, Z., & Yang, J. (2001). Electrochemical performance of Pb3(PO4)2 anodes in rechargeable lithium batteries. *Journal of Power Sources*, *97-98*, 247–250.

Lu, J., Nan, C., Li, L., Peng, Q., & Li, Y. (2012). Flexible SnS nanobelts: Facile synthesis, formation mechanism and application in Li-ion batteries. *Nano Research*, *6*(1), 55–64. doi:10.1007/s12274-012-0281-7

Lu, Y., Tu, Z., & Archer, L. A. (2014). Stable lithium electrodeposition in liquid and nanoporous solid electrolytes. *Nature Materials*, *13*(October), 961–969. doi:10.1038/nmat4041

Luo, C., Xu, Y., Zhu, Y., Liu, Y., Zheng, S., Liu, Y., … Wang, C. (2013). Selenium@Mesoporous Carbon Composite with Superior Lithium and Sodium Storage Capacity. *ACS Nano*, *7*(9), 8003–8010.

Madelung, O., Rössler, U., & Schulz, M. (1998). Lead selenide (PbSe) crystal structure, lattice parameters, thermal expansion. In *Non-Tetrahedrally Bonded Elements and Binary Compounds I* (pp. 1–4). doi:10.1007/10681727_903

Martos, M., Morales, J., & Sanchez, L. (2003). Lead-based systems as suitable anode materials for Li-ion batteries. *Electrochimica Acta*, *48*, 615–621.

Martos, M., Morales, J., Sanchez, L., & Ayouchi, R. (2001). Electrochemical properties of lead oxide films obtained by spray pyrolysis as negative electrodes for lithium secondary batteries. *Electrochimica Acta*, *46*, 2939–2948.

Matsuda, Y., Fukushima, T., Hashimoto, H., & Arakawa, R. (2002). Solvation of Lithium Ions in Mixed Organic Electrolyte Solutions by Electrospray Ionization Mass

Spectroscopy. *Journal of The Electrochemical Society*, *149*(8), A1045–A1048. doi:10.1149/1.1489687

Mayers, M. Z., Kaminski, J. W., & Miller, T. F. (2012). Suppression of dendrite formation via pulse charging in rechargeable lithium metal batteries. *Journal of Physical Chemistry C*, *116*(50), 26214–26221. doi:10.1021/jp309321w

McDowell, M. T., Lee, S. W., Nix, W. D., & Cui, Y. (2013). 25th anniversary article: Understanding the lithiation of silicon and other alloying anodes for lithium-ion batteries. *Advanced Materials*, *25*(36), 4966–4985. doi:10.1002/adma.201301795

Morachevskii, A. (2001). Thermodynamic Analysis of Alloying in the System Lithium-Tellurium. *Russian Journal of Applied Chemistry*, *74*(4), 564–568.

Nadimpalli, S. P. V, Sethuraman, V. a., Dalavi, S., Lucht, B., Chon, M. J., Shenoy, V. B., & Guduru, P. R. (2012). Quantifying capacity loss due to solid-electrolyte-interphase layer formation on silicon negative electrodes in lithium-ion batteries. *Journal of Power Sources*, *215*, 145–151. doi:10.1016/j.jpowsour.2012.05.004

Naji, A., Ghanbaja, J., Humbert, B., Willmann, P., & Billaud, D. (1996). Electroreduction of graphite in LiClO4-ethylene carbonate electrolyte. Characterization of the passivating layer by transmission electron microscopy and Fourier-transform infrared spectroscopy. *Journal of Power Sources*, *63*, 33–39. doi:10.1016/S0378-7753(96)02439-1

Naji, A., Ghanbaja, J., Willmann, P., Humbert, B., & Billaud, D. (1996). First characterization of the surface compounds formed during the reduction of a carbonaceous electrode in LiClO4-ethylene carbonate electrolyte. *Journal of Power Sources*, *62*, 141–143. doi:10.1016/S0378-7753(96)02401-9

Ng, S. H., Wang, J., Konstantinov, K., Wexler, D., Chen, J., & Liu, H. K. (2006). Spray Pyrolyzed PbO-Carbon Nanocomposites as Anode for Lithium-Ion Batteries.

Journal of The Electrochemical Society, *153*(4), A787–A793. doi:10.1149/1.2172570

Nie, M., Abraham, D. P., Chen, Y., Bose, A., & Lucht, B. L. (2013). Silicon solid electrolyte interphase (SEI) of lithium ion battery characterized by microscopy and spectroscopy. *Journal of Physical Chemistry C*, *117*(26), 13403–13412. doi:10.1021/jp404155y

Obrovac, M. N., & Christensen, L. (2004). Structural Changes in Silicon Anodes during Lithium Insertion/Extraction. *Electrochemical and Solid-State Letters*, *7*(5), A93–A96. doi:10.1149/1.1652421

Pan, Q., Wang, Z., Liu, J., Yin, G., & Gu, M. (2009). PbO@C core–shell nanocomposites as an anode material of lithium-ion batteries. *Electrochemistry Communications*, *11*(4), 917–920. doi:10.1016/j.elecom.2009.02.028

Perry, D. L., & Wilkinson, T. J. (2007). Synthesis of high-purity α- and β-PbO and possible applications to synthesis and processing of other lead oxide materials. *Applied Physics A*, *89*(1), 77–80. doi:10.1007/s00339-007-4073-y

Ponrouch, A., Taberna, P. L., Simon, P., & Palacín, M. R. (2012). On the origin of the extra capacity at low potential in materials for Li batteries reacting through conversion reaction. *Electrochimica Acta*, *61*, 13–18. doi:10.1016/j.electacta.2011.11.029

Powell, E. J., Wood, S. M., Heller, A., & Mullins, C. B. (n.d.). Obviating the need for nanocrystallites in the extended lithiation/delithiation of germanium. *Journal of Materials Chemistry A*, accepted. doi:10.1039/x0xx00000x

Profatilova, I. A., Stock, C., Schmitz, A., Passerini, S., & Winter, M. (2013). Enhanced thermal stability of a lithiated nano-silicon electrode by fluoroethylene carbonate and vinylene carbonate. *Journal of Power Sources*, *222*, 140–149.

doi:10.1016/j.jpowsour.2012.08.066

Rui, K., Wen, Z., Huang, X., Lu, Y., Jin, J., & Shen, C. (2016). High-performance lithium storage in an ultrafine manganese fluoride nanorod anode with enhanced electrochemical activation based on conversion reaction. *Phys. Chem. Chem. Phys.*, *18*(5), 3780–3787. doi:10.1039/C5CP07361H

Sanusi, A., Yahya, M. Z. A., Navaratnam, S., Basirun, W. J., Alias, Y., Mohamed, N. S., & Arof, A. K. (2003). Sulphide based anode material for lithium rechargeable battery. *Ionics*, *9*(3-4), 253–257. doi:10.1007/BF02375976

Seng, K. H., Li, L., Chen, D. P., Chen, Z. X., Wang, X. L., Liu, H. K., & Guo, Z. P. (2013). The effects of FEC (fluoroethylene carbonate) electrolyte additive on the lithium storage properties of NiO (nickel oxide) nanocuboids. *Energy*, *58*, 707–713. doi:10.1016/j.energy.2013.06.011

Seo, D. M., Reininger, S., Kutcher, M., Redmond, K., Euler, W. B., & Lucht, B. L. (2015). Role of Mixed Solvation and Ion Pairing in the Solution Structure of Lithium Ion Battery Electrolytes. *The Journal of Physical Chemistry C*, *119*, 14038–14046. doi:10.1021/acs.jpcc.5b03694

Shu, J., Ma, R., Shao, L., Shui, M., Hou, L., Wu, K., … Ren, Y. (2013). Facile preparation of nano-micro structure PbSbO2Cl as a novel anode material for lithium-ion batteries. *RSC Advances*, *3*(2), 372–376. doi:10.1039/c2ra22337f

Shu, J., Ma, R., Shao, L., Shui, M., Wang, D., Wu, K., … Ren, Y. (2013). Hydrothermal fabrication of lead hydroxide chloride as a novel anode material for lithium-ion batteries. *Electrochimica Acta*, *102*, 381–387. doi:10.1016/j.electacta.2013.04.023

Skarmoutsos, I., Ponnuchamy, V., Vetere, V., & Mossa, S. (2015). Li+ solvation in pure, binary and ternary mixtures of organic carbonate electrolytes. *The Journal of Physical Chemistry C*, *119*, 4502–4515.

Song, J.-H., Yeon, J.-T., Jang, J.-Y., Han, J.-G., Lee, S.-M., & Choi, N.-S. (2013). Effect of Fluoroethylene Carbonate on Electrochemical Performances of Lithium Electrodes and Lithium-Sulfur Batteries. *Journal of the Electrochemical Society*, *160*(6), A873–A881. doi:10.1149/2.101306jes

Survey, U. S. G. (2016). *Mineral Commodity Summaries 2016: Lead*. *Mineral Commodity Summaries 2015*. doi:10.1017/CBO9781107415324.004

Tarascon, J. M., & Armand, M. (2001). Issues and challenges facing rechargeable lithium batteries. *Nature*, *414*, 359–367. doi:10.1038/35104644

Thackeray, M. M., Wolverton, C., & Isaacs, E. D. (2012). Electrical energy storage for transportation—approaching the limits of, and going beyond, lithium-ion batteries. *Energy & Environmental Science*, *5*, 7854–7863. doi:10.1039/c2ee21892e

Torabi, M. (2011). Electrochemical Evaluation of PbO Nanoparticles as Anode for Lithium Ion Batteries. *International Journal of Engineering*, *24*(4), 351–356. doi:10.5829/idosi.ije.2011.24.04b.05

Tovar, L. G., & Connor, P. (2001). Investigation of lead tin fluorides as possible negative electrodes for Li-ion batteries. *Journal of Power Sources*, *98*, 473–476.

Trifonova, A., & Momchilov, A. (2001). Electrochemical lithium intercalation in lead–tin–aluminium solder. *Solid State Ionics*, *143*, 319–328.

Tu, F., Huo, Y., Xie, J., Cao, G., Zhu, T., Zhao, X., & Zhang, S. (2013). Reduced graphene oxide induced confined growth of PbTe crystals and enhanced electrochemical Li-storage properties. *RSC Advances*, *3*(45), 23612–23619. doi:10.1039/c3ra42466a

Valentine, D. Y., Cavin, O. B., & Yakel, H. L. (1977). On the crystal structure of LiTe3. *Acta Crystallographica*, *B33*.

van de Krol, R., Goossens, A., & Meulenkamp, E. A. (1999). *In situ* X-Ray Diffraction of

Lithium Intercalation in Nanostructured and Thin Film Anatase TiO2. *Journal of The Electrochemical Society*, *146*(9), 3150–3154. doi:10.1149/1.1392447

Verma, P., Maire, P., & Novák, P. (2010). A review of the features and analyses of the solid electrolyte interphase in Li-ion batteries. *Electrochimica Acta*, *55*(22), 6332–6341. doi:10.1016/j.electacta.2010.05.072

Wakihara, M. (2001). Recent developments in lithium ion batteries. *Materials Science and Engineering: R: Reports*, *33*(4), 109–134.

Wang, D., Wu, K., Shao, L., Shui, M., Ma, R., Lin, X., … Shu, J. (2014). Facile fabrication of Pb(NO3)2/C as advanced anode material and its lithium storage mechanism. *Electrochimica Acta*, *120*(3), 110–121. doi:10.1016/j.electacta.2013.12.080

Wang, H., & Yoshio, M. (2010). KPF6 dissolved in propylene carbonate as an electrolyte for activated carbon/graphite capacitors. *Journal of Power Sources*, *195*(4), 1263–1265. doi:10.1016/j.jpowsour.2009.08.073

Wang, H., Yu, J., Zhao, Y., & Guo, Q. (2013). A facile route for PbO@C nanocomposites: An electrode candidate for lead-acid batteries with enhanced capacitance. *Journal of Power Sources*, *224*, 125–131. doi:10.1016/j.jpowsour.2012.09.051

Wang, J., Feng, C.-Q., Sun, Z.-Q., Chou, S.-L., Liu, H.-K., & Wang, J.-Z. (2014). In-situ One-step Hydrothermal Synthesis of a Lead Germanate-Graphene Composite as a Novel Anode Material for Lithium-Ion Batteries. *Scientific Reports*, *4*(7030), 1–7. doi:10.1038/srep07030

Wang, J., King, P., & Huggins, R. (1986). Investigations of binary lithium-zinc, lithium-cadmium and lithium-lead alloys as negative electrodes in organic solvent-based electrolyte. *Solid State Ionics*, *20*, 185–189.

Wang, X., Liu, B., Xiang, Q., Wang, Q., Hou, X., Chen, D., & Shen, G. (2014). Spray-painted binder-free SnSe electrodes for high-performance energy-storage devices. *ChemSusChem*, *7*(1), 308–313. doi:10.1002/cssc.201300241

Wang, Y., & Balbuena, P. B. (2005). Theoretical Studies on Cosolvation of Li Ion and Solvent Reductive Decomposition in Binary Mixtures of Aliphatic Carbonates. *International Journal of Quantum Chemistry*, *102*(5), 724–733. doi:10.1002/qua.20466

Wang, Y., Nakamura, S., Ue, M., & Balbuena, P. B. (2001). Theoretical studies to understand surface chemistry on carbon anodes for lithium-ion batteries: Reduction mechanisms of ethylene carbonate. *Journal of the American Chemical Society*, *123*(47), 11708–11718. doi:10.1021/ja0164529

Warner, J. (2014). *Lithium-Ion Batteries: Advances and Applications, Chapter 7. Lithium-Ion Battery Packs for EVs*. *Lithium-Ion Batteries: Advances and Applications* (Vol. 1). doi:10.1086/640981

Wen, J., Yu, Y., & Chen, C. (2012). A Review on Lithium-Ion Batteries Safety Issues: Existing Problems and Possible Solutions. *Materials Express*, *2*(3), 197–212. doi:10.1166/mex.2012.1075

Wertheim, G. K., Van Attekum, P. T. T. M., & Basu, S. (1980). Electronic structure of lithium graphite. *Solid State Communications*, *33*(11), 1127–1130. doi:10.1016/0038

Wood, S. M., Klavetter, K. C., Heller, A., & Mullins, C. B. (2014). Fast lithium transport in PbTe for lithium-ion battery anodes. *Journal of Materials Chemistry A*, *2*(20), 7238–7243. doi:10.1039/c4ta01167h

Wood, S. M., Pham, C. H., Heller, A., & Mullins, C. B. (2016). Stages in the Dynamic Electrochemical Lithiation of Lead. *Journal of The Electrochemical Society*, *163*(6), A1027–A1029. doi:10.1149/2.1251606jes

Wood, S. M., Powell, E. J., Heller, A., & Mullins, C. B. (2015). Lithiation and Delithiation of Lead Sulfide (PbS). *Journal of the Electrochemical Society*, *162*(7), A1182–A1185. doi:10.1149/2.0241507jes

Xiang, H., Mei, D., Yan, P., Bhattacharya, P., Burton, S. D., Cresce, A. V. W., … Xu, W. (2015). The Role of Cesium Cation in Controlling Interphasial Chemistry on Graphite Anode in Propylene Carbonate-Rich Electrolytes. *ACS Applied Materials & Interfaces*, *7*, 20687–20695. doi:10.1021/acsami.5b05552

Xie, J., Tu, F., Su, Q., Du, G., Zhang, S., Zhu, T., … Zhao, X. (2014). *In situ* TEM characterization of single PbSe/reduced-graphene-oxide nanosheet and the correlation with its electrochemical lithium storage performance. *Nano Energy*, *5*, 122–131. doi:10.1016/j.nanoen.2014.03.001

Xu, K. (2004). Nonaqueous liquid electrolytes for lithium-based rechargeable batteries. *Chemical Reviews*, *104*(10), 4303–4417.

Xu, S. D., Zhuang, Q. C., Tian, L. L., Qin, Y. P., Fang, L., & Sun, S. G. (2011). Impedance spectra of nonhomogeneous, multilayered porous composite graphite electrodes for Li-ion batteries: Experimental and theoretical studies. *Journal of Physical Chemistry C*, *115*(18), 9210–9219. doi:10.1021/jp107406s

Xu, S. D., Zhuang, Q. C., Wang, J., Xu, Y. Q., & Zhu, Y. B. (2013). New insight into vinylethylene carbonate as a film forming additive to ethylene carbonate-based electrolytes for lithium-ion batteries. *International Journal of Electrochemical Science*, *8*(6), 8058–8076.

Xu, W., Wang, J., Ding, F., Chen, X., Nasybulin, E., Zhang, Y., & Zhang, J.-G. (2014). Lithium metal anodes for rechargeable batteries. *Energy & Environmental Science*, *7*, 513. doi:10.1039/c3ee40795k

Xu, Y., Guo, J., & Wang, C. (2012). Sponge-like porous carbon/tin composite anode

materials for lithium ion batteries. *Journal of Materials Chemistry*, *22*, 9562–9567. doi:10.1039/c2jm30448a

Xu, Y., Zhu, Y., Liu, Y., & Wang, C. (2013). Electrochemical performance of porous carbon/tin composite anodes for sodium-ion and lithium-ion batteries. *Advanced Energy Materials*, *3*(1), 128–133. doi:10.1002/aenm.201200346

Yang, C. R., Wang, Y. Y., & Wan, C. C. (1998). Composition analysis of the passive film on the carbon electrode of a lithium-ion battery with an EC-based electrolyte. *Journal of Power Sources*, *72*, 66–70. doi:10.1016/S0378-7753(97)02655-4

Yang, L., Hua-Qing, X., & Jiang-Ping, T. (2009). SnS with Various Morphologies and Sizes as Anode Material for Lithium Ion Batteries. *Acta Physico-Chimica Sinica*, *25*(2), 365–370.

Yong-Fang, L., & Hao-Qing, W. (1987). Electrochemical Intercalation Reaction of Lithium into Sulfides of Nonlayer Structure. I. Lithium Intercalation in Lead Sulfide. *Acta Chimica Sinica*, *45*, 1147–1151.

Yu, D. Y. W., Hoster, H. E., & Batabyal, S. K. (2014). Bulk antimony sulfide with excellent cycle stability as next-generation anode for lithium-ion batteries. *Scientific Reports*, *4*(4562), 1–6. doi:10.1038/srep04562

Yu, D. Y. W., Prikhodchenko, P. V, Mason, C. W., Batabyal, S. K., Gun, J., Sladkevich, S., … Lev, O. (2013). High-capacity antimony sulphide nanoparticle-decorated graphene composite as anode for sodium-ion batteries. *Nature Communications*, *4*(2922), 1–7. doi:10.1038/ncomms3922

Yuan, Z., Peng, Z., Chen, Y., & Liu, H. (2010). Synthesis and electrochemical performance of nanosized tin lead composite oxides as lithium storage materials. *Materials Chemistry and Physics*, *120*(2-3), 331–335. doi:10.1016/j.matchemphys.2009.11.013

Zhang, W., Zhang, L., Cheng, Y., Hui, Z., & Zhang, X. (2000). Synthesis of nanocrystalline lead chalcogenides PbE (E = S , Se , or Te) from alkaline aqueous solutions. *Materials Research Bulletin*, *35*, 2009–2015.

Zhang, Y., Qian, J., Xu, W., Russell, S. M., Chen, X., Nasybulin, E., … Zhang, J. (2014). Dendrite-Free Lithium Deposition with Self-Aligned Nanorod Structure. *Nano Letters*, *14*, 6889–6896.

Zhao, X. B., Cao, G. S., Lv, C. P., Zhang, L. J., Hu, S. H., Zhu, T. J., & Zhou, B. C. (2001). Electrochemical properties of some Sb or Te based alloys for candidate anode materials of lithium-ion batteries. *Journal of Alloys and Compounds*, *315*(1-2), 265–269. doi:10.1016/S0925-8388(00)01311-6

Zheng, G., Yang, Y., Cha, J. J., Hong, S. S., & Cui, Y. (2011). Hollow carbon nanofiber-encapsulated sulfur cathodes for high specific capacity rechargeable lithium batteries. *Nano Letters*, *11*(10), 4462–4467. doi:10.1021/nl2027684

Zhu, T. J., Liu, Y. Q., & Zhao, X. B. (2008). Synthesis of PbTe thermoelectric materials by alkaline reducing chemical routes. *Materials Research Bulletin*, *43*(11), 2850–2854. doi:10.1016/j.materresbull.2008.01.001

Zhuang, Q. C., Li, J., & Tian, L. L. (2013). Potassium carbonate as film forming electrolyte additive for lithium-ion batteries. *Journal of Power Sources*, *222*, 177–183. doi:10.1016/jjpowsour.2012.08.050

Zu, C., Dolocan, A., Xiao, P., Stauffer, S., Henkelman, G., & Manthiram, A. (2015). Breaking Down the Crystallinity: The Path for Advanced Lithium Batteries. *Advanced Energy Materials*, *1501933*, 1–9. doi:10.1002/aenm.201501933

Vita

Sean Michael Wood was born in Alexandria, Virginia in 1988. His family moved to Charlotte, North Carolina in 1993, where he lived until enrolling at the Georgia Institute of Technology in 2006. While at Georgia Tech, he completed three summer research internships in Raleigh, North Carolina; Manhattan, Kansas; and Annandale, New Jersey. He received a B.S. in Chemical & Biomolecular Engineering from Georgia Tech in May 2011. The summer after his graduation, Sean completed an internship in Marl, Germany.

He began his graduate studies in Chemical Engineering at The University of Texas at Austin in August 2011. He was awarded an Integrative Graduate Education & Research Traineeship (IGERT) in 2011 and the Department of Defense's National Defense Science and Engineering Graduate (NDSEG) Fellowship in 2013. He earned a coursework M.S. degree in Chemical Engineering in May 2015 and is currently completing his Ph.D. under the guidance of Prof. Buddie Mullins and Prof. Adam Heller.

E-mail Address: seanmichaelwood@gmail.com

This dissertation was typed by the author.